Sensors and sensibility

Pieter van der Scheer

Sensors and sensibility

Tailoring the mechano-responsivity of macromolecules & polymer materials

Pieter van der Scheer

Propositions

1. Changes in the fragility of the colloidal glass transition arise completely artificially from their microscopic physics.
(this thesis)

2. Large polydispersities in conjugated polymer sensors lead to unacceptable loss of conformational resolution.
(this thesis)

3. The rigorous standards for data validation and control experiments in biological sciences should become common ground in chemistry.

4. Open scientific literature should be free of methods that depend on proprietary compounds.

5. The spreading of false or deliberately misleading information that undermine democratic processes should be considered an act of terrorism.

6. The relocation of unethical officials within government as punishment is akin to the transplantation of diseased organs into healthy patients.

Propositions belonging to the thesis, entitled

Sensors and sensibility: Tailoring the mechano-responsivity of macromolecules & polymer materials.

Pieter Cornelis van der Scheer

Wageningen, September 4th, 2020

Sensors and Sensibility

Tailoring the mechano-responsivity of macromolecules & polymer materials

Pieter Cornelis van der Scheer

Thesis committee

Promotor
Prof. Dr J.H.B. Sprakel
Personal Chair, Physical Chemistry and Soft Matter
Wageningen University & Research

Other members
Prof. Dr J.T. Zuilhof, Wageningen University & Research
Prof. Dr A.J.C. Kühne, Ulm University, Germany
Dr J.C. Hohlbein, Wageningen University & Research
Dr J.M. Clough, University of Fribourg, Switzerland

This research was conducted under the auspices of
the Graduate School VLAG. (Advanced studies in Food Technology,
Agrobiotechnology. Nutrition and Health Sciences).

Sensors and Sensibility

Tailoring the mechano-responsivity of macromolecules & polymer materials

Pieter Cornelis van der Scheer

Thesis
Submitted in fulfillment of the requirements for the degree of doctor
at Wageningen University
by the authority of the Rector Magnificus,
Prof. Dr A.P.J. Mol,
in the presence of the
Thesis Committee appointed by the Academic Board
to be defended in public
on Friday 4 September, 2020
at 1:30 p.m. in the Aula.

Pieter Cornelis van der Scheer
Sensors and Sensibility— Tailoring the mechano-responsivity of macromolecules & polymer materials
214 pages

PhD thesis, Wageningen University, Wageningen, The Netherlands (2020)
with references, with summary in English.

ISBN: 978-94-6395-396-2
DOI: https://doi.org/10.18174/521303

Contents

Introduction **1**

2 Main chain spiropyran mechanochromic sensors **21**

3 Rigidochromic conjugated polymers carrying main-chain molecular rotors **47**

4 Chain length-dependent luminescence in acceptor-doped conjugated polymers **71**

5 Mechanochemical deprotection of semiconducting polymers gated by chain architecture **105**

6 Fragility and Strength in Nanoparticle Glasses **131**

7 Two-dimensional crystals of star polymers: a tale of tails **155**

General Discussion **177**

Summary **199**

List of Publications **203**

Acknowledgments **205**

Introduction

"Nature uses only the longest threads to weave her patterns, so each small piece of her fabric reveals the organization of the entire tapestry."

- Richard Feynman

Complexity

During meteorological simulations Edward Lorenz discovered what later on would be referred to as the butterfly effect.[2, 3] Small rounding variations in the starting parameters of otherwise identical simulations caused meteorological simulations to diverge at a certain point in time. In his relatively simple simulation containing only 12 equations, the small difference in starting values caused the system of non-linear equation to display largely varying results after only a short time. Here the combination of complexity and a continuously dynamic system create a situation where it makes it very difficult to predict weather patterns on a long term. Variations in the results can be due to the systems non-linear response to inaccuracies in the input or due to the inaccuracies in the model. For meteorology, the time-scale on which this deviation emerges depends directly on the accuracy of the input data and the correctness of the model. In the case of meteorology, weather prediction accuracy has benefited enormously from the increase in wide-spread technologies collecting live data such as satellites. However, this example illustrates a more fundamental challenge of disentangling the effects of complexity from the underlying physics of a complex system. It is thus not surprising that this field of study is often referred to as ’chaos theory’.

Although not always visibly apparent, complexity (or chaos) is generic and can be found throughout nature and the living world. A graphic example is found in the intricate structures found in spider-webs, of which no two are the same. Although a spider-web can be thought of as a static structure its response to mechanic stimuli depends on the complex connections within the web.[4, 5, 6] Although a million randomly generated spider-webs might have similar properties overall, this strength is a sum of all the complex mechanical interactions within the web. If stress is applied to a web and a single strand breaks this influences the distribution of stresses across the remaining strands. This very non-linear feedback can result in critical failure of the whole structure as a result of the failure of one of its components. Although of no consequence to the survival of spiders, the identification of such a fatal cascade could lead to prevention in the design of a new web.

Another example of complexity can be found in the swarming of animals.[7, 8, 9] There are numerous reasons for lifeforms to swarm, some are generic such as the increased perceptive capabilities of a group in detecting and deterring predators and others are unique to a class of animals such as the reduced hydrodynamic drag of a school of fish.[10] Swarming is behavior that emerges from the interactions between many individuals in the absence of a central coordination and guided by few simple rules. Few simple rules, obeyed by many individuals in a group, can lead to the emergence of dynamical patterns that are vastly diverse and complex.

A more conceptual example of complexity and emergence are cellular automata. [11] These models which attempt to create self-replicating systems from fixed rules also display large variation in structure and dynamics and are very sensitive to the initial conditions. The human herd being no exception to this behaviour, these types of models are being actively used to improve the flow of people in train-stations and could be used to prevent people from trampling each-other in case of an emergency when large congregations flock together.[12, 13] Although a human might instinctively seem more complex than the blowing of the wind, the variation in both is boundless.

Finally, a more modern example of actively dynamic complexity are so called twitterstorms. Although mostly void of content the mechanism of tweeting and re-tweeting show complex dynamics. A single well-placed tweet can be picked up by several followed by a cascade of responses reaching millions of users where others just linger in obscurity. Something which is especially of interest to publicity agencies and politicians and has real world consequences. There are companies such as tweetmap dedicated to analyzing twitter responses and advise how to reach the largest amount of people with your future tweets. In the past years it has become clear that controlling the emergence of these patterns can have serious implications for politics. Understanding complexity and finding handles to control it are thus of relevance in a wide variety of scenarios.

Complex fluids

The wide variety of real-world examples given above seem to have little more in common than complexity in itself. However, there are worlds hidden beyond the scope of the human eye which we have not mentioned. Other worlds whose threads indeed seem to be organized similarly. At these much smaller length-scales, where we find the molecular world, complexity is also present. Before Pierre-Gilles de Gennes introduced the term Soft Matter in his 1991 Nobel laureate speech, the study of complexity in the molecular world was often referred to as the study of complex fluids.[14] Covering subjects such as colloids, gels, foams, polymers and biological systems this field focuses on systems which are neither liquid nor solid. In these semi-solid, semi-liquid materials all pre-requirements to find complexity are met: i) many identical molecules interact in many unpredictable ways and ii) thermal motion creates continuous agitation to randomize these interactions.

Despite being seemingly unalike, these soft materials share similarities with animal swarms (or any of the other examples given above): their structures are often self-organized and their properties emerge from the many interactions between many individuals. Although the emergent behaviour of complex fluids is easily accessible as it manifests at the macroscopic scale, understanding where this originates is challenging as it occurs on length scales not accessible by the human eye. Although the threads woven by birds are easily accessible, those on nanometer length-scales can seemingly hide their patterns because we literally cannot see them.

Just as complexity can be of consequence to an outcome when values are not known exactly it can hide physical relations like a proverbial needle in a haystack. While the study of swarms of animals can be challenging and requiring several measurements to obtain adequate statistics there is direct visual access to the length-scale of a bird. Whereas the individual components of a complex fluid can be on the nanometer scale, meaning it can be easy to capture many different interactions but the resolution to differentiate between the individual components can be challenging. This could be compared to the study of swarms of animals through a telescope from the moon. And even then it is clear, a flock of albatrosses would be much easier to analyze than a swarm of hummingbirds. Although scientists at this molecular scale often succeed in isolating and studying what is equivalent to a single ’frozen hummingbird’ and study it in high detail this does not necessarily reveal anything about the interactions between many individuals and how this leads to emergence.

A central challenge in the field of soft materials is to bridge the length scales; How does the complex behavior we can observe macroscopically

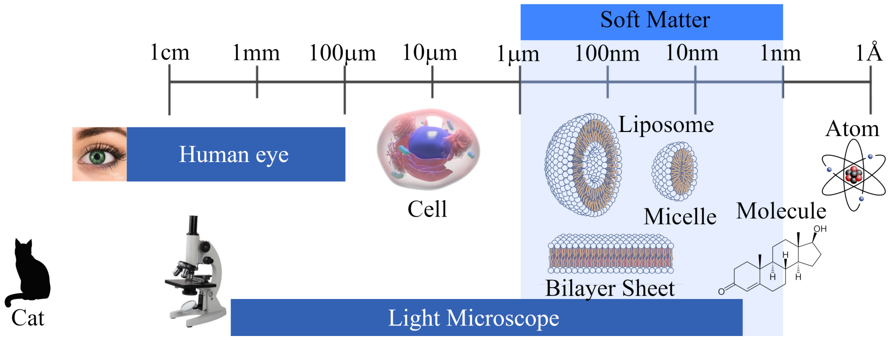

Figure 1.1: Schematic overview of the different length-scales directly and indirectly accessible within soft matter and examples covering this range.

originate from complexity at a scale many orders-of-magnitude smaller? The smallest length-scales of soft-matter systems can range from the molecular scale (several nanometers), e.g. when dealing with lipid bilayers or complex coacervates, to several micrometers, when studying tissues made of cells or in the pursuit of colloidal suspensions, to much larger in the field of granular materials. In Figure1.1 an overview of these different length-scales are shown ranging from singular atoms to individual cats and giving an idea of experimental techniques that can access these scales.

Of particular interest are methods that can reveal the interactions and behavior between individual molecules in large groups. Strong advances have been made in the past decades. However, much remains to be desired nonetheless. Some methods, e.g. scattering, can access even the smallest scales, but often yield only information about averages, and thus leave the role of the individual more elusive. Other methods, e.g. those that probe single molecules, either optically or mechanically, e.g. using Atomic Force Microscopy or Optical Tweezers, perform best when removing the individual from their natural habitat and probe its behavior in isolation. While both approaches have resulted in substantial advances in the field, it remains a major challenge how to probe the behavior of individual mo-

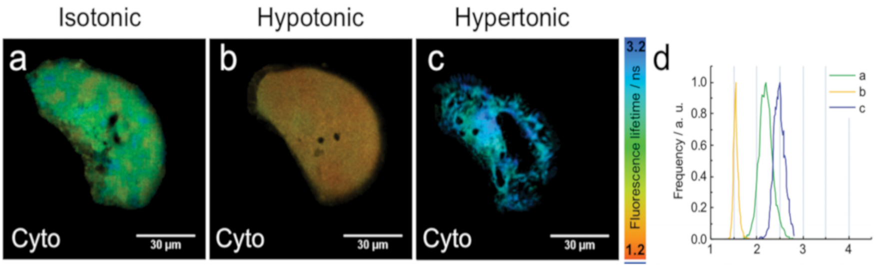

Figure 1.2: Images of BODIPY-HaloTag in COS7 cells expressing HaloTag in (a-c) the cytosol in different conditions with their corresponding fluorescence lifetime distribution histograms representing a heterogeneous viscosity distribution.Adapted from [15], copyright 2018, with permission from Elsevier.

lecules within their natural group-habitat.

Molecular sensors, molecules that report on their behavior or surroundings from within, often by sending out an optical signal, can offer a solution to this knowledge gap. The majority of this thesis has been geared to the design and study of molecular sensors to understand complex mechanics in soft materials. The central challenge here is to illuminate the stresses- and strains experienced by individual molecules, and to illuminate their spatial distribution, in order to understand how and why soft materials at the macroscopic scale respond to mechanical stress in the way they do.

Small-molecule mechanosensors

In recent years, large advances have been made in the development of small molecule mechanosensors, molecules which couple the change in their optical properties in response to a mechanical signal. This has now become a central effort in the field of mechanochemistry. A wide variety of operational mechanisms exist to create a mechano-optical coupling in small molecules, some of which we will briefly introduce here.

One versatile approach to elicit a change in optical signal induced by mechanical phenomena at the molecular scale is the use of intramolecular charge transfer induced by the creation of a twisted molecular geometry. Molecules that utilize this effect are often referred to as molecular rotors. Molecular rotors are molecules which feature a donor and acceptor moiety within the same molecule. The transfer of excited state energy from donor to acceptor relies on molecule undergoing an intramolecular rotation to a twisted state. If the molecule is mechanically-hindered to undergo this rotation, the donor will emit. If the molecule is free to rotate, and thus not mechanically hindered, charge transfer can occur, often resulting in a 'dark' state which does not emit but decays its excited state non-radiatively. This results in molecules whose emission brightness, and fluorescence lifetime, depends on the mechanical properties of their surroundings. Molecular rotors have been shown capable of measuring viscosity, free volume and even temperature, at the molecular scale.[16, 17, 18, 19] In figure1.2, an example is given of a bodipy molecular rotor introduced in cells to function as a local probe of viscosity. The probes reveal spatial inhomogeneities in the local mechanics that could not be easily revealed by other means.

A second class of small-molecule mechanosensors are so-called mechanophores. These are molecules in which mechanical stress leads to the rupture of a weak scissile bond that changes the chemistry of the molecule, and often leads to a change in optical properties for detection purposes. A widely used example of this is spiropyran, this heterocyclic molecule contains a central spiro bond, that is mechanically weak. The application of mechanical stress to this bond, leads to its rupture and induces an isomerisation into merocyanine, as shown in figure1.3a. This results not only in a structural rearrangement from a torqued to a planar conformation but this is accompanied by a change in its conjugation. In the spiropyran form, conjugation between the rings is blocked. Breaking of the C-O spiro bond upon mechanical stimulation creates and extended π-conjugation that spans the entire molecule. This conjugation switching leads to both

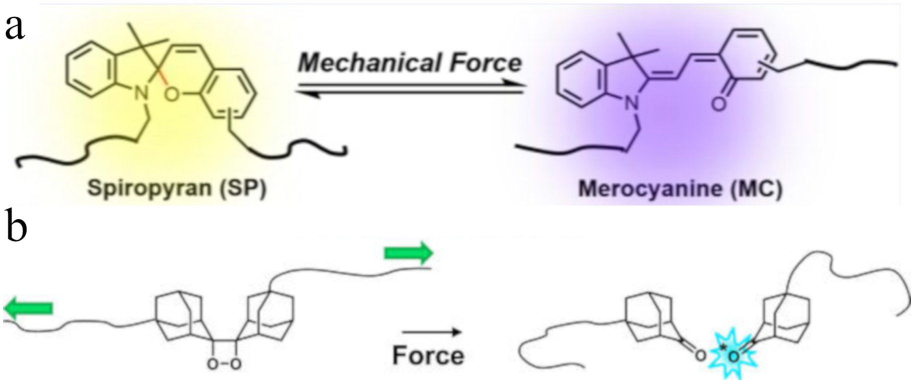

Figure 1.3: Schematic representation of the mechanical activation of a) spiropyran, adapted with permission from [20], copyright 2017, American Chemical Society. b) dioxetane, adapted with permission from [21], copyright 2017, American Chemical Society.

spectral and intensity shifts in the absorption and emission spectra of the probe. This mechano-optical coupling has been exploited in the force-induced activation of spiropyran by both stretching and compression of a bulk polymer material. [22, 23, 20, 24] Other well studied mechanophores are dioxetanes, which utilize the rupture of a non-reversible central bond of the dioxetane ring into an excited ketone group. This mechanically-generated excited state relaxes by emission of a single photon. Contrary to spiropyran, which allows for continuous absorption and emission in both states, the activation process in a dioxetane only produces photons at the moment of bond rupture. Additionally, the light which is emitted is in the UV-range which makes detection difficult and often requires presence of additional chromophores which absorb this light en re-emit in a more favorable spectral range. This makes it very versatile but also introduces issues with additional loss of light due to quantum yield limitations and other losses in the energy transfer to the acceptor. Nevertheless, it has successfully been shown that dioxetane carrying polymers in materials can be activated by bulk deformation to identify the loci of molecular damage. [25, 26, 27]

A third example borrows aspects from both of the previous mechanosensors. The Diels-Alder adduct between a conjugated diene and a substituted alkene leads to an overall reduction in conjugation. For example, the reaction of anthracene and malemide leads to a Diels-Alder adduct wherein the conjugation of the central benzene-ring in the anthracene is broken, which results in changes in its spectral properties and a loss of fluorescence. Upon mechanical stimulation the Diels-Alder bond can be broken leading to restoration of the conjugated structure of the anthracene. Similar to the spiropyran this can be continuously monitored via absorption and fluorescence emission, the scission however is irreversible. This has been used successfully to show local mechanical stresses in materials. [28]

A last main class of mechanosensors that uses small molecules to realize a mechano-optical coupling makes use of the interactions between a fluorescent donor and acceptor pair. Upon optical excitation of a donor, bringing it to an excited state, it can, depending on its spatial separation with the acceptor, transfer its excited state energy which leads to an increase of acceptor fluorescence emission that can be optically detected, e.g. through the Forster mechanism. This enables the measurement of distances in the molecular realm. Such donor-acceptor-based molecular sensors are common-ground in biophysics, and to a lesser degree in material science, and have been used to study a wide variety of molecular phenomena. An example of how this can be used in mechanosensing is found in DNA nanotechnology. A DNA hairpin, depending on its base pair design, features a unique critical force at which the hairpin unfolds and extends. By placing a donor-acceptor pair at each end of the hairpin, the energy transfer efficiency shows a binary jump from high (hairpin intact) to low (hairpin unfolded) once a critical force on the molecule is exceeded. This approach forms the basis of DNA-based FRET tension probe, which are used in a variety of mechanical problems in biology.[29, 30]

The use of small-molecule mechanosensors offers a wide array of opportunities for probing mechanics in soft and complex materials at the smallest scales. But their use comes with several disadvantages. In most cases, the mechano-optical response of these small molecules is binary, responding in a on/off fashion upon exceeding a critical force at the molecular scale. This makes their use in quantitative mapping of mechanical stresses limited. Moreover, the force range at which they function is often, with the exception of the DNA tension probe system, encoded by the stability of the chemical bonds in their design, and not tunable over a wide range of forces. Those mechanoprobes that function on the basis of the rupture of a scissile bond, such as dioxetanes or diels-alder adducts of anthracene [25, 26, 28], are irreversible and can thus not be used to probe how forces relax over time. Finally, these small molecules are often prone to photo-oxidation, which makes performing prolonged experiments challenging.

Macromolecular sensors

More recently, macromolecular mechanosensors that counter the disadvantages of the small-molecule mechanophores described above, have become a topic of study. One promising approach to measure forces at the molecular scale uses energy transfer between donor(s) and acceptor(s) embedded within a single polymer chain. For example to study the folding of labelled proteins or to look at polymer conformations.[31, 32, 33] Although here the chromophores are being used to study macro-molecules internally, their functionalities can also be combined. For example by using a donor and acceptor connected by a peptide linker which requires force to extend. By measuring the energy transfer as a function of the extension using an AFM setup, a force response calibration can be created for the energy tranfer. [29] This enables the user to not only probe distance but to translate it to a force, which in turn can be used to measure forces in a specific environment by introducing the macro-molecule.

A macro-molecular sensor can be comprised of an existing macromolecule modified to carry small molecular dyes, but can also be designed de-novo from conjugated polymers where the entire macromolecule is an optically-active mechanosensor. A conjugated polymer, in contrast to for example polystyrene, does not only contain conjugated groups but the conjugation is connected throughout the backbone of its chain. The mechano-sensitivity of the optical features of these polymers derives from the fact that their absorption and emission depends strongly on the spatial conformation of the semiconducting chain. For sufficiently flexible chains, the chain acts as an entropic spring, which features a distinct coupling between applied mechanical stress and spatial conformation. This results in a mechano-optical coupling that can be exploited for grey-scale stress sensing.

For example, the semiconducting homopolymer polyfluorene features a vibronic fine-structure in its fluorescence emission. The ratios of these vibronic peaks is known to be sensitive to the conformation of the polymer, and hence to mechanical stress. This has e.g. been used to detect the stretching forces involved in the encapsulation of such a polymer chain in a protein capsid, as illustrated in Figure 1.4. In this experiment[34], a watersoluble carboxylated polyfluorene functions as a template for the assembly of a the recombinant protein that forms a virus-mimicking capsid. The proteins complex to the semiconducting polymer, and create a crowded corona that forces the semiconducting polymer into a stretched conformation, which features a distinct spectral fingerprint. This enabled Cingil et al. to monitor the complexation process in real-time with a high resolution. The opto-mechanical coupling in these macromolecules thus enabled to study of a mechanical process at the molecular scale.

The mechano-optical coupling exploited above in homopolymers can be tailored and amplified by the introduction of acceptor-monomers in

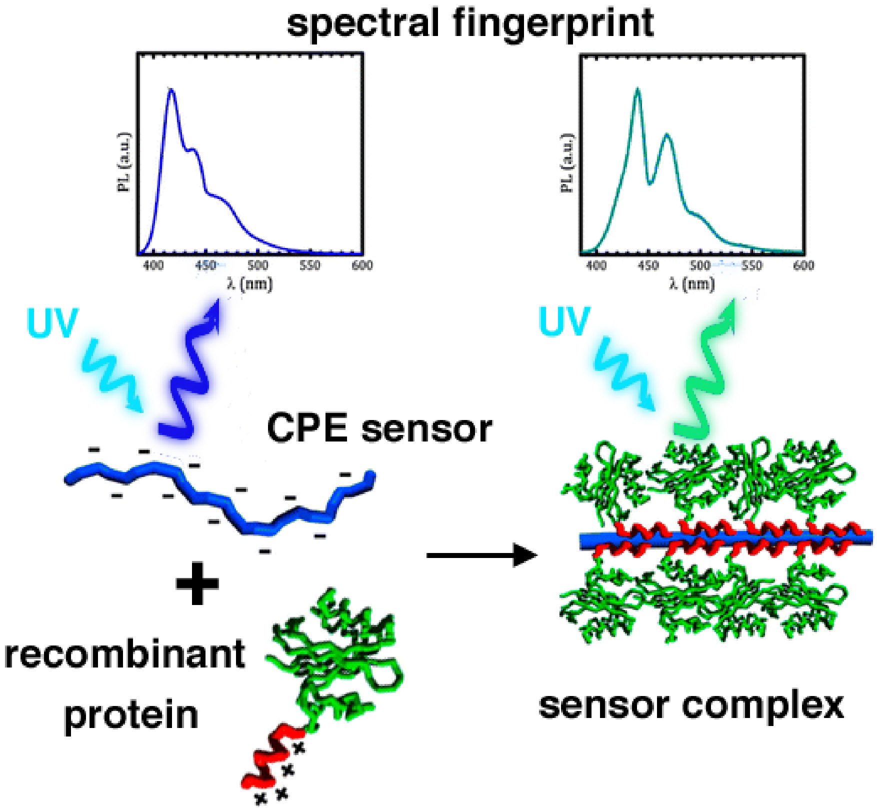

Figure 1.4: Schematic showing the conformational dependent fluorescence properties of polyfluorene used to monitor protein capsid assembly dynamics. Reprinted with permission from [34], copyright 2015, American Chemical Society.

the main chain of these semicoducting chains. Conjugated polymers such as polyfluorene are able to maintain Forster resonance energy transfer (FRET) [35, 36] between donor and acceptor chromophores which are part of the same π-extended system in a single chain, in addition to the possibility of excitonic transfer along the conjugated backbone. This results in a conformation-dependent optical response that is amplified with respect to the vibronic-based sensorics described above.

This approach has been successfully exploited to study electrostatic co-assembly between an acceptor doped conjugated polymer sensor with diblock copolymer[37]. Additionally these types of molecules have been shown to be able to probe sub-picoNewton forces with high resolution. [38] These examples show that conjugated polymers do not just have applications in solar-panels but are a relevant and useful tool in probing small length-scale mechanics. Additionally because they are sensitive to conformational changes of the polymer the force range and length-scale they probe can be directly tuned by the physical properties of the backbone and their chemical nature. For example, the spring constant of an entropic spring, setting the force range at which conformational changes, and the associated optical response, occur is dependent on the length of the chains, which can be in part controlled during their preparation. Moreover, because chain conformations change continuously upon application of increasing forces these sensors exhibit a gray-scale response that is fully reversible. By contrast to many of their small-molecule counterparts, these macromolecular sensors thus enable not only the detection of a stress, but the quantification of the stress and its dynamical nature.

Also these macromolecular sensors exhibit several drawbacks in their use. Their polymeric nature amplifies chemical incompatibility with their intended host matrix, often leading to problems of aggregation or chain collapse which reduces their functionality. Moreover, due to the preparation route followed, they are often polydisperse which reduces the fidelity with which forces can be made quantitative.

This thesis

It is clear that the two main classes of molecular mechanosensors, those based on small molecules and those that rely on the entropic conformations of macromolecules, both have their advantages and disadvantages, as summarized in Figure1.5. To date, these two approaches have remained isolated fields of study. In this thesis, we investigate the opportunities that

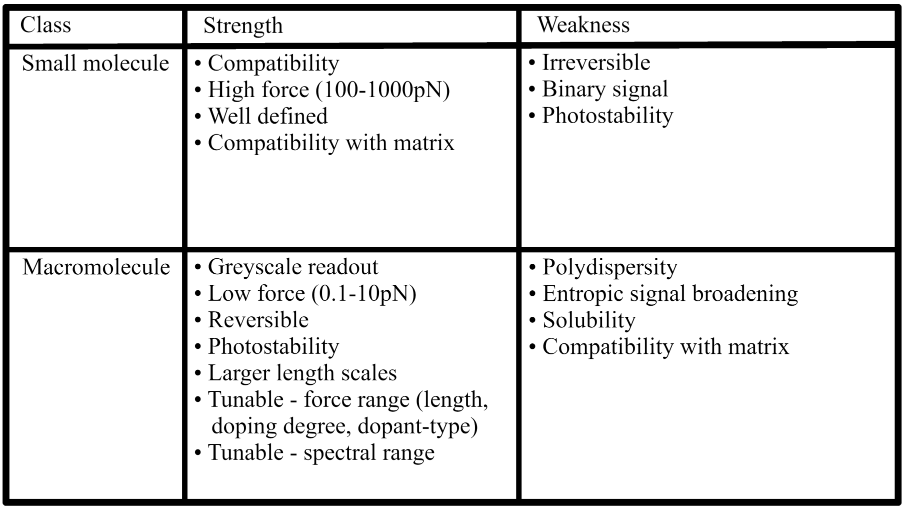

Class	Strength	Weakness
Small molecule	• Compatibility • High force (100-1000pN) • Well defined • Compatibility with matrix	• Irreversible • Binary signal • Photostability
Macromolecule	• Greyscale readout • Low force (0.1-10pN) • Reversible • Photostability • Larger length scales • Tunable - force range (length, doping degree, dopant-type) • Tunable - spectral range	• Polydispersity • Entropic signal broadening • Solubility • Compatibility with matrix

Figure 1.5: Strengths and weaknesses of small molecule and macromolecular sensors.

emerges when combining aspects of both worlds into a single molecular sensor. We explore how the combinations of optically-responsive macromolecules, with mechano-active small molecules as main-chain dopants, can lead to new and/or improved mechanosensory capabilities, with the ultimate aim to use these to shed light on the emergence of complex mechanics in soft materials.

In this thesis we aim to develop new tools to probe local mechanics & confinement effects at the nanoscale to explore mechanical emergence in soft materials.

Although each experimental situation asks for different qualities in a sensor this table provides some insight into possible advantages of combining these two classes of sensors. The ability to sense complementary force-ranges and different length-scales in parallel while combining grayscale and binary response would be a substantial improvement to current sensing capabilities. By incorporating the conjugated structure of the small molecule into the backbone of the conjugated polymer the relative photo-stability of the former would improve. However not all weaknesses are negated by the combination of the two. Especially the weaknesses of conjugated polymers need to be addressed since their polymeric nature magnifies properties, such as solubility and compatibility with their intended host matrix, to a degree where small molecules have little effect.

This presents us with several very specific challenges to overcome. Because solubility and compatibility with a matrix are very case-specific we put special emphasis on polydispersity and entropic signal broadening. Although some polymerisation reactions for conjugated polymers such as Kumada[39, 40] and Yamamoto[41, 42] have excellent polydispersity, their chemistry limits the versatility and compatibility with small molecules. In this thesis we mostly use Suzuki-Miyaura poly-condensation to allow for easy adaptation and to maximize versatility and choose to solve the polydispersity issue non-chemically.

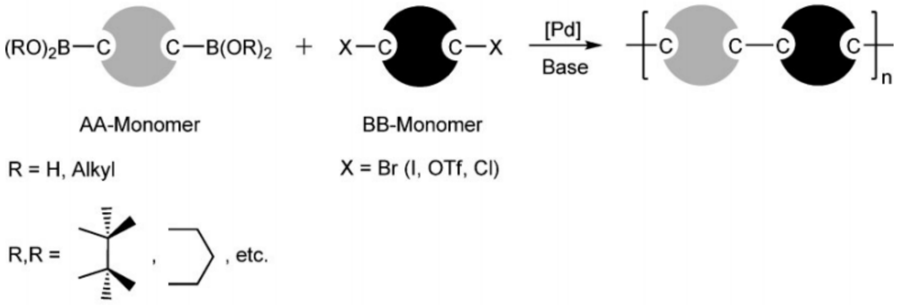

Figure 1.6: A schematic representation of the Suzuki-Miyaura polycondensation illustrating the generic nature of the reaction. Adapted from [43] copyright 2009, with permission from John Wiley & Sons Inc.

The mild conditions of Suzuki-Miyaura polycondensation make it compatible with many different monomers. Additionally because it uses a two phase reaction this increases the solubility of monomers in either solvent increasing homogeneous incorporation of dopants which is critical to avoid bias in chain architecture due to different availabilities and subsequent reactivities. The general mechanism of this reaction, shown in figure1.6[43] requires an aromatic halide and an aromatic boronic-group which are coupled using a palladium catalyst in the presence of a base and absence of oxygen and result in a conjugated carbon-carbon coupling. The interchangeable nature of the monomers gives its user great freedom in the polymer architecture allowing for facile incorporation of different functionalities or end-capping of the polymers. For example we can exploit the aromatic nature of small molecule sensors due to their high-susceptibility to bromination allowing their use in Suzuki-Miyuara polymerisation. Although this strategy is not new and creates its own challenges in monomer synthesis it remains highly effective.

Although each chapter presents independent manuscripts which are published or in preparation we present a short summarized outline. In chapters 2-5 we explore our main aim by synthesizing new macromolecular sensors which incoorporate different small mechano-active molecules into the backbone of a conjugated polymer. Subsequently, in chapter 4 we explore a generic method to improve polydispersity of conjugated polymer sensors in general and exploit this to investigate chain length-dependent properties of acceptor-doped conjugated polymers. Both of which are challenges which are encountered when doping conjugated polymers with small molecules. In chapters 6 and 7, describe the results of a side project, which although not inherently related to our main research question, are in our opinion valuable contributions to understanding complexity in soft materials. Finally, in the General Discussion we place the results of this research in a broader context and describe avenues for future exploration.

References

[1] Gleick, J. *Chaos: Making a new science* (Open Road Media, 2011).

[2] Motter, A. E. & Campbell, D. K. Chaos at fifty. Tech. Rep. (2013).

[3] Lorenz, E. The butterfly effect. *World Scientific Series on Nonlinear Science Series A* **39**, 91–94 (2000).

[4] Su, I. *et al.* Imaging and analysis of a three-dimensional spider web architecture. *Journal of The Royal Society Interface* **15**, 20180193 (2018).

[5] Benjamin, S. P. & Zschokke, S. Webs of theridiid spiders: construction, structure and evolution. *Biological Journal of the Linnean Society* **78**, 293–305 (2003).

[6] Benjamin, S. P. & Zschokke, S. Untangling the tangle-web: web construction behavior of the comb-footed spider steatoda triangulosa and comments on phylogenetic implications (araneae: Theridiidae). *Journal of Insect Behavior* **15**, 791–809 (2002).

[7] Grossman, D., Aranson, I. & Jacob, E. B. Emergence of agent swarm migration and vortex formation through inelastic collisions. *New Journal of Physics* **10**, 023036 (2008).

[8] Kok, V. J., Lim, M. K. & Chan, C. S. Crowd behavior analysis: A review where physics meets biology. *Neurocomputing* **177**, 342–362 (2016).

[9] Kelley, D. H. & Ouellette, N. T. Emergent dynamics of laboratory insect swarms. *Scientific reports* **3**, 1073 (2013).

[10] Calovi, D. S. *et al.* Swarming, schooling, milling: phase diagram of a data-driven fish school model. *New journal of Physics* **16**, 015026 (2014).

[11] Chou, H.-H. & Reggia, J. A. Emergence of self-replicating structures in a cellular automata space. *Physica D: Nonlinear Phenomena* **110**, 252–276 (1997).

[12] Tang, M. & Auffrey, C. Advanced digital tools for updating overcrowded rail stations: Using eye tracking, virtual reality, and crowd simulation to support design decision-making. *Urban Rail Transit* **4**, 249–256 (2018).

[13] Narain, R., Golas, A., Curtis, S. & Lin, M. C. Aggregate dynamics for dense crowd simulation. In *ACM SIGGRAPH Asia 2009 papers*, 1–8 (2009).

[14] de Gennes, P.-G. Soft matter (nobel lecture). *Angewandte Chemie International Edition in English* **31**, 842–845 (1992).

[15] Chambers, J. E. *et al.* An optical technique for mapping microviscosity dynamics in cellular organelles. *ACS nano* **12**, 4398–4407 (2018).

[16] Kue, C. S. *et al.* Recent strategies to improve boron dipyrromethene (bodipy) for photodynamic cancer therapy: an updated review. *Photochemical & Photobiological Sciences* **17**, 1691–1708 (2018).

[17] Dent, M. R. *et al.* Imaging phase separation in model lipid membranes through the use of bodipy based molecular rotors. *Physical Chemistry Chemical Physics* **17**, 18393–18402 (2015).

[18] Levitt, J. A. *et al.* Membrane-bound molecular rotors measure viscosity in live cells via fluorescence lifetime imaging. *The Journal of Physical Chemistry C* **113**, 11634–11642 (2009).

[19] Ogle, M. M. *et al.* Sensing temperature in vitro and in cells using a bodipy molecular probe. *The Journal of Physical Chemistry B* **123**, 7282–7289 (2019).

[20] Li, M., Zhang, Q., Zhou, Y.-N. & Zhu, S. Let spiropyran help polymers feel force! *Progress in Polymer Science* **79**, 26–39 (2018).

[21] Clough, J. M., Van Der Gucht, J. & Sijbesma, R. P. Mechanoluminescent imaging of osmotic stress-induced damage in a glassy polymer network. *Macromolecules* **50**, 2043–2053 (2017).

[22] Davis, D. A. *et al.* Force-induced activation of covalent bonds in mechanoresponsive polymeric materials. *Nature* **459**, 68–72 (2009).

[23] Kingsbury, C. M. *et al.* Shear activation of mechanophore-crosslinked polymers. *Journal of Materials Chemistry* **21**, 8381–8388 (2011).

[24] Klajn, R. Spiropyran-based dynamic materials. *Chemical Society Reviews* **43**, 148–184 (2014).

[25] Chen, Y. *et al.* Mechanically induced chemiluminescence from polymers incorporating a 1, 2-dioxetane unit in the main chain. *Nature chemistry* **4**, 559–562 (2012).

[26] Matsumoto, M. Advanced chemistry of dioxetane-based chemiluminescent substrates originating from bioluminescence. *Journal of Photochemistry and Photobiology C: Photochemistry Reviews* **5**, 27–53 (2004).

[27] De Vico, L., Liu, Y.-J., Krogh, J. W. & Lindh, R. Chemiluminescence of 1, 2-dioxetane. reaction mechanism uncovered. *The Journal of Physical Chemistry A* **111**, 8013–8019 (2007).

[28] Göstl, R. & Sijbesma, R. π-extended anthracenes as sensitive probes for mechanical stress. *Chemical science* **7**, 370–375 (2016).

[29] Freikamp, A., Mehlich, A., Klingner, C. & Grashoff, C. Investigating piconewton forces in cells by fret-based molecular force microscopy. *Journal of structural biology* **197**, 37–42 (2017).

[30] Zhang, Y., Ge, C., Zhu, C. & Salaita, K. Dna-based digital tension probes reveal integrin forces during early cell adhesion. *Nature communications* **5**, 1–10 (2014).

[31] Schuler, B., Lipman, E. A. & Eaton, W. A. Probing the free-energy surface for protein folding with single-molecule fluorescence spectroscopy. *Nature* **419**, 743–747 (2002).

[32] Qin, L. *et al.* Conformational transitions of polymer chains in solutions characterized by fluorescence resonance energy transfer. *Polymers* **10**, 1007 (2018).

[33] Nath, A. *et al.* The conformational ensembles of α-synuclein and tau: combining single-molecule fret and simulations. *Biophysical journal* **103**, 1940–1949 (2012).

[34] Cingil, H. E. *et al.* Monitoring protein capsid assembly with a conjugated polymer strain sensor. *Journal of the American Chemical Society* **137**, 9800–9803 (2015).

[35] Sahoo, H. Förster resonance energy transfer–a spectroscopic nanoruler: Principle and applications. *Journal of Photochemistry and Photobiology C: Photochemistry Reviews* **12**, 20–30 (2011).

[36] Medintz, I. L. & Hildebrandt, N. *FRET-Förster resonance energy transfer: from theory to applications* (John Wiley & Sons, 2013).

[37] Cingil, H. E., Boz, E. B., Wang, J., Stuart, M. A. C. & Sprakel, J. Probing nanoscale coassembly with dual mechanochromic sensors. *Advanced Functional Materials* **26**, 1420–1427 (2016).

[38] van de Laar, T. *et al.* Light from within: Sensing weak strains and femtonewton forces in single molecules. *Chem* **4**, 269–284 (2018).

[39] Kiriy, A., Senkovskyy, V. & Sommer, M. Kumada catalyst-transfer polycondensation: Mechanism, opportunities, and challenges. *Macromolecular rapid communications* **32**, 1503–1517 (2011).

[40] Geng, Y., Huang, L., Wu, S. & Wang, F. Kumada chain-growth polycondensation as a universal method for synthesis of well-defined conjugated polymers. *Science China Chemistry* **53**, 1620–1633 (2010).

[41] Yamamoto, T. *et al.* Preparation of π-conjugated poly (thiophene-2, 5-diyl), poly (p-phenylene), and related polymers using zerovalent nickel complexes. linear structure and properties of the π-conjugated polymers. *Macromolecules* **25**, 1214–1223 (1992).

[42] Kanbara, T., Saito, N., Yamamoto, T. & Kubota, K. Preparation and properties of poly (quinolinediyl) s and poly (isoquinoline-1, 4-diyl) with new π-conjugation systems. *Macromolecules* **24**, 5883–5885 (1991).

[43] Sakamoto, J., Rehahn, M., Wegner, G. & Schlüter, A. D. Suzuki polycondensation: Polyarylenes à la carte. *Macromolecular rapid communications* **30**, 653–687 (2009).

Chapter 2

Main chain spiropyran mechanochromic sensors

The molecular switching properties of spiropyran have been successfully harnessed in the development of dynamic materials using the distinct properties of its isomers. It has also been shown extension and modification of its pi-conjugated system alters its spectroscopic properties. However, the effect on molecular switching and isomerization kinetics of extension of its pi-conjugated system into a completely semiconducting material remains largely unexplored. In this chapter we present the synthesis of a fluorene-alt-spiropyran conjugated polymer and explore its spectroscopic properties in solution, varying the isomerisation of spiropyran and merocyanine within its semiconducting backbone. We stimulate this process with UV-irradiation and probe the influence of pH on both spectroscopic properties and back-conversion kinetics. We find that the spiropyran maintains a spectral response upon isomerization, however comparison with its molecular equivalent shows back-conversion kinetics are completely stalled. Additionally, we find the zwitterionic merocyanine once protonated is poorly soluble. Finally, we show there is no spectroscopic response to ultrasonic stimulation and explain previous reports of this effect by acid stimulated aggregation as a result of the ultrasonication process.

Manuscript in preparation as:

P. van der Scheer, H. Dekker and J. Sprakel: *Main chain spiropyran mechanochromic sensors*

2.1 Introduction

One of the large advances offered by the field of mechanochemistry in the past two decades has been the development of molecular probes in which an optical response is elicited upon action of a mechanical stress. Such optical mechanophores feature a central bond that is mechanically weak and that can be cleaved when a threshold force is exceeded. A wide variety of mechanophores has been developed in the past decades, with operating principles ranging from mechanically induced retro-Diels-Alder reactions to ring-strain promoted mechanical opening of cyclic molecules. One of the most commonly used optical mechanophores however is spiropyran, that features a central mechanically-weak spiro bond that when broken transforms the non-aromatic molecule into an aromatic species called merocyanine. The isomerization between spiropyran and merocyanine, which is reversible in many cases, thus acts as a molecular switch for conjugation. In addition to its mechanical sensitivity, spiropyran been widely used as a photoswitch, since also UV light can bias the isomerization reaction to the merocyanine state. Mechanical activation of spiropyran into merocyanine gives rise to a distinct colorimetric change in the material in which the mechanophore is embedded, which can be either detected based on light absorption[1, 2] or fluorescence[3, 4]. This approach has been extensively studied, for example to detect precursors for macroscopic mechanical damage in engineering polymers[5, 6, 7].

The optical signal elicited from spiropyran mechanophores only emerges when a threshold force is exceeded; single-molecule studies has shown this threshold force to be around 200 pN[8], about a tenth of the force required to break conventional covalent bonds. This binary (on-off) response limits their applicability to qualitive sensoric function where bond rupture can be detected but forces cannot be quantified. To resolve this issue, a different force sensing strategy has recently been developed in our group. This makes use of the coupling between polymeric chain conformation and fluorescent emission found in many conjugated polymers. Here either the vibronic fine-structure of the emission band shows distinct changes when mechanical forces stretch out the chain conformations, or these effects are amplified through the clever use of donor-acceptor energy transfer within the chain. [9, 10, 11] The energy transfer processes within the chain are strongly dependent on the local monomer density within the coil and can be tuned to give high dynamic range when either stretching or collapsing the polymer coil. The configuration of the coil can be coupled to a force by considering that the polymer chain is a large spring with a specific spring-constant. Its deformation, which can be read out optically, can be linked to a specific force. This makes it possible, after calibration, to optically read-out very small forces continuously over a certain force range.[12] This has been successfully used, e.g. by group of Bazan, to study the binding-induced conformational changes of conjugated polymer sensors by specific DNA sequences. [13, 14, 15, 10] In our group we have shown them to be capable of monitoring the formation of self-assembled nanostructures during electrostatic condensation. [10, 9] In addition to their greyscale optical response, conjugated polymers enable spatially-resolved force measurements, enabled by their high quantum yield and photostability. Especially at the single molecule level this is paramount to obtain high-resolution data.

In this Chapter, we aim to investigate if these beneficial properties of force-responsive conjugated polymers can be amplified by their combination with a small-molecule mechanoswitch: spiropyran. It has already been shown that it is possible to include the spiropyran into the backbone of a conjugated polymer with retention of its switchable spectroscopic properties.[16] By switching from SP to MC the conjugated system is extended and opened-up from its neighbouring monomers through the MC effectively increasing the conjugation length. For polyfluorene the spectroscopic dependence on conjugation length has been studied extensively.-[17, 18] There is both a blue-shift in absorption and emission accompanied with an increase of the fluorescence quantum efficiency. If we now

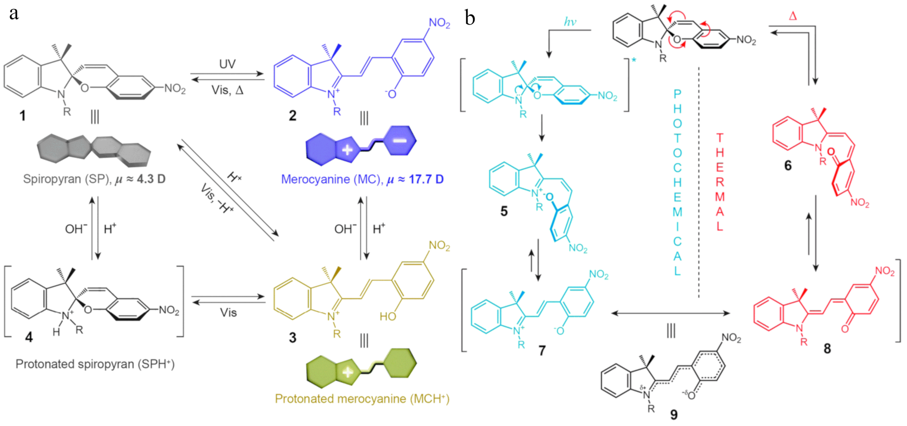

Figure 2.1: a) The structures of SP (1), MC (2), protonated merocyanine MCH+ (3) and protonated spiropyran SPH+ (4) as a result of photo- and acidochromism. b) The transition of spiropyran to merocyanine as a result of thermal and photochemical isomerisation. Reprinted with permission from [1]. Copyright 2013 by the royal society of chemistry.

take an alternating polymer of SP and fluorene and exert a force until we obtain an alternating polymer of MC and fluorene we expect a step wise conversion of SP to MC. This step wise conversion is accompanied by a spectroscopic response unique to the conjugation length of the segments which in turn can be coupled to the force exerted on the polymer. The spiropyran cascade combines the photo-stable and high quantum yield properties of conjugated polymers which that of a continuous response with respects to the mechanic stimuli of its direct environment hereby increasing the dynamic range of its use as a mechanochromic sensor.

In this chapter we explore the design of an alternating main-chain spiropyran-fluorene conjugated polymer and its application as a mechanochromic sensor. We do this by synthesizing a monomer suitable for Suzuki-Miyaura polymerisation[19, 20, 21, 22] and subsequently co-polymerize it with fluorene. We can now study the spectroscopic properties of the obtained alternating spiropyran-flourene main-chain conjugated polymer under exposure of different external stimuli exploring its applicability as a mechanochromic sensor. We put these results in context by comparing them with the well known response of nitro-spiropyran under identical stimuli.

2.2 Results & Discussion

To synthesize an alternating spiropyran-fluorene polymer we first synthesize a spiropyran with reactive groups suitable for Suzuki-Miyaura polymerisation. To extend the mechanochromic properties of the spiropyran in the direction of the backbone the reactive groups need to be positioned on the two outer phenyl rings.[23, 24] To achieve this building blocks containing bromide on the desired positions were used in the synthesis of a dibrominated spiropyran following a procedure from literature [16]. Analysis using ^{H}-NMR showed the product to be chemically pure. This monomer was subsequently used to synthesize an alternating spiropyran-fluorene main-chain mechanochromicsensor using Suzuki--Miyaura polycondensation[16, 21, 25, 26]. Gel permeation chromatography showed the polymer to have an M_w of 34kD. All monomer and oligomer fractions were removed from the sample by a soxhlet extraction protocol. Hereby minimizing any chain-length effects. [27] Note that the chemical nature of the Suzuki-Miyaura coupling ensures the alternating sequence of the spiropyran and fluorene moieties in the polymer backbone and only chain length variations are possible.

To determine whether the mechanochromic properties of the spiropyran are maintained after polymerization we conduct a spectroscopic study aimed at activating the MC form of the molecule which can be spectrally separated from the SP. To validate our methods of conversion to MC we also include reference experiments conducted on nitro-spiropyran (nitro-SP) which has shown to open under various conditions displaying changes in spectroscopic properties.[28, 1] This also enables us to compare rate constants and activation energies accompanying these pro-

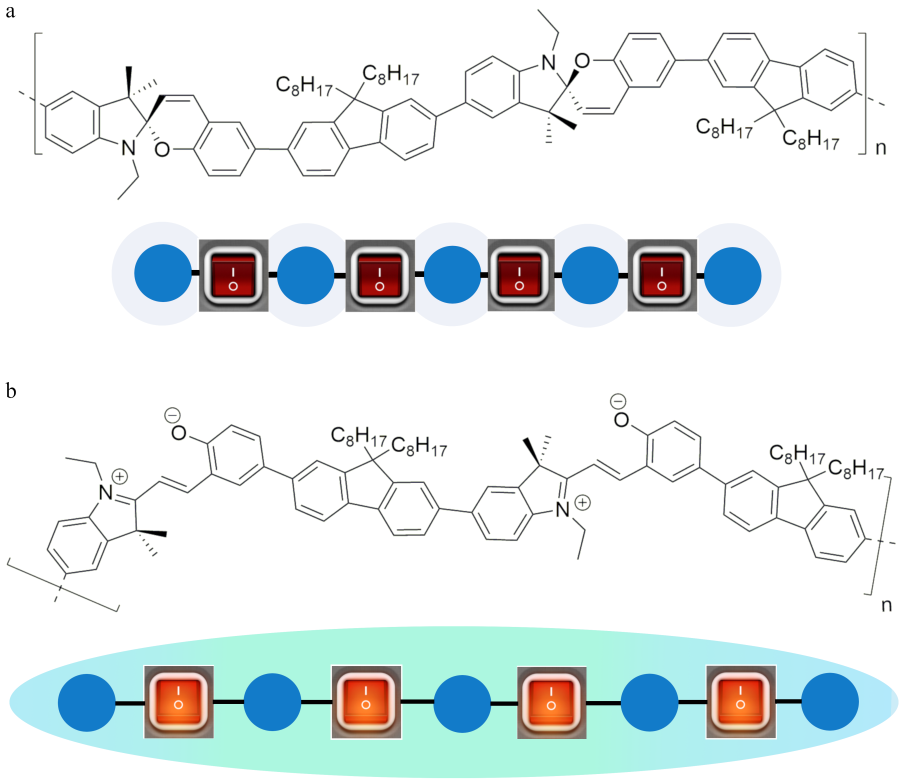

Figure 2.2: a) The chemical structure of p(SP-alt-F8) with a schematic representation where F8 is depicted as a blue circle and spiropyran as an off switch. The conjugation of the backbone is interrupted by the spiropyran resulting in low fluorescence quantum yield. b) The chemical structure of p(MC-alt-F8) and a schematic depiction of the now non-interupted conjugation resulting in high fluorescence quantum yield and emission along the complete backbone and elongation of the chain.

cesses.

We use the fact that the SP molecule shows photochromism in solution-[29, 30, 31, 32], enabling conversion from the SP to MC form by activation by UV-irradiation and MC to SP conversion under irradiation with green light.[28, 1] To first determine the equilibrium spectroscopic properties of the p(SPF8) and its p(MCF8) form compared to that of the nitro-SP and nitro-MC we chose to use UV-irradiation to switch between conformations. First excitation and emission spectra of reference spiropyran compound 1,3,3-trimethylindolino-6'-nitrobenzopyrylospiran (nitro-SP) were recorded shown in figure 2.3a, for the SP form and the UV-irradiated MC form.

In the closed state the nitro-SP absorbs mainly at 450 nm and has very low fluorescence emission. The open MC form absorbs strongly at 600nm and has a strong emission at 625nm.

We now determine the equilibrium spectroscopic properties of the p(SPF8) and that of its p(MCF8) form by measuring absorption and fluorescence emission spectra in solution before and after irradiation with UV, as shown in 2.3b-c. The activation of the spiropyran monomers to their merocyanine state can be readily seen in the changes in the absorption spectrum. The activated p(MCF8) form can be clearly distinguished from the native p(SPF8) form by the emergence of a new absorption band, in the visible range, that signals the newly formed and colored merocyanine. Also in the fluorescence, a distinct optical effect is seen. First, we observe a weak blue-shift when the switches are toggled on. This is surprising, as it is conventional wisdom that extension of the pi-conjugated system of these polyfluorene-based macromolecules should lead to a red-shift in the fluorescence emission [33]. Moreover, we observe a 6-fold increase in fluorescence intensity, signalling a 6-fold change in quantum efficiency, upon spiropyran activation.

Both effects are surprising and not as expected. If the spiropyran moieites in the main chain are all closed, the conjugated structure should be limited to a single fluorene monomer flanked by two phenyl rings. Such a small conjugated structure should have marginal fluorescence in the visible range. By contrast, once the SP is isomerized to its MC form, the conjugated structure can extend over many monomeric units. We expected this to lead to both a strong redshift, and a drastic increase in fluorescence. Neither effect is observed.

While a conclusive answer to why this occurs is currently not available, we can make a speculation. It is known that the isomerization reaction SP $\rightleftharpoons$ MC exists in a dynamic equilibrium. Even in the absence of light or force, a small fraction of SP will be in the MC state. It is also possible that the incorporation of SP within a semiconducting chain biases this equilibrium to the MC state. This could imply that even in the native state, larger conjugated structures exist within these copolymer chains that lead to finite fluorescence emission without purposeful activation. Even though no clear MC signal can be detected in the absorption spectra of the native product, opening of a small percentage of the SP mechanophores could lead to distinct fluorescence signal. Moreover, making these optical measurement invariable involves illuminating the sample with near-UV light, which could contribute to undesired activation while performing the measurement.

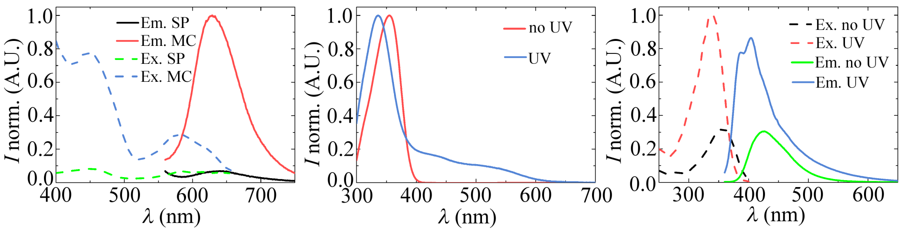

Figure 2.3: a) excitation and emission spectra of Nitro-SP and nitro-MC in DCM. $\lambda_{EX} = 540nm$ b) absorption spectra of p(SPF8) in DCM with and without UV-irradiation c) exciation and emission spectra of p(SPF8) in DCM before and after UV-irradiation. $\lambda_{EX} = 350nm$

One particularly useful function of the spiropyran mechanophore is that its opening is thermally reversible. Removal of the opening trigger (light and/or force) should lead to backconversion into the native equilibrium. To ascertain if such reversibility is maintained in the semiconducting backbone we perform backconversion kinetics experiments. The rate constant of MC>SP isomerization can be determined from the evolution of the MC fluorescence emission band in time. We find a distinct decay in emission intensity with time upon removal of the UV trigger (Figure2.4 a). These data is well described by a simple exponential decay describing first-order reaction kinetics $\frac{[I]_t}{[I]_0} = e^{-kt}$[34], where k is the reaction rate constant and t the time.

Since the measurement itself exposes the light-sensitive material to light, this could influence the determination of the rate constant. To mitigate this, we perform measurements with different sampling (and thus illumination) intervals to vary the light exposure during the measurement. For short time intervals Δt, and thus high light exposures during the measurement, we indeed find a dependence of the reaction-rate constant and measurement settings. Only for measurements with a time delay between acquisitions of 30 seconds or more, we find this dependency to be lost, thus representing the true thermodynamic reaction-rate constant.

To verify if the ring closure involved in MC>SP conversion is thermally-activated, we perform a series of experiments at different temperatures. We find that indeed the ring closure is accelerated at increased temperatures, and well described by the Arrhenius equation $k = Ae^{E_a/RT}$ [30]. From these data, we determine an activation energy of 71.8 $kJmol^{-1}$ which corresponds to values found in literature [35, 36].

To determine if the same equilibrium is maintained when SP is incorporated in the main chain of a semiconducting polymer, we performed kinetic experiments also for p(MCF8). Neither fluorescence, absorption nor NMR showed any back-conversion of the merocyanines inside the semiconducting chains on timescales of up to 4 days. This is a large contrast with the thermal back-conversion of the small molecule nitro-MC, which occurs within 15 minutes. Literature suggests that for spiropyrans as pendant sidechains on polymers, there is a sterical barrier to isomerise back from MC to SP, which leads to MC forms being stable for months. [37] This effect could be amplified in this spiropyran main chain polymer, as the MC to SP transition involves a rotation around the central spiro-carbon bond, which is very hindered by the fact that this motion involves dragging the entire chain through the viscous medium. However, literature experiments on main-chain spiropyran polymers that do not have a semiconducting backbone show rapid back-conversion within 5 minutes [24]. This appears to rule out this possible explanation, while being at odds with other literature data on pendent (side-chain) spiropyran polymers [37].

Another reason for the arrest of the back-conversion kinetics could be a specific effect of the semiconducting polymer. The de-localised electron configuration along the backbone also changes the electron distribution on the MC monomers. This could lead to electronic stabilisation of the open state. This would also imply that in a non-triggered state, the equilibrium SP $\rightleftharpoons$ MC should also be biased towards the MC state, which is in line with our hypothesis to explain the smaller-than-expected effect of the switching on the polymer luminescence. We finally note that stimulation of MC with green light is known to increase the conversion rate to the SP form. Irradiation of p(MCF8) with high-intensity green light for up to 4 hours did not lead to noticeable back-conversion, further supporting the hypothesis that the incorporation of spiropyran into the extended conjugated system alters the isomerization equilibrium fundamentally.

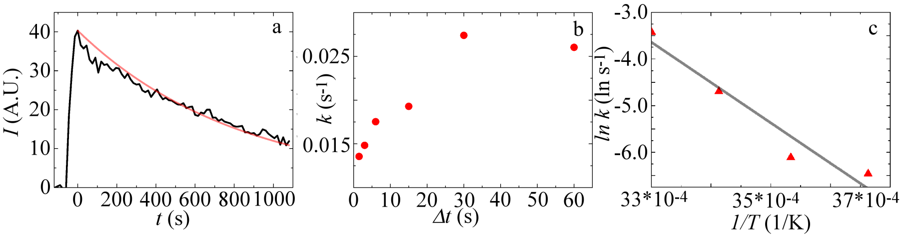

Figure 2.4: a) MC to SP relaxation rate constants (k) after irradiation with UV-light as a function the intervals between points. Averaging time = 0.1s b) Emission intensity at $\lambda_{EM} = 675nm$ of nitro-SP in DCM after UV-irradiation as a function of time. Irradated from t = -60 to 0. c) Natural logarithm of reaction constant (k) as a function of the inverse temperature

To further investigate the differences in electronic properties of the nitro-SP and the p(SPF8) we attempted to force the equilibrium of SP and MC to the open form .[38] Temperature-dependent fluorescence and NMR measurements (0 °C to 30 °C) did not indicate a distinguishable amount of p(MCF8) being formed. This further supports the hypothesis that there is a high energy barrier between the p(SPF8) and p(MCF8) form, which cannot easily be crossed without the very intense UV light that is applied.

To further explore the nature of the increased stability of the p(MCF8) compared to that of the nitro-MC we now investigate the influence of pH. Since the open MC conformation contains an oxygen cation in aprotic environments this is susceptible to protonation. This not only influences the local electronic environment but also changes the energetic landscape of the molecule and alters its polarity.[1]

To study this equilibrium, samples of p(SPF8) with an excess of acetic acid are prepared. Two sequences are used: a solution of p(SPF8) is treated with acetic acid and then switched to the p(MCH+F8) state using UV irradiated, another solution is first switched to p(MCF8) by UV irradiation and then acetic acid is added transforming it to p(MCH+F8). We effectively explore the three routes shown in 2.1a. For both sequences the absorption spectra are recorded 2.5a-c.

First we explore addition of acid after UV-irradiaton. This route is limited to three states as shown in figure 2.1a. The ground-state p(SPF8), the opened p(MCF8) state after UV-irradiation and p(MCH+F8) which is obtained after protonation of p(MCF8). We compare absorption spectra in 2.5a. We can see the distinct blue shift of the main peak from 360 to 340nm; this band is the absorption band of the fluorene monomers, whose position changes in response to the switching of the adjacent responsive monomers. The coupling of the fluorene spectral response to the state of the photoswitch, makes it possible to evaluate the photoswitch state even when its own spectral shift is obscured. This shift is maintained after protonation of p(MCF8) to obtain p(MCH+f8), indicating that changes in the spectrum after protonation are not due to back-conversion into p(SPF8). The absorption bands at 450 and 550 nm associated with the MC are present in both the p(MCF8) and p(MCH+F8). Just as in 2.3b their features are broadened compared to the bands of the MC in 2.3a, as is expected due to the broad distribution of states in a polymer. There is a slight decrease in intensity in the p(MCH+F8) band compared to that of the p(MCF8), however their mutual ratios remain unchanged. Either the p(MCF8) and p(MCH+F8) states cannot be distinguished spectroscopically or the solvent itself contains protons which cause inmediate conversion of p(MCF8) to p(MCH+F8).

The second route of protonation before UV-irradiation also has three possible states; there are distinct pathways that can lead to the final state. The p(SPF8) upon protonation can open directly to the p(MCH+F8) state of form an intermediate p(SPH+F8) state as shown in 2.1a. This p(SPH+F8) state upon UV-irradiation can be transformed into p(MCH+F8). In 2.5b we plot the absorption spectra of p(SPF8) solution after addition of acid, then after UV-irradiation and we repeat this last measurement after 20 hours. Upon addition of acid to the p(SPF8) sample we can see an increase of absorption across the whole spectrum. The sample does show slight turbidity after addition of acid, this could signal the induced in-

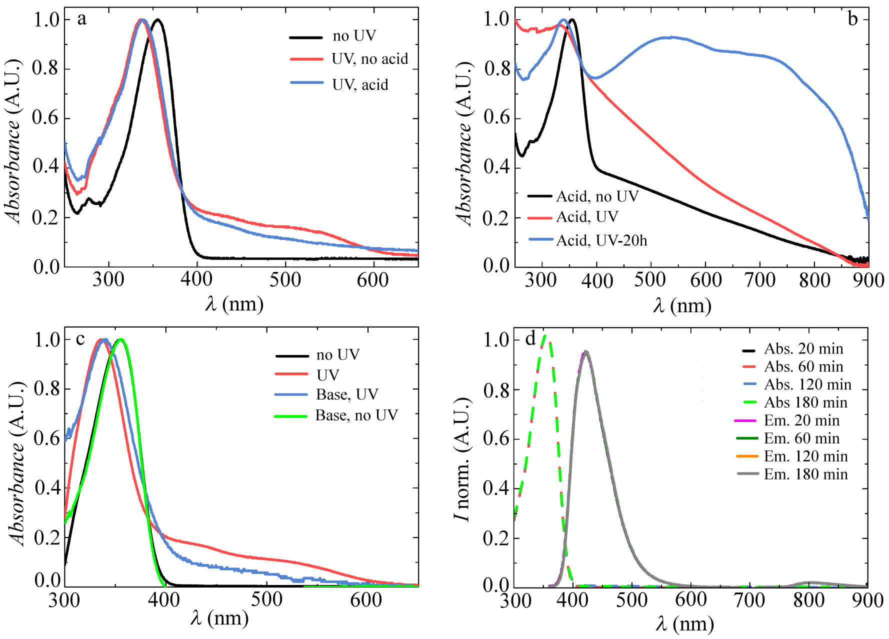

Figure 2.5: a) Absorption spectra of p(SPF8) in DCM comparing influence of acid added after UV-irradiation b) absorption spectra of p(SPF8) with acid before and after irradiation with UV c) absorption spectra of p(SPF8) comparing influence of base and UV-irradiation d) absorption and emission spectra of p(SPF8) in THF under the influence of ultrasound at different exposure times. $\lambda_{EX} = 350nm$.

solubility, and resulting formation of aggregates, due to the opening and protonation of the photoswitch. In fact, induced insolubility is one of the features of spiropyran materials that has been used to create a switchable response (ref review article). The large difference in absorption spectrum upon addition of acid is most likely caused by insolubility of the polymer and not by conformational changes of the switch itself.

We can also see that only the two spectra after UV-irradiation show the blue-shift of the fluorene absorption band connected to the opening of the SP to the MC. This seems to indicate that addition of acid does not spontaneously cause transformation of p(SPF8) into p(MCH+F8) as is indicated for non-polymeric spiropyran. After UV-irradiation we can see that the absorption across the complete spectrum increases even further and we now see the blue-shift of the fluorene band at 340nm. After 20h. the spectrum shows two distinct bands at 550 and 750nm. It is however difficult to attribute these to any changes in conformation due to the apparent solubility issues the p(MCH+F8) seems to have. It can however be said that no back-conversion to p(SPF8) can be observed. The absorption band at $750nm$ could be caused by stacking of the very flat rigid backbone of the now open MCH^{+}F8 which would lead to even lower energies. The emergence of this stacking could be caused by the absence of the negative charge on the oxygen of the spiro unit making it more likely to stack.[39, 34] This additional stability of the p(MCH+F8) in a stack could additionally hinder back-conversion as we observed. In contrast to the absorbance measurements the fluorescence emission do not show change upon addition of acid, the spectrum proves to be only dependent on UV irradiation of the sample.

As a control, we now repeat the experiment in the presence of base. The presence of base restricts the possible states to that of the p(SPF8) and the non-protonated p(MCF8) and removes any uncertainty of the role of acidic impurities present in the solvent. The influence of the presence of the base pyridine on the spectral properties of p(SPF8) are shown in figure 2.5c. A small spectral change can be seen in the region between 400 and 600 nm. These changes are however too weak to assign any physical interpretation to them. These spectra do act as negative control to the UV-irradiation measurements without acid or base. It can be ruled out that the presence of p(MCF8) in the UV-irradiation measurements is caused acidic impurities.

Now that we know the spectral response of the p(SPF8) and p(MCF8) by opening with UV-irradiation and the influence of pH we can explore the possible applications of the polymer as a mechanochromic sensor. This requires mechanical opening of the p(SPF8) to its p(MCF8) form which we try to achieve by ultrasonication.[16, 24] A solution of p(SPF8) in THF was ultrasonicated for up to 180 minutes. THF was used instead of DCM, because chlorinated solvents can form acid upon ultrasonication [40], which influences the p(SPF8) to p(MCF8) equilibrium as shown before. Ultrasonication did not result in a significant change in fluorescence and absorbance, as can be seen in figure 2.4d.

Interestingly, this result of the lack of mechanical opening in the main chain conjugated polymer is in contrast to the result obtained by Sommer and Komber [16] where they report the apparent mechanical activation of the identical polymer. The molecular weights are very similar in both cases, thus ruling out a chain-length dependent mechanical susceptibility effect. Rather, the experiments of Sommer and Komber were conducted in DCM. Since it is known that DCM can generate acidic species under ultrasonication [40], and we have shown above that acid alone is sufficient to open SP partly in these polymers, this triggers the question if the reported positive result of mechanochemical opening is not a secondary effect due to solvent degradation. A more controlled way of confirming mechanochromism could be embedding the sensor into a polymer matrix where upon bulk deformation of the material deformation of the sensor would also occur. [25]

2.3 Conclusions

A poly-spiropyran-*alt*-dioctylfluorene alternating copolymer p(SPF8) is succesfully synthesised, with a representative molecular weight for Suzuki-Miyaura polymerisation, M_w of 25 respectively 34 kDa and a PDI of 2.5 respectively 2.9. The expected structure has been confirmed with NMR.

However the amplified effects of combining the mechanochemical properties of conjugated polymers and mechanochemical sensors directly into the conjugated structure of the former were not found. The main reason being the non-reversible opening of the spiropyran switches and poor mechanical activation. These result in an increase of fluorescence quantum yield and spectral changes but remain unresponsive after the initial opening. Spectroscopic analysis and comparison with literature showed energetic stabilization to be an important factor in this. The augmentation of the extended pi-conjugated system cannot be avoided in the current design and requires new approaches. Both fluorescence quantum yield effects and spectral changes in the spectrum upon activation indicate that the principle design was valid. The cause of the poor mechanical activation remains unclear. The results in the this work do provide us with design rules which we can use to improve and expand upon the current design.

A method which has been successfully applied is the cycloaddition of malemide and anthracene.[41, 42] This reaction results in a thermally stable covalent bond and quenches the fluorescent emission of anthracene by reducing the size of the conjugated system. Unlike the complex and sensitive equilibria of the spiropyran and merocyanine the anthracene-malemide bond is only sensitive to mechanical bond breaking. The use of this coupling has also been shown compatible with polymeric systems. Malemide terminated PEG was used to graft to polystyrene with pendant anthracene. [43] They also show that fluorescence emission of the anthracene is quenched after cycloaddition.

By incorporating the anthracene into a fluorene backbone this effect could be amplified by the increased size of the conjugated system. Furthermore fluorene shows spectral dependence on conjugation length which can additionally give information about the amount of neighbouring free anthracene units which could function as an internal standard. This approach would also allow for control of the chemistry and length of the polymer tether attached to the malemide independently of the backbone. Here there are no complications arising from the extention of the conjugated system and we gain control of the polymeric tether attached to the bond-breaking site independent of the sensor itself.

Because the polyfluorene based conjugated polymer sensors already posses mechanochromic properties it would be beneficial to expand this with additional sensing applications. One such property relevant to the mechanical properties of local environments is the viscosity or free volume. Various sensors have been developed where the fluorescent properties depend on the viscosity or free volume of its local environment.[44, 45, 46] Since we have no indication that the chemistry in the current work inhibited the function of the spiropyran we propose a similar strategy in exploring the incorporation of viscosity probes into the conjugated backbone of polyfluorene. The working principle of such probes is based on fluorescence decay pathways availability depending on the unhindered rotation over certain bonds in the molecule. Which are a steric issue and not one of local electronic environment. Furthermore they probe a different lengthscale and force range compared to that of the mechanochromic sensing capability of the polyfluorene backbone.

The combination of the probing capabilities of small molecules with those of the mechanochromic conjugated polymers shows much promise. We have successfully showed the limits of the incorporation of spiropyran in this current design and used this information in the construction of other designs.

2.4 Methods

Chemicals

All chemicals used in synthesis are purchased from Sigma-Aldrich or TCI chemicals and used as received. Solvents are obtained from BioSolve and also used without further purification unles mentioned otherwise.

NMR

Spectra are recorded on a Bruker Avance III 400 MHz spectrometer. Shifts are presented in parts per million (ppm) and referenced to tetramethylsilane (TMS) (0.0 ppm). Solvents used are specified with the provided NMR spectra or data. Standard abbreviations indicating multiplicity were used as follows: s (singlet), b (broad), d (doublet), t (triplet), q (quartet), m (multiplet), dd (doublet of doublets), and td (triplet of doublets). Concentration for NMR spectra are between 5 and 10 mg mL^{-1}.

UV-VIS and fluorescence spectroscopy

UV-VIS absorbance spectra are recorded on a Shimadzu UV-2600 UV-VIS spectrometer with temperature controller. Fluorescent experiments are conducted on a Cary Eclipse Fluorescence Spectrometer with temperature controller. Measurements are performed in signal-to-noise mode with an signal-to-noise ratio of 1000. Concentrations of spectroscopy samples are $\approx 1 * 10^{-2}$ mg mL^{-1}. When no temperature is specified, spectroscopy measurements are performed at 20 °C. For time-dependent spectroscopy experiments, the cuvette is put immediately in the spectrometer after UV irradiation and left to decay thermally in the dark in the spectrometer while measuring a spectrum every 10 or 30 minutes.

UV irradiation

UV irradiation experiments are performed using an Omnicure Series 1500 200W UV lamp, at 100% laser power for 90s (unless specified otherwise). λ_{max} is 365 nm. UV irradiation for spectroscopy measurements is performed in the cuvette, with the lamp above the open cuvette, in a dark room. Cuvettes are then sealed, mixed and immediately measured. UV irradiation for NMR measurements is performed in a glass vial then transferred to an NMR tube which is kept under light-poor conditions up-to and during the measurements.

GPC

Gel permeation chromatography (GPC) is performed on an Agilent Tech 1200 series machine with SEDEX Model 90 LT-ELSD detector. Measurements are performed at 35 °C in THF. A polystyrene calibration standard is used. Correction factor of 2.7 (literature value for polyfluorenes [47]) is used to correct for polymer rigidity compared to polystyrene.

Ultrasonication experiments

A bandelin Sonopulse GM70 ultrasonic needle is used. Ultrasonication is performed continuously with a relative pulse strenght of 72%. A sample of 5.7 mg p(SPF8) in 10 mL THF is prepared in a 22 mL glass vial. While ultrasonicating, it is cooled on ice. After a certain ultrasonication time, a 50 μL aliquot is taken from the sample and diluted to a final concentration of $\approx 1 * 10^{-2}$ mg mL^{-1} for spectroscopy measurements.

Synthesis

In this section first the synthesis of the spiropyran monomer 5',6-bis(bromo)-1',3',3'-trimethylspiro-[2H-1-benzopyran-2,2'-indoline] (**SP**) is described, followed by the polymerisation of this monomer with fluorene derivative 9,9-dioctylfluorene-2,7-diboronic acid bis(1,3-propanediol) ester (**F8**) to give the desired polymer **p(SPF8)**.

5-Bromo-2,3,3-trimethyl-3H-indole (**1**)

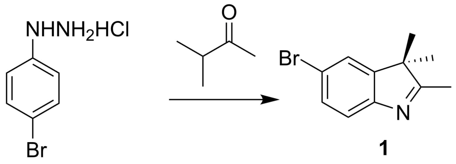

To a 250 mL round-bottom flask is added 15 g (67.1 mmol) bromophenylhydrazine HCl, 8.3 mL (135 mmol) 3-methylbutanone and 90 mL glacial acetic acid. The mixture reacted at reflux for 20 h and cooled to room temperature. A colour change from a dark grey suspension to a bright red solution is visible. The volatile components are removed under vacuum, the resulting red oil is partitioned between petroleum ether (100 mL) and brine (50 mL). The organic layer is washed a twice with 50 mL of brine. The organic fractions are dried (MgSO4), filtered, and evaporated under vacuum to yield **1** (12.68 g, 53.2 mmol, 79%).

Column chromatography and distillation are both unsuccessful to isolate product **1**, the crude was used in subsequent synthesis steps.

5-Bromo-1-ethyl-2,3,3-trimethyl-3H-indolium iodide (**2**)

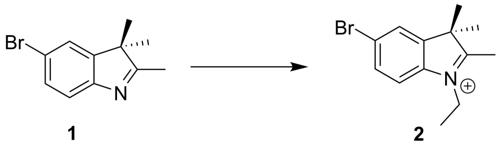

To a 100 mL round-bottomed flask is added 9.17 g (38.5 mmol) **1** and 25 mL acetonitrile and subsequently deoxygenated. To the mixture 20 mL of deoxegenated ethyl iodide is then added. The reaction is deoxegenated further and left to reflux for 48 h. Subsequently, the volatile components are removed under reduced pressure. The residue is triturated with ether (100 mL) to give a solid. The solid is filtered off, washed with ether (2 x 150 mL), and dried under vacuum to yield **2** as a dark red solid solid (13.41 g, 35.3 mmol, 91.6 %)

The crude product is recrystallized, yielding of 6.16 g of purified **2** (16.2 mmol, 42.1%).

1H NMR (400 MHz, DMSO-d6) δ 8.17 (d, J = 1.9 Hz, 1H), 7.93 (d, J =

8.5 Hz, 1H), 7.84 (dd, J = 8.5, 2.0 Hz, 1H), 4.47 (q, J = 7.3 Hz, 2H), 3.90 (d, J = 16.8 Hz, 1H), 2.81 (s, 3H), 1.53 (s, 6H), 1.41 (t, J = 7.3 Hz, 3H), 1.25 (s, 1H).

5’,6-bis(bromo)-1’,3’,3’-trimethylspiro-[2H-1-benzopyran-2,2’-indoline](**3**)

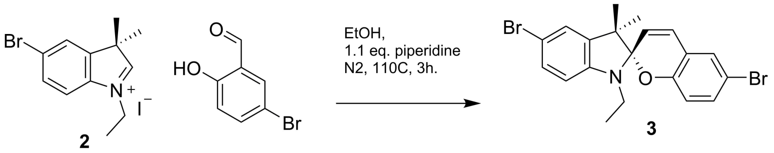

2.23 g (5.87 mmol) **2** and 1.15 g (5.72 mmol) 5-bromosalicylaldehyde are dissolved in 50 mL ethanol. Piperidine, 1.1 equivalent, is added and the mixture is deoxygenated. The mixture is reacted at 110 °C for 3 hours under N_2, subsequently the solvent is removed under reduced pressure. Recrystallizing twice yields a white solid **3** (1.69 g, 37.5 mmol, 66 %).

1H NMR (400 MHz, Chloroform-d) δ 7.25 (dd, J = 8.3, 2.0 Hz, 1H), 7.20 (d, J = 2.5 Hz, 1H), 7.17 (s, 1H), 7.14 (d, J = 2.0 Hz, 1H), 6.77 (d, J = 10.3 Hz, 1H), 6.62–6.53 (m, 1H), 6.41 (d, J = 8.2 Hz, 1H), 5.69 (d, J = 10.3 Hz, 1H), 3.22 (ddt, J = 53.8, 14.8, 7.3 Hz, 2H), 1.26 (s, 3H), 1.19-1.09 (m, 6H).

Suzuki polymerisation **p(SPF8)**

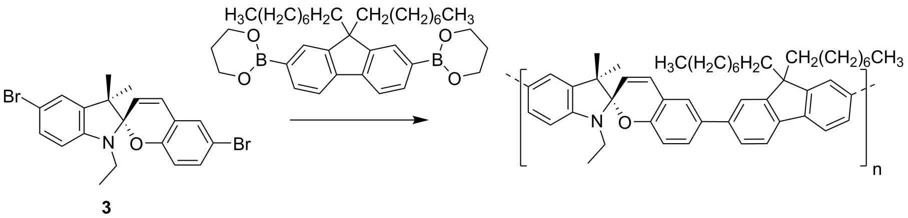

To a 20 ml microwave vial were added 197,6 mg (0.44 mmol) (**3**) and 245,6 (0.44 mmol) 9,9-Dioctylfluorene-2,7-diboronic acid bis(1,3-propanediol) ester and 100.4 mg tetrabutyammonium bromide (TBAB) which are subsequently dissolved in 6 ml toluene. To this 4 ml potasssium carbonate solution (2M) is added. The mixture is stirred heavily and deoxygenated. The vial is closed with a septum, degassed and backfilled with N_2 (5x). Under N_2 6 mg 1,1'-bis(diphenylphosphinoferrocene)dichloropalladium is added and the vial is crimp sealed, degassed and backfilled with N_2. The mixture was reacted at 80 °C for 96 hours.

The mixture was left to cool to room temperature, and extracted with brine. The aqueous layer is washed three times with DCM. The bulk of the organic solvent is evaporated under reduced, dissolved in a minimal amount of THF and precipitated in cold methanol, yielding a brown solid which is filtered into a Soxhlet thimble. The product is extracted with methanol, acetone and chloroform. The chloroform fraction was recovered and used in subsequent experiments.

A second bath of polymer was prepared under identical conditions using: 575.0 mg (1.28 mmol) **3**, 714.7 mg (1.28 mmol) 9,9-Dioctylfluorene-2,7-diboronic acid bis(1,3-propanediol) ester, 202.0 mg TBAB, 12.0 mg Pd(dppf)Cl_2 in 12 ml toluene and 8 ml potasssium carbonate solution (2M).

Batch 1 yields 130.0 mg p(SPF8) (44%) and batch 2 yields 385.0 mg (44%). GPC analysis shows M_w (kg/mol): 25.0 & 34.1 and PDI: 2.52 & 2.87 for batch 1 and 2 respectively.

These results are similar to the M_w's and PDI's in literature for a Suzuki polymerisation with similar monomers. [16]

Batch 1: 1H NMR (400 MHz, Chloroform-d) δ 7.66 (d, J = 8.0 Hz, 2H), 7.48 (dd, J = 18.7, 10.1 Hz, 5H), 7.35 (dd, J = 22.4, 8.8 Hz, 3H), 6.91 (d, J = 10.2 Hz, 1H), 6.77 (d, J = 8.3 Hz, 1H), 6.60 (d, J = 8.1 Hz, 1H), 3.64 (s, 0H), 3.45-3.09 (m, 2H), 1.38 (s, 3H), 1.18 (dd, J = 12.4, 7.0 Hz, 6H), 1.02 (s, 14H), 0.78-0.69 (m, 7H), 0.66 (s, 5H).

Batch 2: 1H NMR (400 MHz, Chloroform-d) δ 7.66 (d, J = 8.0 Hz, 1H), 7.47 (dd, J = 19.0, 10.3 Hz, 2H), 7.44-7.26 (m, 1H), 6.90 (d, J = 10.1 Hz, 1H), 6.77 (d, J = 8.3 Hz, 1H), 6.59 (d, J = 8.2 Hz, 1H), 5.72 (d, J = 10.1 Hz, 1H), 3.29 (dd, J = 58.5, 7.7 Hz, 1H), 1.97 (s, 2H), 1.43 (s, 0H), 1.38 (s, 1H), 1.29-1.08 (m, 3H), 1.13 (s, 6H), 1.01 (s, 7H), 0.75 (dddt, J = 11.0, 7.3, 5.6, 2.2 Hz, 4H), 0.66 (s, 2H).

References

[1] Klajn, R. Spiropyran-based dynamic materials. *Chemical Society Reviews* **43**, 148–184 (2014).

[2] Tyer Jr, N. W. & Becker, R. S. Photochromic spiropyrans. i. absorption spectra and evaluation of the. pi.-electron orthogonality of the constituent halves. *Journal of the American Chemical Society* **92**, 1289–1294 (1970).

[3] Li, C., Zhang, Y., Hu, J., Cheng, J. & Liu, S. Reversible three-state switching of multicolor fluorescence emission by multiple stimuli modulated fret processes within thermoresponsive polymeric micelles. *Angewandte Chemie International Edition* **49**, 5120–5124 (2010).

[4] Zhu, L. *et al.* Reversibly photoswitchable dual-color fluorescent nanoparticles as new tools for live-cell imaging. *Journal of the American Chemical Society* **129**, 3524–3526 (2007).

[5] Lee, C. K. *et al.* Exploiting force sensitive spiropyrans as molecular level probes. *Macromolecules* **46**, 3746–3752 (2013).

[6] Beiermann, B. A. *et al.* Environmental effects on mechanochemical activation of spiropyran in linear pmma. *Journal of Materials Chemistry* **21**, 8443–8447 (2011).

[7] Li, M., Zhang, Q. & Zhu, S. Photo-inactive divinyl spiropyran mechanophore cross-linker for real-time stress sensing. *Polymer* **99**, 521–528 (2016).

[8] Gossweiler, G. R., Kouznetsova, T. B. & Craig, S. L. Force-rate characterization of two spiropyran-based molecular force probes. *Journal of the American Chemical Society* **137**, 6148–6151 (2015).

[9] Cingil, H. E. *et al.* Monitoring protein capsid assembly with a conjugated polymer strain sensor. *Journal of the American Chemical Society* **137**, 9800–9803 (2015).

[10] Cingil, H. E. *et al.* Illuminating the reaction pathways of viromimetic assembly. *Journal of the American Chemical Society* **139**, 4962–4968 (2017).

[11] Cingil, H. E., Boz, E. B., Wang, J., Stuart, M. A. C. & Sprakel, J. Probing nanoscale coassembly with dual mechanochromic sensors. *Advanced Functional Materials* **26**,

1420–1427 (2016).

[12] van de Laar, T. *et al.* Light from Within: Sensing Weak Strains and FemtoNewton Forces in Single Molecules. *Chem* **4**, 269–284 (2018).

[13] Gaylord, B. S., Heeger, A. J. & Bazan, G. C. Dna hybridization detection with water-soluble conjugated polymers and chromophore-labeled single-stranded dna. *Journal of the American Chemical Society* **125**, 896–900 (2003).

[14] Hong, J., Hemme, W., Keller, G., Rinke, M. & Bazan, G. Conjugated-polymer/dna interpolyelectrolyte complexes for accurate dna concentration determination. *Advanced Materials* **18**, 878–882 (2006).

[15] Feng, L., Liu, L., Lv, F., Bazan, G. C. & Wang, S. Preparation and biofunctionalization of multicolor conjugated polymer nanoparticles for imaging and detection of tumor cells. *Advanced Materials* **26**, 3926–3930 (2014).

[16] Sommer, M. & Komber, H. Spiropyran main-chain conjugated polymers. *Macromolecular Rapid Communications* **34**, 57–62 (2013).

[17] Klaerner, G. & Miller, R. D. Polyfluorene derivatives:effective conjugation lengths from well-defined oligomers. *Macromolecules* **31**, 2007–2009 (1998).

[18] Jo, J., Chi, C., Höger, S., Wegner, G. & Yoon, D. Y. Synthesis and characterization of monodisperse oligofluorenes. *Chemistry–A European Journal* **10**, 2681–2688 (2004).

[19] Liu, B. & Bazan, G. C. Interpolyelectrolyte complexes of conjugated copolymers and dna: platforms for multicolor biosensors. *Journal of the American Chemical Society* **126**, 1942–1943 (2004).

[20] Liu, B., Gaylord, B. S., Wang, S. & Bazan, G. C. Effect of chromophore-charge distance on the energy transfer properties of water-soluble conjugated oligomers. *Journal of the American Chemical Society* **125**, 6705–6714 (2003).

[21] Miyaura, N., Yanagi, T. & Suzuki, A. The palladium-catalyzed cross-coupling reaction of phenylboronic acid with haloarenes in the presence of bases. *Synthetic Communications* **11**, 513–519 (1981).

[22] Kuehne, A. J., Gather, M. C. & Sprakel, J. Monodisperse conjugated polymer particles by suzuki–miyaura dispersion polymerization. *Nature communications* **3**, 1088 (2012).

[23] Metzler, L. *et al.* High molecular weight mechanochromic spiropyran main chain copolymers via reproducible microwave-assisted suzuki polycondensation. *Polym. Chem.* **6**, 3694–3707 (2015).

[24] Komber, H. *et al.* Soluble and stable alternating main-chain merocyanine copolymers through quantitative spiropyran–merocyanine conversion. *Polymer Chemistry* **5**, 443–453 (2014).

[25] van de Laar, T. *et al.* Light from within: Sensing weak strains and femtonewton

forces in single molecules. *Chem* **4**, 269–284 (2018).

[26] Scheer, P. v. d., Laar, T. v. d. & Sprakel, J. Chain length-dependent luminescence in acceptor-doped conjugated polymers. *Scientific Reports* **9**, 11217 (2019).

[27] Van Der Scheer, P., Van De Laar, T., Van Der Gucht, J., Vlassopoulos, D. & Sprakel, J. Fragility and strength in nanoparticle glasses. *ACS nano* **11**, 6755–6763 (2017).

[28] Minkin, V. I. Photo-, thermo-, solvato-, and electrochromic spiroheterocyclic compounds. *Chemical reviews* **104**, 2751–2776 (2004).

[29] Garcia, A. *et al.* Photo-, thermally, and ph-responsive microgels. *Langmuir* **23**, 224–229 (2007).

[30] Görner, H., Atabekyan, L. S. & Chibisov, A. K. Photoprocesses in spiropyran-derived merocyanines: singlet versus triplet pathway. *Chemical physics letters* **260**, 59–64 (1996).

[31] Krysanov, S. & Alfimov, M. Ultrafast formation of transients in spiropyran photochromism. *Chemical Physics Letters* **91**, 77–80 (1982).

[32] Vandewyer, P., Hoefnagels, J. & Smets, G. Photochromic spiropyrans. *Tetrahedron* **25**, 3251–3266 (1969).

[33] Klaerner, G. & Miller, R. D. Polyfluorene derivatives: Effective conjugation lengths from well-defined oligomers. *Macromolecules* **31**, 2007–2009 (1998).

[34] Goldburt, E., Shvartsman, F., Fishman, S. & Krongauz, V. Intramolecular interactions in photochromic spiropyran-merocyanine polymers. *Macromolecules* **17**, 1225–1230 (1984).

[35] Piskorz, K., Dust, J. M., Buncel, E., Lebel, O. & Nunzi, J.-M. Deceleration of thermal ring closure in a glass-forming mexylaminotriazine-substituted merocyanine (mc) linked to intramolecular hydrogen bonding. *New J. Chem.* **41**, 940–947 (2017).

[36] Richert, R. & Bässler, H. Merocyanine spiropyran transformation in a polymer matrix: an example of a dispersive chemical reaction. *Chemical physics letters* **116**, 302–306 (1985).

[37] Bertoldo, M., Nazzi, S., Zampano, G. & Ciardelli, F. Synthesis and photochromic response of a new precisely functionalized chitosan with “clicked” spiropyran. *Carbohydrate Polymers* **85**, 401 – 407 (2011).

[38] Wojtyk, J. T., Wasey, A., Kazmaier, P. M., Hoz, S. & Buncel, E. Thermal reversion mechanism of n-functionalized merocyanines to spiropyrans: a solvatochromic, solvatokinetic, and semiempirical study. *The Journal of Physical Chemistry A* **104**, 9046–9055 (2000).

[39] Goldburt, E., Shvartsman, F. & Krongauz, V. " zipper" crystallization of polymers with spiropyran side groups. *Macromolecules* **17**, 1876–1878 (1984).

[40] Mhuircheartaigh, E., Blau, W. J., Prato, M. & Giordani, S. Spectroscopic changes induced by sonication of porphyrin–carbon nanotube composites in chlorinated

solvents. *Carbon* **45**, 2665 – 2671 (2007).

[41] Göstl, R. & Sijbesma, R. π-extended anthracenes as sensitive probes for mechanical stress. *Chemical science* 7, 370–375 (2016).

[42] Li, H. *et al.* Promoting mechanochemistry of covalent bonds by noncovalent micellar aggregation. *ACS Macro Letters* **5**, 995–998 (2016).

[43] Gacal, B. *et al.* Anthracene- maleimide-based diels- alder "click chemistry" as a novel route to graft copolymers. *Macromolecules* **39**, 5330–5336 (2006).

[44] Haidekker, M. A., Brady, T. P., Lichlyter, D. & Theodorakis, E. A. A ratiometric fluorescent viscosity sensor. *Journal of the American Chemical Society* **128**, 398–399 (2006).

[45] Haidekker, M. A. & Theodorakis, E. A. Molecular rotors—fluorescent biosensors for viscosity and flow. *Organic & Biomolecular Chemistry* **5**, 1669–1678 (2007).

[46] Levitt, J. A. *et al.* Fluorescence anisotropy of molecular rotors. *ChemPhysChem* **12**, 662–672 (2011).

[47] Grell, M. *et al.* Chain geometry, solution aggregation and enhanced dichroism in the liquidcrystalline conjugated polymer poly(9,9-dioctylfluorene). *Acta Polymerica* **49**, 439–444 (1998).

Chapter 3

Rigidochromic conjugated polymers carrying main-chain molecular rotors

We design and prepare rigidochromic conjugated polymers that carry molecular rotors in the main chain. We show how a suitable design maintains the mechanosensitivity of the rotors upon incorporation into an extended π-conjugated system. Construction of donor-acceptor polymers enables their use as ratiometric probes for polymer micromechanics, which we evidence through micromechanical imaging of a phase-separated polymer blend.

This chapter was published as:
P. van der Scheer, Q. van Zuijlen and J. Sprakel: *Rigidochromic conjugated polymers carrying main-chain molecular rotors,* Chem. Commun., 2019,55, 11559-11562.

3.1 Introduction

The properties of many soft and biological materials depends sensitively on the emergence of complex mechanical patterns at the microscale. Micromechanical imaging, e.g. using contact-based techniques such as Atomic Force Microscopy, can resolve these patterns at the surface, but preclude insights deep into bulk materials. Molecular mechanosensors have emerged as valuable probes to enable non-invasive micromechanical imaging using optical methods, in order to resolve mechanical patterns deep inside materials. One particular class of these mechano-sensitive probes are molecular rotors. Molecular rotors derive their mechano-optical coupling on the basis of a Twisted Intramolecular Charge Transfer (TICT) principle.[1, 2, 3, 4] Upon photoexcitation, the molecular rotor tends to undergo an intramolecular rotation, which alters its electronic configuration and opens a pathway for non-radiative decay of the excited state. The accessibility of this pathway depends on the rate at which the intramolecular rotation can occur, which is sensitive to the solvent viscosity or polymer free volume. In this way, molecular rotors exhibit a coupling between the fluidity of the surroundings and their fluorescence quantum efficiency and lifetime. The rigidochromism of these probes has been harnessed for the study of a wide variety of micromechanical phenomena both in synthetic materials and in biology, including studies of plasma membrane fluidity [5, 6], polymer free volume [7, 8] and contact mechanics[9].

More recently, the mechano-optical coupling found in semiconducting polymers has emerged as a powerful platform for micromechanical analysis [10, 2, 3]. Here, the mechanosensitivity derives from a coupling between the conformation of the entropic backbone in response to mechanical stress and the intramacromolecular energy transfer efficiency. To date, the potential of small-molecule mechano-sensitive probes in combination with semiconducting polymers has not yet been harnessed. Coupling the rigidochromism of molecular rotors to the mechanosensitivity of

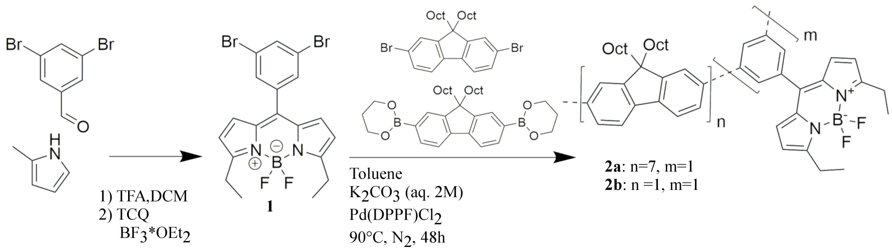

Figure 3.1: Schematic illustration of the synthesis pathway to prepare reactive molecular rotors and their co-polymerization into rigidochromic polymers.

semiconducting polymers could lead to a new class of mechanochromic materials. For example, using molecular rotors in a donor-acceptor semiconducting polymer could result in ratiometric fluidity probes for quantitative micromechanical imaging, or in semiconducting materials that actively respond to external mechanical stimuli.

In this Communication, we design and prepare mechanosensitive conjugated polymers that carry rigidochromic molecular rotors in the main chain. The fluidity-dependent rotation of the rotors to a state of twisted intramolecular charge transfer (TICT) is maintained when incorporated into the extended conjugated structure of a poly(fluorene) backbone. This results in luminescent polymers with a donor-acceptor structure, whose intramolecular transfer efficiency depends on the mechanics of the local environment. We confirm that the emission ratio is linear in the excited state lifetime of the rotor, enabling their use as quantitative ratiometric fluidity sensors. We demonstrate their potential by performing ratiometric micromechanical imaging on a demixed polymer blend. These rigidochromic organic semiconductors can enable non-invasive mechanical imaging in polymeric or biological materials, or can serve as a building blocks for mechanochromic optoelectronic devices.

As our rigidochromic building block we choose phenyl-substituted boron-dipyrromethene (BODIPY) molecular rotors (Fig .3.1, structure **1**). The BODIPY rotor is a good choice for incorporation into a conjugated chain, as it has been shown to be stable under Suzuki-Miyaura reaction conditions [13, 14]. Building the molecular rotor into the main-chain of a semiconducting polymer, offers two options; polymerization along the rotor (BODIPY) core or along the pendant phenyl substituent. Extension of the π-conjugated system of the BODIPY core alters the electronic configuration of the molecule to such an extent that rigidochromism is lost [15]. We therefore opt to use the phenyl ring as our attachment point, which is known to leave rotor function intact[16]. Moreover, steric considerations are also relevant, as substituents on the phenyl ring may hinder rotation [17]. We therefore chose a *meta*-substitution pattern of two aromatic halogens on the 3-5 position of the phenyl ring such that hindrance of the rotation is minimized (Fig.3.1, structure **1**).

It is our aim to design a semiconducting polymer whose emission pattern changes depending on the local mechanics of its surroundings. To achieve this, we incorporate the dibromo-Ph-BODIPY in a poly(dioctyl fluorene) polymer as a main-chain dopant. This leads to a polymer with a internal donor-acceptor structure. The polyfluorene emission overlaps with the excitation band of the BODIPY dopants, leading to intramolecular energy transfer (ET). The nature of this transfer is most likely a combination of transfer along the conjugated chain by excitonic migration and transfer through the dielectric medium by dipolar coupling [18]. The blue emission of the polyfluorene backbone serves both as an internal reference, for comparison to the rotor emission, and as the excitation source for the the rotor due to ET.

First, we synthesize dibromo-Ph-BODIPY by condensation of dibromobenzaldehyde with 2-ethyl pyrrole, based on the method of Wagner and Lindsey[19]; ^{1}HNMR and MS (see ESI) show the product to be pure with 18% yield, in accord with literature [19, 15, 20]. We subsequently, prepare two rigidochromic copolymers via Suzuki-Miyaura polycondensation [1, 2, 3] with two different doping ratios of dioctyl fluorene and our molecular rotor (Fig .3.1, structure **2a**-**b**). This resulted in polymers with

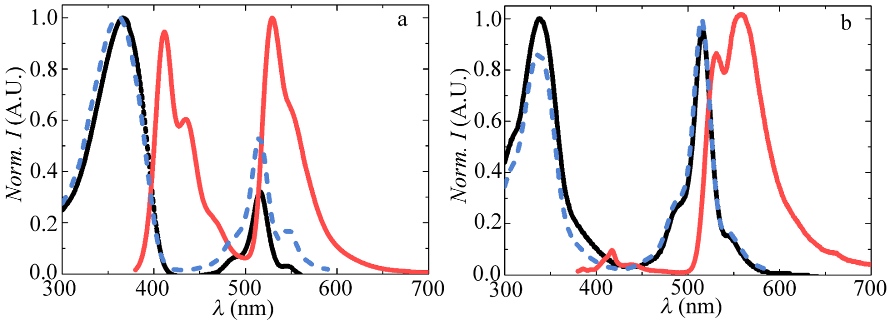

Figure 3.2: Absorption (solid black line), excitation (blue dashed line) and fluorescence (solid red line, $\lambda_{ex} = 370nm$) spectra of a) **2a** and b) **2b**

.

$M_w = 6.1$ kg/mol for **2a** and 5.5 kg/mol for **2b**, after correction of the GPC data for the chain stiffness [22].

The chemical composition of polymer **2b** is bound to a strict 1:1 ratio of fluorene:rotor, due to the Suzuki coupling chemistry. By contrast, in polymer **2a**, this is not the case. Analysis by ^{1}HNMR shows that the resulting rotor doping degree is closer to 10:1 (fluorene:rotor) than the aimed at 7:1, which may be due to the different reactivity of the two dibrominated monomers in this reaction mixture.

The absorption, excitation and emission spectra of these two polymers take the shape of linear combinations of the spectra for pure poly(dioctyl fluorene) and a small molecule Ph-BODIPY rotor (Fig. 3.2a-b). This indicates that the combination of both species within a single extended π-conjugated structure does not alter their optical properties. The emission spectra, upon donor excitation at $\lambda = 372$ nm, show strong differences between the two copolymers. The alternating poly(fluorene-alt-Ph-BODIPY) **2b** gives almost complete intramolecular energy transfer from fluorene donors to rotor moieties as the acceptor even in low viscous solutions (Fig. 3.2b). We also note that the acceptor emission band of **2b** exhibits a shoulder at higher wavelength, which could be indicative of intermolecular aggregation of the rotors in the highly doped polymer coil. This is confirmed by the fact that the emission intensity of this shoulder is insensitive to the viscosity of the surrounding solution (see SI). Moreover, also the absorption spectrum of the rotor in this design exhibits a shoulder that is characteristic of aggregation possibly due to pi-pi interactions within the polymer coil where the local concentration of rotors is very high. Combined with the fact that the emission ratio of donor to acceptor in low viscous media is very low, limiting the dynamic range of sensing, makes this design poorly suited for ratiometric mechanosensing applications.

By contrast, the minority-doped polymer **2a** shows emission bands for both the donor and acceptor (Fig. 3.2a), indicative of incomplete energy transfer. This makes this design potentially suitable as a ratiometric mechanosensor.

We note that the donor backbone exhibits a stress- and conjugation length dependence of the maximum emission wavelength and its vibronic structure.[23, 2] Both the position and shape of the donor emission band indicate a backbone above the conjugation length and a relaxed, non-collapsed, conformation.

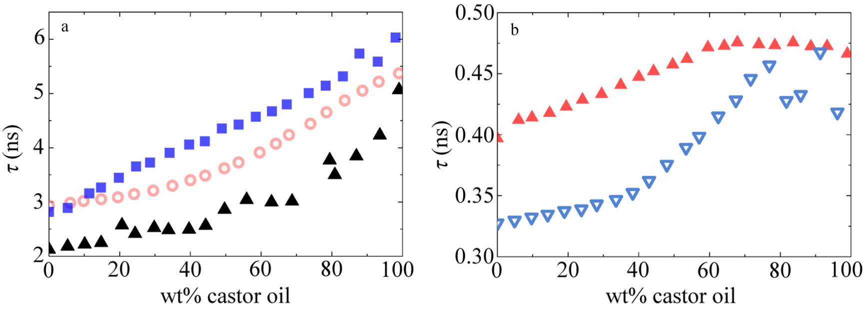

Figure 3.3: a) Average fluorescence lifetimes of the molecular rotor as a function of wt% castor oil, for small molecule rotor **1** (triangles), and rotor in copolymers **2a** (circles) and **2b** (squares). Data was recorded by excitation at λ_{ex}:372 nm and emission at λ_{em}540nm. b) Fluorene donor lifetimes as a function of wt% castor oil for **2a** (filled triangles) and the reference homopolymer (open triangles), recorded at $\lambda_{ex} = 372$ nm and $\lambda_{em} = 420$ nm.

To confirm that rigidochromic behavior is maintained, we perform fluorescence lifetime measurements of polymers dissolved in solvents of varying viscosity (Fig 3.3a-b), prepared from mixtures of low viscosity toluene and high viscosity castor oil. As a reference, we include a non-brominated version of rotor **1**, which is not part of an extended conjugated system. We observe how the excited state lifetime of the rotor, both as a small molecule and as a dopant in the semiconducting chains, grows with increasing the viscosity, upon going from pure toluene to 95 wt% castor oil (Fig 3.3a). This confirms that the rigidochromism is maintained. We note a slight reduction in the sensitivity of the lifetime versus viscosity response of the co-polymerised rotors as compared to their small molecule equivalents, in particular at low viscosities (i.e. low fractions of castor oil) (Fig 3.3a). In all cases, rotor lifetime increases by more than a factor of 2 over the explored viscosity range, making this design suitable for sensitive mechanosensory experiments. Finally we note that the shape of the time-resolved fluorescence decays is monoexponential for the small molecule rotor and the rotor copolymerized as a minority component in design **2a**; by contrast, in the highly doped polymer **2b**, where

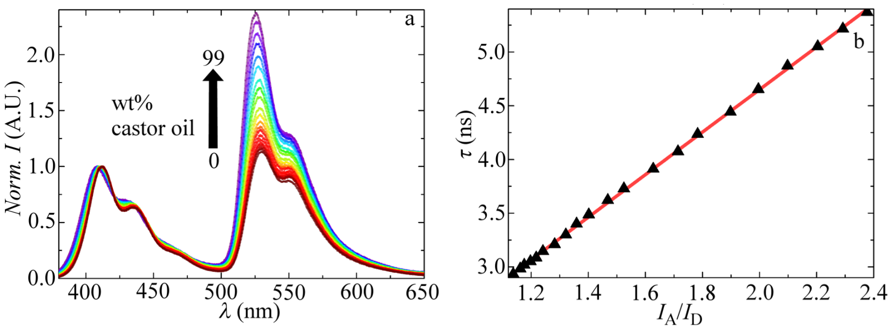

Figure 3.4: a) Fluorescence spectra of **2a** normalized to their donor emissions maximum for identical samples as in fig 3b. Inset the λ_{max} of the donor (red triangles) and guide for the eye (solid line) as a function of wt% castor oil b) Fluorescence lifetimes as a function of acceptor/donor ratio of **2a** (black triangles) and a linear fit (red solid line)

we find signs of aggregation, we also observe a biexponential decay, of which only one component is sensitive to viscosity, further substantiating the hypothesis of intermolecular aggregation when the rotor doping degree is too high.

Interestingly, we also see that the donor polymer itself is rigidochromic to some extent. The donor lifetime, of both the copolymer and of pure poly(dioctylfluorene) homopolymer, grows mildly with increasing solvent viscosity (Fig 3.3b). This could be explained by the effect the increased viscosity had on the relaxation rate of torsion angles along the backbone.[24]. The difference in the donor response to viscosity between a copolymer and homopolymer is most likely due to differences in chain flexibility and length.

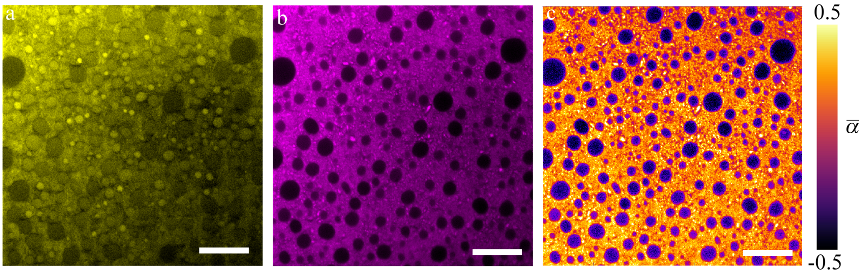

Figure 3.5: Micromechanical imaging of a phase separated polymer film, showing liquid poly(butyl acrylate) droplets in a solid poly(hexadecyl acrylate) matrix, containing sensor **2a**, showing donor (a) and acceptor channels (b) and the corresponding ratiometric fluidity map in based on the normalised ratio $\alpha/\langle\alpha\rangle - 1$ (c). Scale bars = 40 micrometer.

Molecular rotors have emerged as valuable molecular mechanosensors for micromechanical imaging of complex materials[5, 25, 26]. This is usually done through fluorescence lifetime imaging (FLIM) to obtain a quantitative response. However, FLIM instruments are costly and suffer from a poor temporal resolution, often requiring minutes for acquisition of a single image. Ratiometric rigidochromic probes could solve these issues, by enabling imaging on simple confocal microscopes and enabling data aqcuisition rate set only by the instrument, often orders-of-magnitude faster than in FLIM.

A good ratiometric rotor dye must have a linear correlation between the fluorescence lifetime, which correlates to solvent viscosity, and the emission ratio.

To confirm if our probe obeys this constraint, we take polymer **2a** and measure the fluorescence emission spectra for the same samples used in the fluorescence lifetime experiments. Normalized emission spectra indeed show the growth of the acceptor, i.e. rotor, band with respect to that of the donor with increasing viscosity (Fig.3.4a). A plot of the fluorescence lifetime as a function of the emission ratio of acceptor to donor I_A/I_D reveals a perfect linear correlation (Fig.3.4b). This proves that our sensor design **2a** is suitable as a quantitative ratiometric rigidochromic probe. We note that the sensitivity of the donor lifetime of **2a** to viscosity (Fig.3.3b) does not seem to influence this relation.

To showcase the application of such a rigidochromic sensor with a ratiometric read-out, we perform micromechanical imaging experiments on a phase separated polymer blend. We add polymer **2a** as a probe to a mixture of poly(hexadecyl acrylate)(pHDA) and poly butyl acrylate (pBA) at 0.5 wt% to polymer. Spincoated layers of this blend result in phase separated films upon solvent evaporation. From confocal microscopy images of the donor signal (Fig.3.5a) we find that the probe is present in both pHDA and pBA phases, with a slight partioning preference for the solid pHDA phase. Major differences appear in the acceptor channel, where the mechanically-sensitive rotor dye manifests (Fig.3.5b), with a high rotor signal in the solid pHDA matrix and a low rotor signal in the fluid pBA droplets.

To convert these data to a ratiometric image that reflects the local micromechanics, we compute the normalized emission ratio as $\bar{\alpha} = \left(\frac{\alpha}{\langle\alpha\rangle} - 1\right)$

where $\alpha = I_D/I_A$ is the raw emission intensity and $\langle\alpha\rangle$ its ensemble average. This results in a clear micromechanical image of the complex polymer material (Fig.3.5c). The liquid pBA droplets appear homogeneous, expected for a fast-relaxing polymer melt. By contrast, the pHDA matrix exhibits spatial variations in $\bar{\alpha}$. These are most likely caused by the grain boundaries of the waxy alifatic crystal where the rotor has increased free volume to undergo the internal rotation.

To confirm that the ratiometric image is not biased by partioning effects between the two chemically-distinct polymer phases, we perform a correlation analysis. We see that there is no correlation of $\bar{\alpha}$ with respect to the donor intensity (Fig.3.18a), confirming the absence of such a bias. Yet, there is a positive correlation between $\bar{\alpha}$ and acceptor intensity (Fig.3.18b), highlighting that ratiometric difference emerge only because of the rigidochromism of the acceptor. Finally, from such images, quantitative information can be extracted. We do so by plotting the probability distribution of ratiometric values $\bar{\alpha}$, which reveals two distinct populations (Fig.3.18c), that can be attributed to the fluid pBA domains ($\bar{\alpha} < 0$) and solid pHDA domains ($\bar{\alpha} > 0$).

We have demonstrated the successful incorporation of a rigidochromic molecule into the main-chain of a conjugated polymer while retaining its mechano-sensitive properties. A linear correlation between fluorescence lifetime and emission ratios confirms its suitability as a linear ratiometric fluidity probe, which is further evidenced by micromechanical imaging using confocal microscopy. The coupling between local mechanics and emission properties could be harnessed for quantitative micromechanical imaging, based on a simple ratiometric principle, in a variety of polymeric materials or biological compartments such as vesicles, without the necessity for fluorescence lifetime imaging instrumentation, which is often used for rigidochromic probes without an internal emission standard [27, 28, 29]. Moreover, such mechanochromic semiconducting polymers could find application in optoelectronic applications where mechanical feedback, e.g., for haptic displays, is required [30, 31, 32, 33].

References

[1] Kuimova, M. K. Molecular rotors image intracellular viscosity. *CHIMIA International Journal for Chemistry* **66**, 159–165 (2012).

[2] Hu, R. *et al.* Twisted intramolecular charge transfer and aggregation-induced emission of bodipy derivatives. *The Journal of Physical Chemistry C* **113**, 15845–15853 (2009).

[3] Sasaki, S., Drummen, G. P. & Konishi, G.-i. Recent advances in twisted intramolecular charge transfer (tict) fluorescence and related phenomena in materials chemistry. *Journal of Materials Chemistry C* **4**, 2731–2743 (2016).

[4] Haidekker, M. A. & Theodorakis, E. A. Environment-sensitive behavior of fluorescent molecular rotors. *Journal of Biological Engineering* **4**, 11 (2010).

[5] López-Duarte, I., Vu, T. T., Izquierdo, M. A., Bull, J. A. & Kuimova, M. K. A molecular rotor for measuring viscosity in plasma membranes of live cells. *Chemical Communications* **50**, 5282–5284 (2014).

[6] Dent, M. R. *et al.* Imaging phase separation in model lipid membranes through the use of bodipy based molecular rotors. *Physical Chemistry Chemical Physics* **17**, 18393–18402 (2015).

[7] Loutfy, R. O. Fluorescence probes for polymer free-volume. *Pure and Applied Chemistry* **58**, 1239–1248 (1986).

[8] Doolittle, A. K. Studies in newtonian flow. iii. the dependence of the viscosity of liquids on molecular weight and free space (in homologous series). *Journal of Applied Physics* **23**, 236–239 (1952).

[9] Suhina, T. *et al.* Fluorescence microscopy visualization of contacts between objects. *Angewandte Chemie* **127**, 3759–3762 (2015).

[10] van de Laar, T. *et al.* Light from within: Sensing weak strains and femtonewton forces in single molecules. *Chem* **4**, 269–284 (2018).

[11] Cingil, H. E. *et al.* Illuminating the reaction pathways of viromimetic assembly. *Journal of the American Chemical Society* **139**, 4962–4968 (2017).

[12] Cingil, H. E. *et al.* Monitoring protein capsid assembly with a conjugated polymer strain sensor. *Journal of the American Chemical Society* **137**, 9800–9803 (2015).

[13] Zhou, Z., Zhou, J., Gai, L., Yuan, A. & Shen, Z. Naphtho [b]-fused bodipys: one pot suzuki–miyaura–knoevenagel synthesis and photophysical properties. *Chemical Communications* **53**, 6621–6624 (2017).

[14] Hayashi, Y., Yamaguchi, S., Cha, W. Y., Kim, D. & Shinokubo, H. Synthesis of directly

connected bodipy oligomers through suzuki–miyaura coupling. *Organic Letters* **13**, 2992–2995 (2011).

[15] Alemdaroglu, F. E. *et al.* Poly (bodipy) s: A new class of tunable polymeric dyes. *Macromolecules* **42**, 6529–6536 (2009).

[16] Xochitiotzi-Flores, E. *et al.* Optical properties of two fluorene derived bodipy molecular rotors as fluorescent ratiometric viscosity probes. *New Journal of Chemistry* **40**, 4500–4512 (2016).

[17] Vu, T. T., Méallet-Renault, R., Clavier, G., Trofimov, B. A. & Kuimova, M. K. Tuning bodipy molecular rotors into the red: sensitivity to viscosity vs. temperature. *Journal of Materials Chemistry C* **4**, 2828–2833 (2016).

[18] van der Scheer, P., van de Laar, T. & Sprakel, J. chain length-dependent luminescence in acceptor-doped conjugated polymers. *Scientific Reports* **9** (2019).

[19] Wagner, R. W. & Lindsey, J. S. Boron-dipyrromethene dyes for incorporation in synthetic multi-pigment light-harvesting arrays. *Pure and Applied Chemistry* **68**, 1373–1380 (1996).

[20] Meng, G., Velayudham, S., Smith, A., Luck, R. & Liu, H. Color tuning of polyfluorene emission with bodipy monomers. *Macromolecules* **42**, 1995–2001 (2009).

[21] Miyaura, N., Yanagi, T. & Suzuki, A. The palladium-catalyzed cross-coupling reaction of phenylboronic acid with haloarenes in the presence of bases. *Synthetic Communications* **11**, 513–519 (1981).

[22] Grell, M. *et al.* Chain geometry, solution aggregation and enhanced dichroism in the liquidcrystalline conjugated polymer poly (9, 9-dioctylfluorene). *Acta Polymerica* **49**, 439–444 (1998).

[23] Klaerner, G. & Miller, R. Polyfluorene derivatives: effective conjugation lengths from well-defined oligomers. *Macromolecules* **31**, 2007–2009 (1998).

[24] Monkman, A., Rothe, C., King, S. & Dias, F. Polyfluorene photophysics. In *Polyfluorenes*, 187–225 (Springer, 2008).

[25] Kuimova, M. K., Yahioglu, G., Levitt, J. A. & Suhling, K. Molecular rotor measures viscosity of live cells via fluorescence lifetime imaging. *Journal of the American Chemical Society* **130**, 6672–6673 (2008).

[26] Loison, P. *et al.* Direct investigation of viscosity of an atypical inner membrane of bacillus spores: a molecular rotor/flim study. *Biochimica et Biophysica Acta (BBA)-Biomembranes* **1828**, 2436–2443 (2013).

[27] Peinado, C., Salvador, E., Catalina, F. & Lozano, A. Solvatochromic and rigidochromic fluorescent probes based on d–π-a diaryl ethylene and butadiene derivatives for uv-curing monitoring. *Polymer* **42**, 2815–2825 (2001).

[28] Haidekker, M. A. & Theodorakis, E. A. Molecular rotors—fluorescent biosensors for viscosity and flow. *Organic & Biomolecular Chemistry* **5**, 1669–1678 (2007).

[29] Raut, S. *et al.* A homodimeric bodipy rotor as a fluorescent viscosity sensor for membrane-mimicking and cellular environments. *Physical Chemistry Chemical Physics* **16**, 27037–27042 (2014).

[30] Ciardelli, F., Ruggeri, G. & Pucci, A. Dye-containing polymers: methods for preparation of mechanochromic materials. *Chemical Society Reviews* **42**, 857–870 (2013).

[31] Peterson, G. I., Larsen, M. B., Ganter, M. A., Storti, D. W. & Boydston, A. J. 3d-printed mechanochromic materials. *ACS Applied Materials & Interfaces* 7, 577–583 (2014).

[32] Pucci, A. & Ruggeri, G. Mechanochromic polymer blends. *Journal of Materials Chemistry* **21**, 8282–8291 (2011).

[33] Metzler, L. *et al.* High molecular weight mechanochromic spiropyran main chain copolymers via reproducible microwave-assisted suzuki polycondensation. *Polymer Chemistry* **6**, 3694–3707 (2015).

3.2 Appendix

3.3 Methods

Chemicals

All chemicals and solvents were bought from Sigma Aldrich (Merck) Europe, TCI Europe and BIOSOLVE and used as received unless otherwise mentioned. Poly(9,9-di-n-octylfluorenyl-2,7-diyl) from Sigma Alrich was used as a spectroscopy reference. Product number: 571652. Mw $\geq$ 20kg/Mol.

8-[3,5-dibromophenyl]-3,5-diethyl-4,4-difluoro-4-bora-3a, 4a-diaza-s- indacene (1)

To 50 ml anhydrous and deoxygenated DCM was added 2.64 g (10 mmol) 3,5-dibromobenzaldehyde which was further deoxygenated. To this we added 2.04 ml (1.9 g, 20 mmol) 2-ethyl-1H-pyrrole and 100μl TFA. The reaction is performed for 18 hours under nitrogen atmosphere and light poor conditions at room temperature. To this was added 2.46 g (10 mmol) tetrachloro-1,4-benzoqui- ‘none (TCQ) in 30 ml anhydrous DCM, and then stirred for 50 minutes at room temperature. To this 10 ml DiPEA was added followed by stirring for 30 minutes. To this 10 ml BF_3*$O(Et)_2$ was added and stirred for 45 minutes. Solvents were removed under vacuum and the remaining suspension was filtered and washed with DCM. The filtrate was purified by silica column chromatography using DCM as eluent yielding 887 mg (18.3 % mol/mol) product. MS: M+H/z, relative abundance: 481.2, 50; 483.2, 100; 485.2, 50; 1H-NMR (400 MHz, $CDCl_3$, 300 K): δ (ppm) 7.84 (t, 1H, J=1.8 Hz), 7.59 (d, 2H, J=1.8 Hz), 6.71 (d, 2H, J=4.1 Hz), 6.39 (d, 2H, J=4.2 Hz), 3.08 (q, 4H, J=7.6 Hz), 1.35 (t, 6H, J=7.6 Hz)

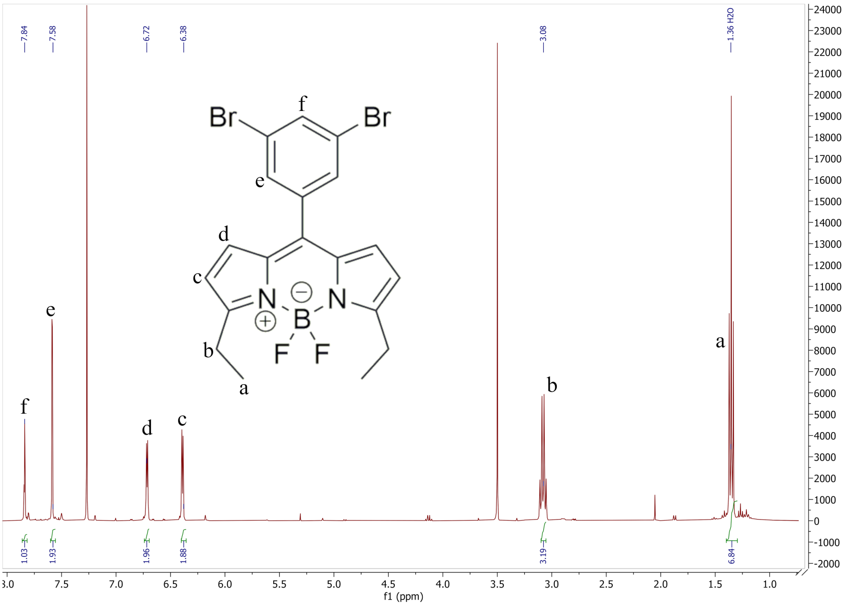

Figure 3.6: ^{1}HNMR specrum of **1** in $CDCl_3$

8-phenyl-3,5-diethyl-4,4-difluoro-4-bora-3a,4a-diaza-s-indacene

As a spectroscopy reference a non-brominated bodipy-rotor was prepared. The same protocol was used as for **1** but with benzaldehyde.

poly-(9,9-dioctylfluorene-2,7-diyl)-co-(5-[3,5-diethyl-4,4-difluoro-4-bora-3a,4a-diaza-s-indacene-8-yl]-m-phenylene (2a)

Conjugated polymers composed primarily of donor moieties, and doped with a minority fraction of acceptors, are prepared via standard Suzuki-Miyaura polycondensation reactions [1, 2, 3]. We dissolve 100 mg (0.2075 mmol) **1**, 341.38 mg (0.6225 mmol) 2,7-dibromo-9,9-dioctyl-fluorene and 463.44 mg (0.8300 mmol) 9,9-dioctylfluorene-2,7-diboronic acid bis(1,3-propanediol) ester in 2 ml toluene, 15 ml 2M K_2CO_3 under nitrogen atmosphere. After thorough deoxygenation, we add 25 mg [1,1-Bis(diphenylphosphino)ferrocene]dichloropalladium(II) (Pd(DPPF)Cl_2). The reaction

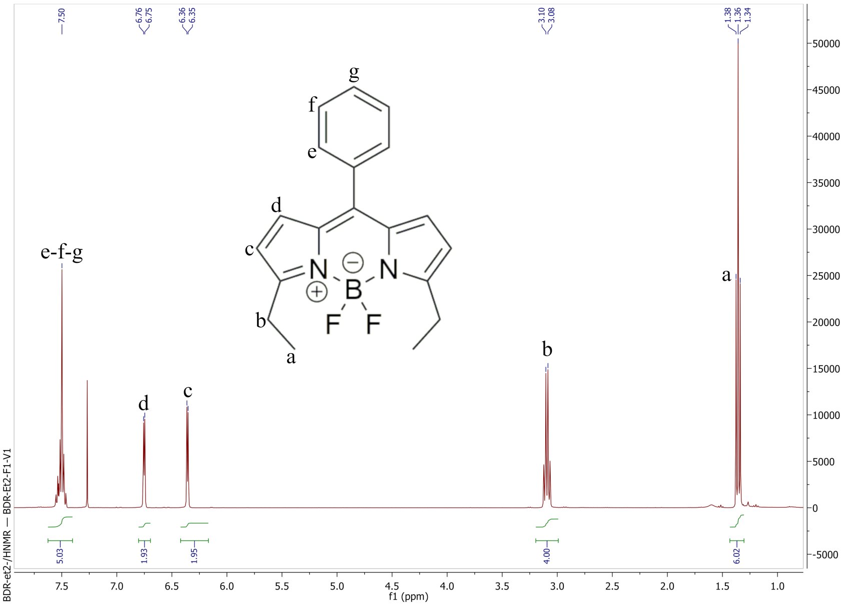

Figure 3.7: ^{1}HNMR specrum of **8-phenyl-3,5-diethyl-4,4-difluoro-4-bora-3a,4a-diaza-s-indacene** in $CDCl_3$

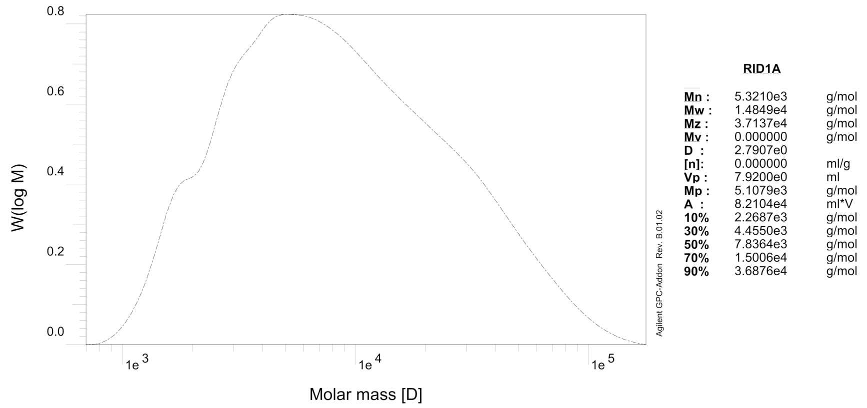

RID1A

Mn :	5.3210e3	g/mol
Mw :	1.4849e4	g/mol
Mz :	3.7137e4	g/mol
Mv :	0.000000	g/mol
D :	2.7907e0	
[n]:	0.000000	ml/g
Vp :	7.9200e0	ml
Mp :	5.1079e3	g/mol
A :	8.2104e4	ml*V
10%	2.2687e3	g/mol
30%	4.4550e3	g/mol
50%	7.8364e3	g/mol
70%	1.5006e4	g/mol
90%	3.6876e4	g/mol

Figure 3.8: GPC trace and calculated mass against polystyrene reference standards for **2a** measured in $CHCl_3$ at 35°C.

is performed for 48 hours at 90°C. The crude product is obtained by precipitation in cold methanol and Soxhlet extraction against ethanol and acetone. Yield: 44.8 mg (7.1%). GPC: Mn: 2.0 kDa, Mw: 5.5 kDa, D: 2.7907; 1H-NMR (400 MHz, $CDCl_3$, 300 K): δ (ppm) 7.86, (s, 2H), 7.84 (s, 23H), 7.75-7.61 (m, 62H), 3.09 (q (dq?), 4H, J=6.1 Hz), 2.12 (s br, 53H), 1.26-1.14 (m, 341H), 1.35 (t), 6H, J=6.1 Hz), 0.82 (m, 172H)

poly-(9,9-dioctylfluorene-2,7-diyl)-alt-(5-[3,5-diethyl-4,4-difluoro-4-bora-3a,4a-diaza-s-indacene-8-yl]-m-phenylene (2b)

Using the same protocol we **2b** using the following amounts: 200 mg (0.4150 mmol) **1** and 231.72 mg (0.4150 mmol) 9,9-dioctylfluorene-2,7-diboronic acid bis(1,3-propanediol) ester & 12.5 mg $Pd(DPPF)Cl_2$. Yield: 69.5 mg (23.5%). GPC: Mn: 3.0, Mw: 6.1 kDa, D: 1.9964; 1H-NMR (400 MHz, $CDCl_3$, 300 K): δ (ppm) 8.10-7.5 (13H, m), 6.95 (2H, s), 6.43(2H, s), 3.13 (4H, m), 2.10(5H, s), 1.37-0.6(75H,m)

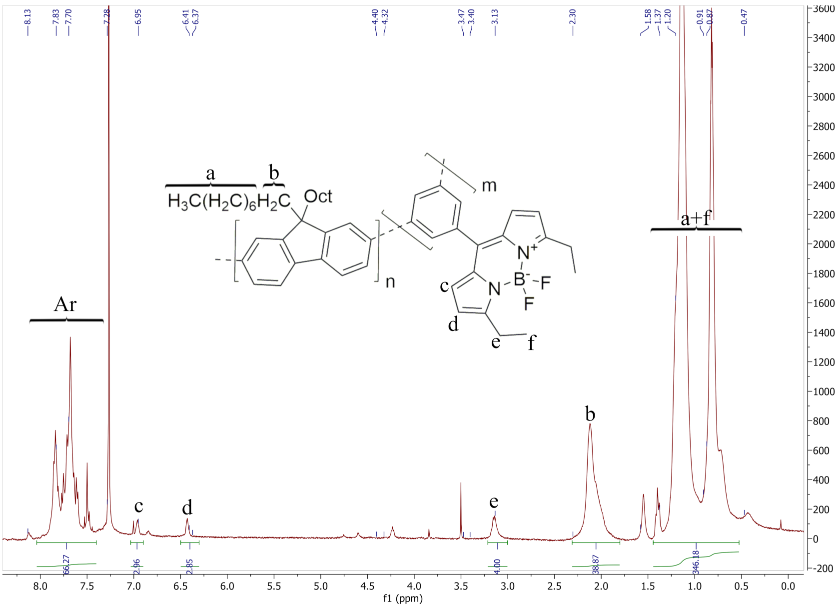

Figure 3.9: ^{1}HNMR specrum of **2a** in $CDCl_3$

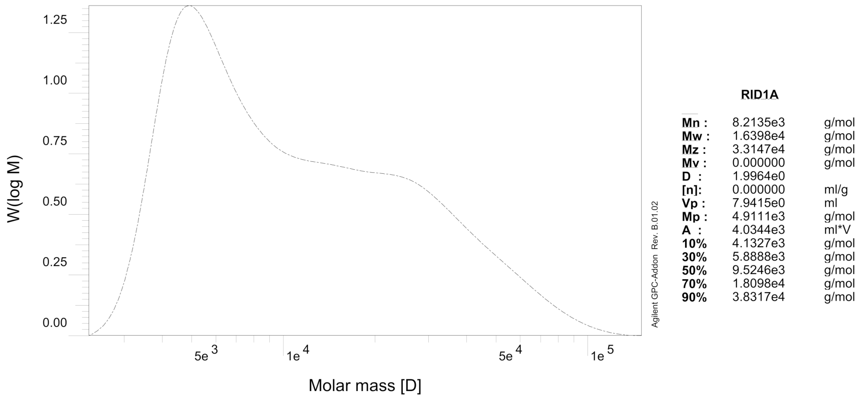

```
RID1A

Mn :   8.2135e3   g/mol
Mw :   1.6398e4   g/mol
Mz :   3.3147e4   g/mol
Mv :   0.000000   g/mol
D  :   1.9964e0
[n]:   0.000000   ml/g
Vp :   7.9415e0   ml
Mp :   4.9111e3   g/mol
A  :   4.0344e3   ml*V
10%    4.1327e3   g/mol
30%    5.8888e3   g/mol
50%    9.5246e3   g/mol
70%    1.8098e4   g/mol
90%    3.8317e4   g/mol
```

Figure 3.10: GPC trace and calculated mass against polystyrene reference standards for **2b** measured in $CHCl_3$ at 35°C.

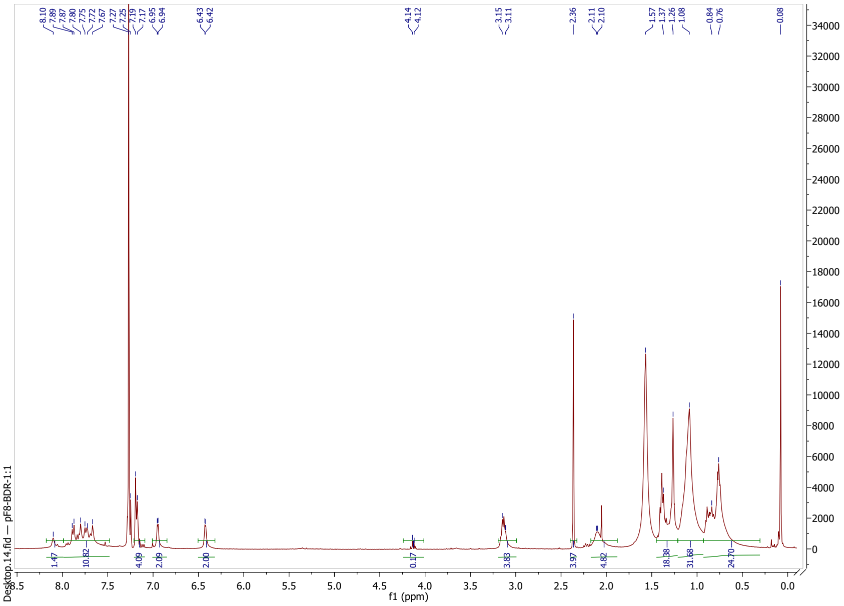

Figure 3.11: ^{1}HNMR specrum of **2b** in $CDCl_3$

Synthesis of poly(hexadecyl acrylate

In 40 ml Toluene 12.5g (42.2mmmol) octadecyl acrylate and 18mg 2,2'-dimethyl-2,2'-azodipropiononitril (AIBN) were dissolved. In a roundbottom flask fitted with reflux condensor 10ml of Toluene was stirred and heated to 140°C for 5 minutes. The octadecyl acrylate solution was added via a dropping funnel over the course of 1 hour and this was reacted at 140°C for 24 hours. The product was cleaned by precipitating in cold methanol three times.

Synthesis of poly(butyl acrylate

Inhibitor was removed from 30g (0.24 mol) butyl acrylate by running over an alumina plug. To this 0.5%(mol/mol) AIBN and 30 ml Toluene were added. The mixture was deoxegynated and reacted at 70°C for 18 hours under oxygen free conditions. The product was precipitated into cold

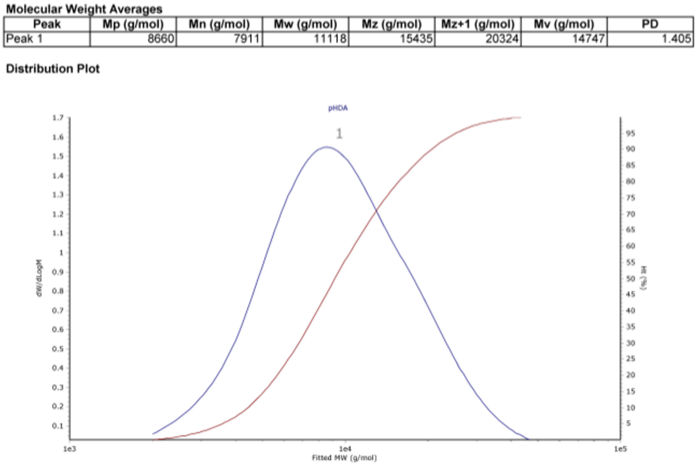

Molecular Weight Averages

Peak	Mp (g/mol)	Mn (g/mol)	Mw (g/mol)	Mz (g/mol)	Mz+1 (g/mol)	Mv (g/mol)	PD
Peak 1	8660	7911	11118	15435	20324	14747	1.405

Distribution Plot

Figure 3.12: GPC trace and calculated mass against polystyrene reference standards for pHDA measured in $CHCl_3$ at 35°C.

methanol.

Optical Spectroscopy

All optical spectroscopy experiments are performed in toluene, containing ≤ 5 μg/ml of polymer, in a quartz cuvette after filtering over a 0.2 micron PTFE syringe filter. Absorption spectra are recorded on a Shimadzu UV-2600. All fluorescence excitation, emission and lifetime measurements were performed on an Edinburgh FS5, equipped with a 372nm pulsed laser and Time-Correlated Single-Photon Counting module for lifetime measurements. All depicted spectra are an average of two consecutive measurements. Lifetime decay curves were obtained with 10^4 counts, 4095 channels in a 50ns window. Fluorescent lifetimes were obtained from a lifetime-distribution fitting procedure performed in DecayFit.

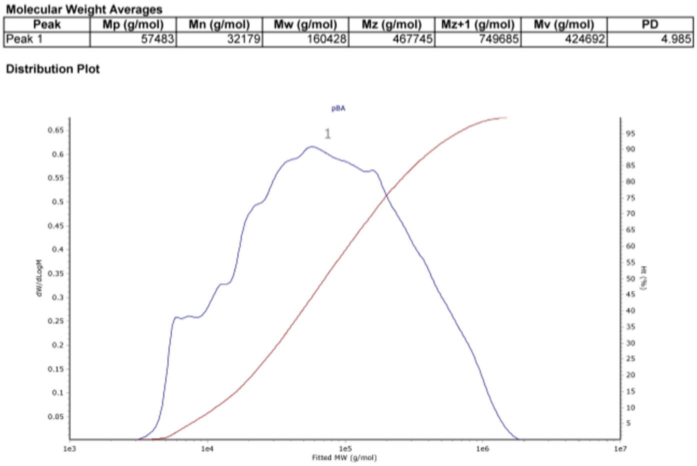

Molecular Weight Averages

Peak	Mp (g/mol)	Mn (g/mol)	Mw (g/mol)	Mz (g/mol)	Mz+1 (g/mol)	Mv (g/mol)	PD
Peak 1	57483	32179	160428	467745	749685	424692	4.985

Distribution Plot

Figure 3.13: GPC trace and calculated mass against polystyrene reference standards for pBA measured in $CHCl_3$ at 35°C.

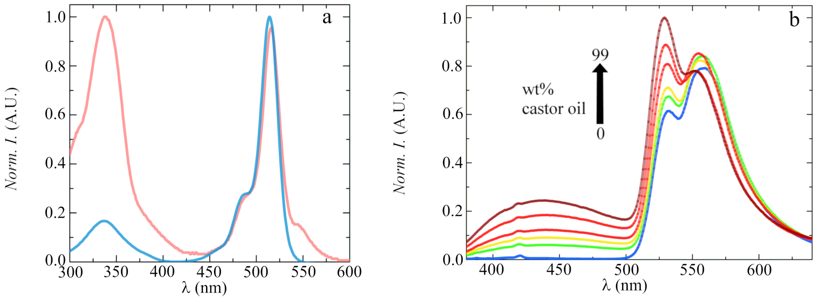

Figure 3.14: a) Normalized absorption spectra of non-brominated **1** (blue) and **2b** (red) in toluene. In the absorption spectrum of **2b** there is a red-shifted shoulder present which is indicative of aggregation. and b) fluorescence emission spectra ($\lambda_{ex} = 372nm$) in different wt % of castor oil in toluene (0, 30, 45, 60, 83, 99 wt %) normalized to the highest peak. The first peak of the acceptor emission is slightly responsive to the increasing viscosity whereas the second peak shows little response to viscosity. This supports the idea that the shoulder is cause by aggregation resulting in an unresponsive acceptor emisison peak. The donor emission features of the **2b** have broadened with those in the **2a** and show a response in intensity to the viscosity. Rendering its use as an internal reference innefective.

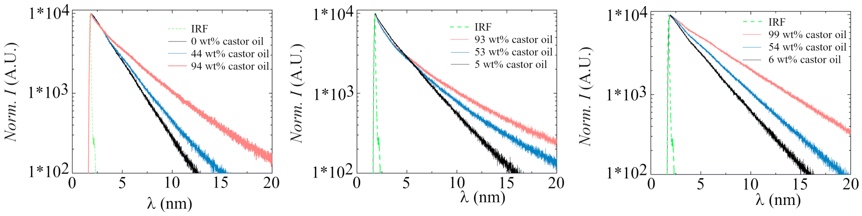

Figure 3.15: Representive lifetime decay traces ($\lambda_{em} = 580$nm and 540nm respectively) of non-brominated **1**, **2b** and **2a** in different mixtures of castor oil and toluene. Where **1** and **2a** show single-exponential decays the **2b** shows bi-exponential decays at higher viscosity which could be attributed to the unresponsive red-shifted emission band thought to be caused by aggregation.

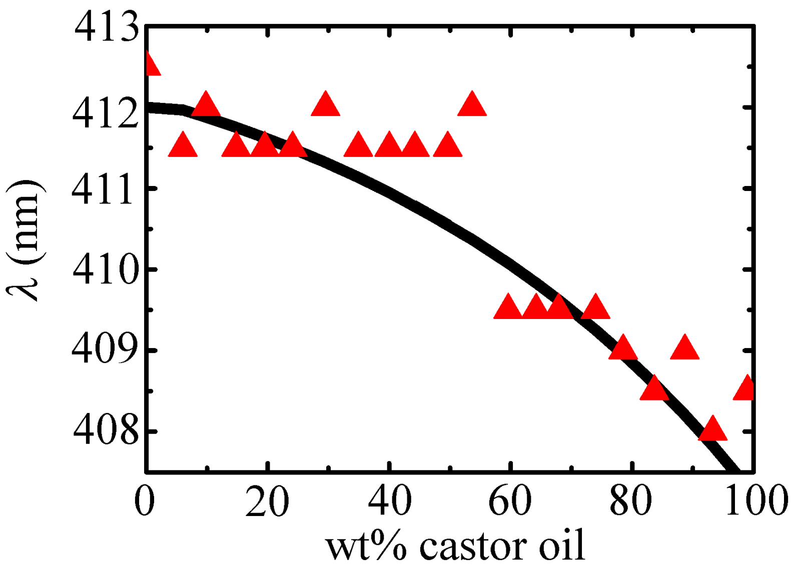

Figure 3.16: Maximum emission wavelength as a function of wt% castor oil for **2a** obtained from the emission spectra of Fig.4a in the main text.

Table 3.1: Absorption and emission maxima for sensor 1 & 2

Sensor	λ_{abs}(nm)	λ_{emm}(nm)
1	366, 516	412, 529
2	340, 516	417, 555

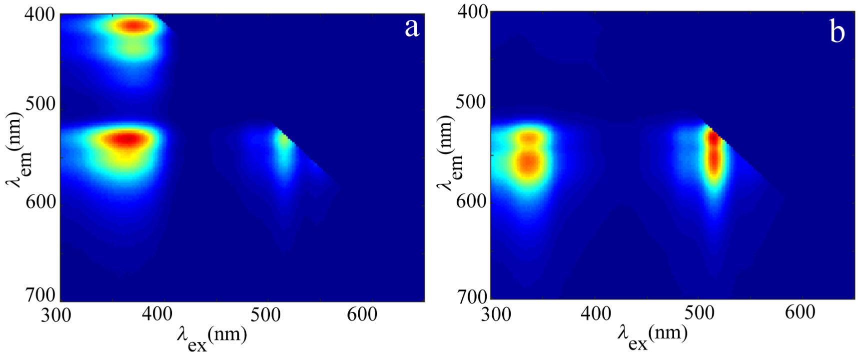

Figure 3.17: 2D excitation-emission scan of **2a** and **2b** in chloroform.

Confocal fluorescence microscopy

We prepared a solution of 10wt% pHDA and 10 wt% pBA in chloroform. To this 0.5 wt% of rigidochromic sensor **2a** was added, with respect to total polymer mass. The polymer solution was spincoated onto a coverslip at 2000 rpm. Solvent was removed by placing the sample in a vacuum stove at 40°C for 3 days. Imaging experiments were performed on a Nikon C2 confocal scanning laser microscope, with an excitation source at 405 nm. The donor and acceptor emission, upon donor excitation, were detected on two spectrally-split PMT detectors, recorded through a 60x/1.40 oil immersion objective.

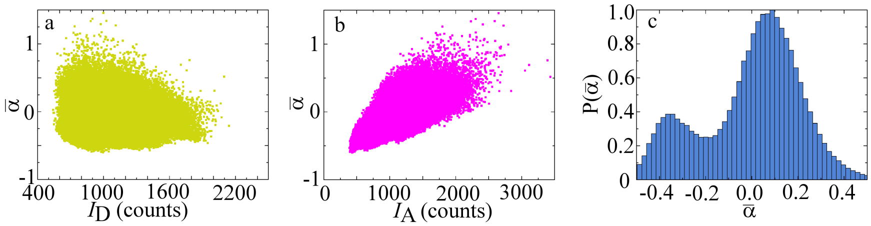

Figure 3.18: Correlation analysis shows the normalised ratio per pixel as a function of donor intensity (a) and acceptor intensity (b). Histogram of normalised ratios shows two distinct mechanical populations, corresponding to the two domains (c).

References

[1] Miyaura, N., Yanagi, T. & Suzuki, A. The palladium-catalyzed cross-coupling reaction of phenylboronic acid with haloarenes in the presence of bases. *Synthetic Communications* **11**, 513–519 (1981).

[2] Cingil, H. E. *et al.* Illuminating the reaction pathways of viromimetic assembly. *Journal of the American Chemical Society* **139**, 4962–4968 (2017).

[3] Cingil, H. E. *et al.* Monitoring protein capsid assembly with a conjugated polymer strain sensor. *Journal of the American Chemical Society* **137**, 9800–9803 (2015).

Chapter 4

Chain length-dependent luminescence in acceptor-doped conjugated polymers

Semiconducting polymers doped with a minority fraction of energy transfer acceptors feature a sensitive coupling between chain conformation and fluorescence emission, that can be harnessed for advanced solution-based molecular sensing and diagnostics. While it is known that chain length strongly affects chain conformation, and its response to external cues, the effects of chain length on the emission patterns in chromophore-doped conjugated polymers remains incompletely understood. In this paper, we explore chain-length dependent emission in two different acceptor-doped polyfluorenes. We show how the binomial distribution of acceptor incorporation, during the probabilistic polycondensation reaction, creates a strong chain-length dependency in the optical properties of this class of luminescent polymers. In addition, we also find that the intrachain exciton migration rate is chain-length dependent, giving rise to additional complexity. Both effects combined, make for the need to develop sensoric conjugated polymers of improved monodispersity and chemical homogeneity, to improve the accuracy of conjugated polymer based diagnostic approaches.

This chapter was published as:

P. van der Scheer, T. van de Laar and J. Sprakel: *Chain length-dependent luminescence in acceptor-doped conjugated polymers*, Scientific Reports, Vol. 9, (2019)

4.1 Introduction

Conjugated polymers are a versatile class of building blocks combining the properties of a polymer and a semi-conducting material. Mostly used for making advanced optical and opto-electronic materials such as photovoltaics[1, 2], OLED's[3, 4] and insulated molecular wires[5, 6], displays, memories, batteries. In addition to their value in creating physical opto-electronic devices and active layers, conjugated polymers have recently emerged as a valuable platform to build molecular diagnostic tools in solution. These approaches rely on the effectuation of conformation changes of the conjugated polymer, e.g. by analyte binding or mechanical stretching, and the resulting alteration of the luminescence pattern. The relationship between luminescence emission and chain conformation is complex, depending on a variety of factors, including the chemical composition, presence of chromophores, chain length, solubility and intermolecular interactions. For conjugated homopolymers, these effects have, e.g., been harnassed to measure viral capsid formation, where encapsulation and subsequent stretching of the conjugated polymer lead to distinct changes in the vibronic fine structure[7], or to probe various types of analyte binding or enzymatic action by means of superquenching[8, 9]. Also more complex architectures employing conjugated homopolymers, such as polydiacetylene vesicles, have been used to detect species in solution based on changes in fluorescence emission resulting from conformational changes in the semiconducting polymer.[10, 11, 12]

The optical response to changes in the spatial conformation of a polymer chain can be tailored and amplified through the doping of the semiconducting chain with a minor fraction of energy transfer acceptors, positioned as chromophores along the chain. Both the excitonic transfer along the semiconducting backbone, as well as the Förster resonant energy transfer through the dielectric medium within the polymer coil, change substantially as the chain goes from a solvated and coiled conformation to one that is either stretched or collapsed. For example, extensive work in the group of Bazan has shown the sensitive, and sequence-specific, detection of small amounts of DNA based on the binding-induced conformational changes in acceptor-doped polyfluorenes [13, 14, 15]. A similar approach has been used to evaluate nanoscopic structural changes in self-assembled nanostructures during electrostatic condensation [16]. More recently, our group has shown that mechanical tension can induce a gradual transition from coil to stretched chain, that can be optically deduced down to the scale of single molecules[17], leading to their use as highly sensitive molecular tension sensors.

Most synthetic methods to produce semiconducting polymers yield rather polydisperse products. Yet, it is well established that the equilibrium chain conformation, and its sensitivity to changes in response to an external cue, depend strongly on their chain length. This poses the question how these sensory approaches based on semiconducting polymers suffer from chain polydispersity, and how the sensitivity of the measurement could potentially be tuned if the chain length can be well controlled. For several prototypical conjugated homopolymers, including polyfluorenes[18, 19, 20, 21], polythiophenes[22, 23, 24, 25], polyacetylene-[26, 24], phenylenevinylene[27, 23, 28], phenyleneethynylenes[29, 30], effects of polymerisation degree on their optoelectronic properties has been established. For example, for polyfluorenes, systematic synthesis of pure oligomers has lead to a detailed insight in how the luminescence of these polymer changes with increasing conjugation length. Above a chain length of approximately 6 repeat units, no further changes in emission patterns were observed, thereby defining the maximum conjugation length in extended chains.[18, 19] While emission properties stop changing when the polymerisation degree exceeds the conjugation length, structural properties such as the glass transition and isotropization temperature continue to evolve.[19]

By contrast, very little is known about the chain length effects on the emission patterns of conjugated polymers that are doped with a minority fraction of chromophores, despite its importance in further developing conjugated polymer-based solution diagnostics. By contrast to homopolymers, chain length effects in doped chains have both conformational and compositional origins. Due to the semiflexible backbone of many conjugated polymers, very short chain lengths result in rigid rod behavior, with little to no conformational flexibility. Indeed, previous work has shown that doped chains below their conjugation length are not effective as molecular sensors.[17] The conformational freedom of the chain continues to grow with increasing chain length, thereby increasing the sensitivity by which changes in conformation, e.g. due to analyte binding or mechanical tension, can be interrogated optically. An additional degree of complexity in minority-doped conjugated chains, which often feature a random incoorporation of the chromophore during synthesis, is the heterogeneity of the chemical composition, even if the chain length would be perfectly homogeneous. The probabilistic nature of chromophore incorporation, and the resulting variations in chemical composition between chains, results in strong variations of energy transfer efficiency within a population. We have previously shown that while acceptor-doped donor polymers can be used as ultrasensitive tension sensors, chain length has a substantial effect on the tension-optical response curve. This offers the opportunity to tune the mechano-optical response of these molecular sensors by chain length, but simultaneously highlights how polydispersity increases the experimental uncertainty in these optically-based mechanical tension assays. To increase the reliability and sensitivity of solution-based sensory platforms based on acceptor-doped conjugated polymers, it is crucial that we develop new approaches to improve the chain length and composition homogeneity, and understand which factors influence chain length dependencies in the optical response.

In this paper, we set out to understand the mechanisms of chain length dependent emission patterns in acceptor-doped semiconducting polymers. To do so, we fractionate polydisperse conjugated polymer reaction products

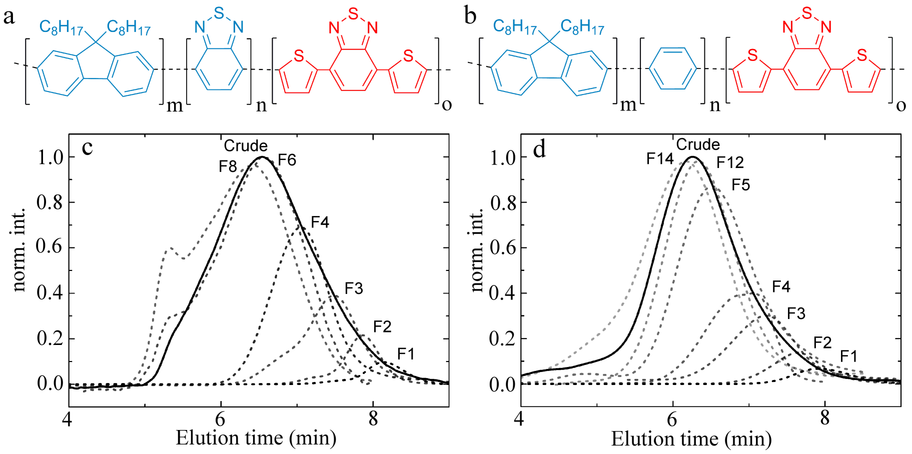

Figure 4.1: a) Chemical structure of poly(dioctylfluorene-alt-benzothiadiazole)-co-(dithienyl benzothiadiazole) ($P1$), with m=7, n=6, o=1. b) Chemical structure of poly(dioctylfluorene-alt-benzene)-co-(dithienyl benzothiadiazole) with m=6, n=7, o=1 ($P2$). c-d) Gel permeation chromatography elution traces for $P1$ (c) and $P2$ (d). The crude product is drawn as a solid line, different subfractions in dashed lines as indicated.

into series of fractions of well-defined molecular weight using solvent-gradient Soxhlet extractions. Spectroscopic analysis of fractions of donor polymers, doped with a minority fraction of acceptors, shows a strong chain length dependence in the intrachain energy transfer. We explain these results, aided by computer simulations, as the result of the binomial distribution of acceptor incorporation that ensues from the probabilistic acceptor incoorporation during the polymerisation. Furthermore, we perform this analysis on two different chemical designs, to highlight that our findings are not specific to a single chemical design, and may be generic to a much wider class of minority-doped semiconducting polymers.

4.2 Results

We explore two different chemical designs for a donor polymer doped with a small fraction of energy transfer acceptors. The first polymer ($P1$) features a green emitting backbone, composed of alternating segments of dioctyl fluorene and benzothiadazole (BT), that together form an effective green emitting donor moiety, as the energy transfer between fluorene and BT has an efficiency close to unity. The second polymer ($P2$) features a donor backbone composed of alternating dioctylfluorene and phenyl moeities, which emits in the blue. Both polymers are doped by introducing a minority fraction of dithienyl benzothiadiazole (DTBT), as a blue/green absorbing and red-emitting acceptor chromophore. The chemical structure of these two designs is illustrated in Figure4.1a-b. These designs are based on previous studies in which these architectures have been successfully used as molecular tension sensors[17], inspired by previous work in the group of Bazan on DNA detection[13, 14].

The synthesis of such doped semiconducting polymers often occurs through carbon-carbon coupling polycondensations, such as Suzuki or Yamamoto polymerizations[31, 32, 33, 34, 35, 36, 37], in which both chain length and chemical composition of the polymers is ill-controlled. Methods for controlled polymerizations of semiconducting polymers, e.g. Kumada polymerizations [38, 39, 40, 41, 42], are not readily ammenable to synthesize complex doped copolymers. As a result, the cleaned but crude product features a broad size distribution, from which it is impossible to evaluate the effects of individual fractions of chain length on the overal optical properties.

We use solvent-gradient Soxhlet extraction, used previously on both conjugated and non-conjugated polymers [43, 44, 45, 46], to fractionate the polydisperse crude mixture into fractions of increasing lenth with improved monodispersity. The normalized gel permeation chromatography elution traces are shown in Figure4.1c-d; these data illustrate that we obtain fractions spanning a rather broad range of molecular weights with improved polydispersity with respect to the starting product. This approach gives us access to a set of fractions of increasing average molecular weight (SI Fig.1a-b), all derived from the same synthesis reaction, and thus featuring identical *average* chemical composition. Proton NMR spectra of a short and long chain fraction of P1 are shown in the Supporting Information; we observe a distinct peak broadening for the longer chains due to slower molecular relaxations. The different monomers appear as a clustered set of peaks in the aromatic region; combined with the peak broadening, this makes quantitative assignement more challenging. Hence, we turn to spectroscopic means to evaluate the structure of the chains as a function of their molecular weight.

Chain-length dependent spectroscopy

Now that we have obtained a systematic set of fractions of the same polymer at different lengths, we can explore how chain length affects the optical properties of these acceptor-doped conjugated polymers, which is the main aim of this study. The UV-VIS absorption spectra, as shown in Figure4.2a-b, show distinct absorption bands for each of the different chromophores within the chain. By comparing the integrated intensities of donor and acceptor moieties, we can evaluate the ratio of donor and acceptor groups in the chemical composition of the polymer across the different fractions (see insets in Figure 4.2a-b). For polymer $P2$ we find a homogeneous chemical composition across all fractions, as the donor-to-acceptor intensity ratio α is noisy but constant, and the spectra show no systematic variations (Figure 4.2b). By contrast, for $P1$, we find that the chemical composition itself shows a chain length dependency, as the ratio α is much larger for short chain lengths, i.e. the shorter chains are enriched in donor, as compared to the higher M_w fractions. This is most likely the result of a composition-dependent solubility of short chains, where the presence of one strongly aromatic DTBT acceptor, which does not carry solubilizing alifatic tails, has a pronounced effect on the solu-

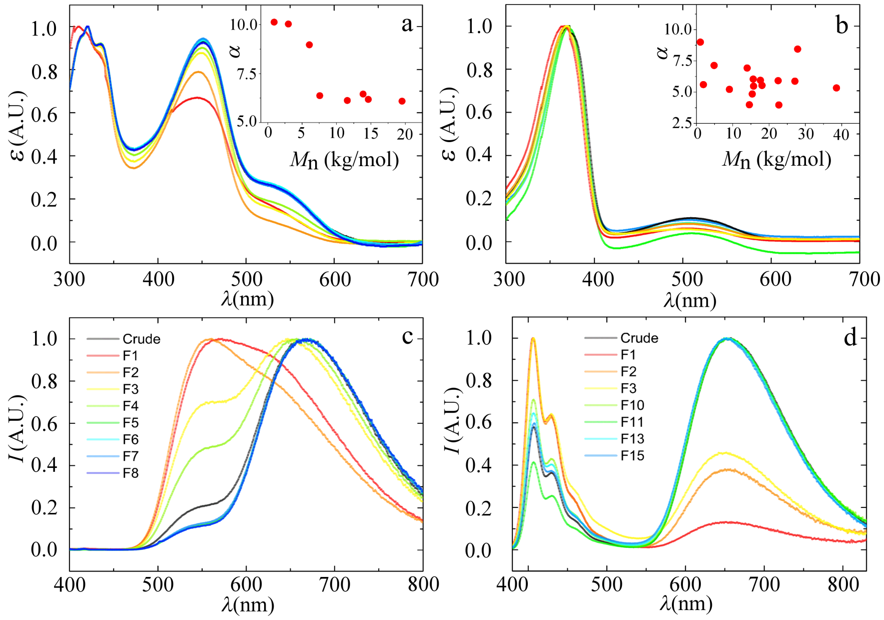

Figure 4.2: a-b) Normalised UV-VIS absorption spectra for several fractions of $P1$ (a) and $P2$ (b). Inset show the ratio α of integrated donor to acceptor absorption intensity, defined as $\alpha = \int_{370}^{500} I(\lambda) / \int_{500}^{700} I(\lambda)$ for $P1$ (a) and $\alpha = \int_{300}^{420} I(\lambda) / \int_{420}^{700} I(\lambda)$ for $P2$ (b). c-d) Corresponding normalized fluorescence emission spectra, upon donor excitation at $\lambda_{ex} = 370nm$, for several fractions of $P1$ (c) and $P2$ (d).

bility of the entire oligomer. This result illustrates the first contribution to chain-length dependent emission patterns in doped semiconducting polymers, which is a chain-length dependent chemical composition, that can emerge during polymer purification. For both polymers we do not observe substantial shifts in the wavelength of maximal absorption λ_{max}, which indicates that all fractions feature chains with degrees of polymerization that exceed the conjugation length. For polyfluorene homopolymers it is known that the conjugation length constitutes approximately 6-7 repeat units, below which the addition of each additional monomer shifts both the absorption maximum and molar exctinction coefficient

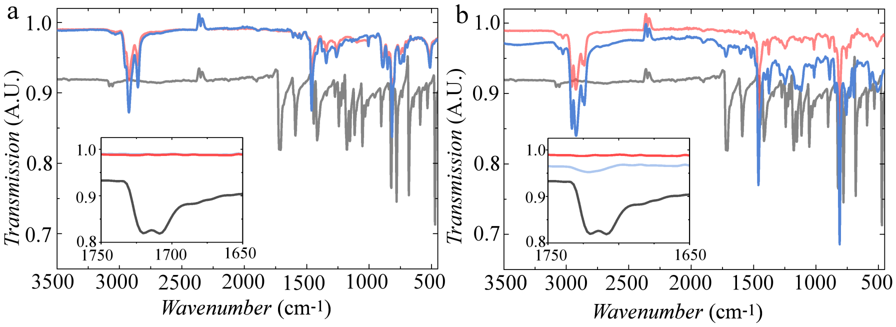

Figure 4.3: a) Transmission IR spectra of $P1 - F1$ & $P1 - F7$ in red and blue & dibromo fluorenone in black. Same data from 1750-1650 cm^{-1} inset b) Same as in a but for $P2 - F2$ & $P2 - F13$

[18, 19]. Although the spectra as shown in Figure4.2a-b, are normalized, we did not observe significant or systematic changes in the molar extinction between any of the fractions studied.

In previous studies, conformation-sensitive changes in donor-to-acceptor energy transfer have been used to deduce information about the spatial configuration of the semiconducting chains, e.g., to detect binding of DNA, proteins or block copolymers [47, 16, 13]. To probe how these effects are chain length dependent, we record the fluorescence emission of solutions of our fractionated polymers upon donor excitation at $\lambda_{ex} =$ 370 nm.

The fluorescence spectrum of $P1$ shows donor emission, from the BT moeities, at $\lambda = 550$ nm and acceptor emission from the DTBT acceptors at 680nm, for all fractions (Figure 4.2c). It is immediately clear, however, that the relative amount of acceptor emission, indicative of the efficiency of energy transfer within chains, grows with increasing length. One could speculate that this is due to the previously observed change in chemical composition in $P1$ with chain length. However, we also observe the same effect for $P2$, which is chemically more homogeneous; this polymer exhibits donor emission peaked at 415 nm, showing distinct vibronic

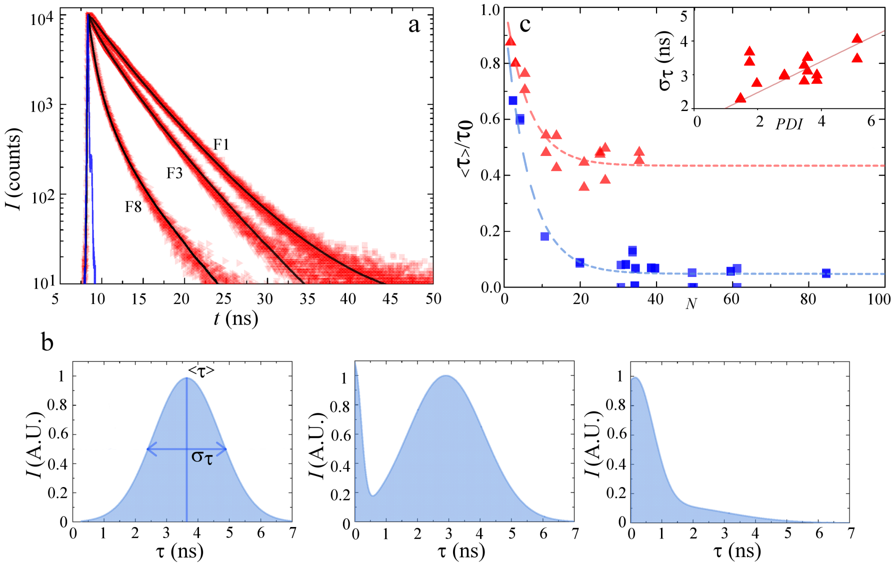

Figure 4.4: a) Time-resolved fluorescence measurements of the donor in $P1$, upon excitation at $\lambda = 372$ nm, and detection at 550 nm. Instrument response function indicated as a solid line (blue). Black lines are fits to these spectra to obtain the lifetime distributions, as shown in b). c) Normalized mean donor fluorescence lifetime as a function of chain length, expressed as the number of repeat units N, for all $P1$ (red triangles) and $P2$ (blue squares). Inset shows the width of the lifetime distributions σ_τ, as a function of polydispersity (PDI) for $P1$.

transitions in the donor emission band, characteristic for polyfluorenes, and acceptor emission at 650 nm. Also for $P2$ we observe a distinct increase in acceptor emission with increasing chain length. This suggests that the chain-length dependent luminescence is not only due to changes in chemical composition, but must have additional origins as well.

To confirm that these effects are not due to chemical defects in the chain, we realise that the most common defect in polyfluorene-based semiconducting polymers is the oxidative keto-impurity that forms from mono-alkylated fluorenes and exhibits distinct green emission [48, 49, 50]. We perform infrared spectroscopy experiments on several polymer fractions (see Figure 4.3a-b) and compare these to a reference material which is pure fluorenone. These results show that the characteristic keto-stretching mode at 1721 cm^{-1} is virtually absent in all fractions. This implies that the observed differences in the fluorescent properties of both polymers are not due to chemical-defects.

We also note that chain-end defects cannot be at the root of the observed M_w effects; one of the two polymers was carefully end-capped during the synthesis to mitigate these potential defects, while the other polymer was not. In both cases, we observe the same behaviour, thus excluding the role of chain-ends in the length-dependent emission patterns.

Finally, we note that these chain-length dependent effects are most pronounced in solution. A main application domain of semiconducting polymers is the formation of solid-state optoelectronic devices. The luminescence spectra in the solid state, as shown in the SI, give near complete energy transfer for both short and long chains. This is due to a dominant role for interchain energy transfer. We do note a distinct red-shift of the spectra in the solid state with increasing chain length. This has been previously observed in different semiconducting polymers and attributed to the formation of intramolecular stacks [51]. In solution, this pathway is suppressed and only intrachain effects emerge. Due to the recent interest in semiconducting polymers for solution-based sensoric applications, we turn our focus to the intrachain effects alone.

Time-correlated single-photon counting

To explore the origin of these effects, we turn to measurements of the lifetime of the excited state of the donor. The donor lifetime τ is a very sensitive measure for the energy transfer efficiency to acceptor moieties in the same chain; energy transfer leads to a proportional decrease in τ, making lifetime measurements the method of choice to quantify energy transfer efficiencies.

We study the chain-length dependence of the donor lifetime for the same fractions as studied in Figure 4.2. The time-resolved fluorescence decays (Figure 4.4a) show a clear decrease in donor lifetime with increasing chain length, indicating an increase in energy transfer efficiency, in line with the spectral observations in Figure 4.2. We deconvolve the time-resolved fluorescence decay curves by fitting them to a series of exponential decays to obtain the excited state lifetime distributions, as shown in Figure 4.4b. All fractions exhibit a rather broad lifetime distribution. We speculate that this is due to the internal remaining polydispersity index (PDI) within each fraction. To elucidate this point, we measure the width σ_{τ} of the donor lifetime distributions as the full-width at half maximum. We indeed find a positive, linear, correlation between the width of the chain length distribution and the width of the donor life distribution for polymer $P1$. This suggests that the lifetime of the donor backbone itself is dependent on its length and spatial conformation.

To analyse the chain-length dependent energy transfer, we measure the mean donor lifetime from the distributions (Figure 4.4b) as a function of degree of polymerisation N. Since the absolute donor lifetimes vary as a function of the chemical design of the backbone, we plot these data normalized to τ_0, which is the extrapolated donor lifetime in the limit of $N \rightarrow 0$, to reflect the relative change in τ as a function of chain length. Interestingly, we find for both polymers a significant decrease in the donor lifetime, and thus increase in energy transfer efficiency, with increasing chain length for short chains, reaching a steady-value for chains above a critical chain length N, which is approximately $N =$15 units for $P1$ and 20 units for $P2$, as shown in Figure 4.4c.

Clearly, there is a strong chain-length dependent emission in these acceptor-doped conjugated polymers, but this effect is only present for chains below a critical chain length. We have previously shown that the intramolecular FRET efficiency in these systems is a measure for the segmental density in the polymeric coil.[17] However, the fact that the chain length effect on the emission is only present for sufficiently short chains, suggests that an additional effect must be at play.

The synthesis of these co-polymers is a probabilistic process, in which the addition of monomers to growing and extending chains, is essentially random. The probability of attaching an acceptor monomer as the next addition to the chain is only determined by the ratio of donor and acceptor monomers in the reaction mixture. The number of acceptors n_A per individual chain is dictated by a binomial distribution, which depends only on the chain length N and the molar fraction of acceptors in the reaction mixture p, which is $p = 0.14$ for our experiments. The binomial distribution assumes that the selection of monomers in the sequence of N trials is independent, which we presume to hold in the early stages of the reaction where the reaction is well below conversion and an ample supply of unreacted monomers of both species is available.

The probability of finding n_A acceptors in a chain of length N, with an average acceptor fraction p set by the reaction mixture, is:

$$P(n_A) = \left(\binom{N}{n_A} \right) p^{n_A} \left(1 - p\right)^{N - n_A} . \tag{4.1}$$

The consequence of this binomial acceptor distribution across the chains is that, especially for small N, a significant fraction of chains will not have any acceptors, set by:

$$P(n_A = 0) = \left(1 - p\right)^N . \tag{4.2}$$

In these chains, the energy transfer efficiency is $E \equiv 0$ by definition. We hypothesize, that it is this fraction of acceptor-free chains that biases the energy transfer efficiency to lower values than dictated by the mean doping degree, and results in the distinct chain length dependency we observe. This hypothesis is supported by previous single-molecule experiments, in which we recorded the fluorescence spectra of very long and very short doped conjugated polymers. Indeed, these data appear to hint at a significant fraction of zero-acceptor chains for the short oligomers, while this fraction is virtually absent for the longer chains.[17]

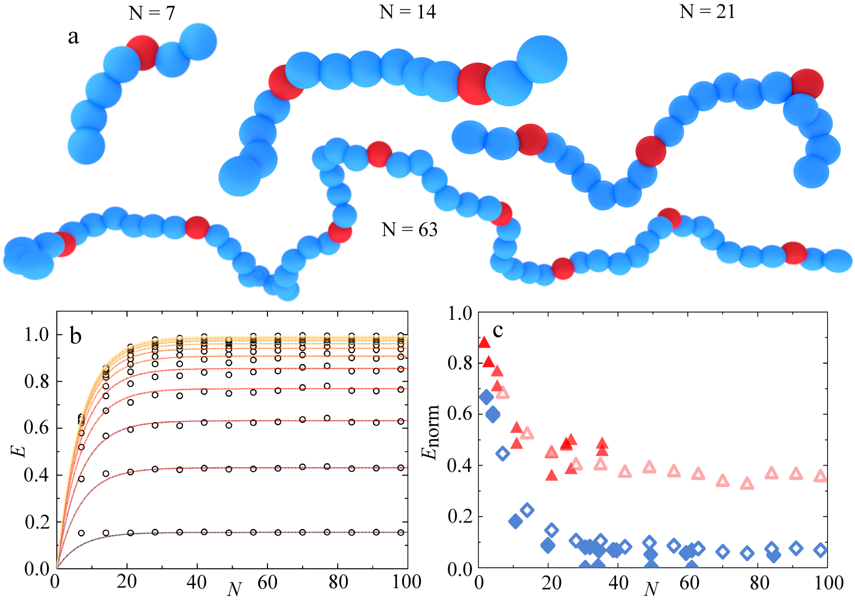

Figure 4.5: a) Computer-generated renderings of typical chain conformations with donor (blue) and acceptor (red) distributions from the BD simulations for (left-to-right) N = 7,14, 21, 63 b) Calculated energy transfer efficiency E (symbols) as a function of chain length N with increasing increasing r_f, ranging from $r_f = 1$ nm (bottom) to $r_f = 10$ nm (top). Solid lines are predictions based on the binomial distribution, as explained in the text. c) Normalized E, as explained in the text, for experimental data (filled symbols) and simulations (open symbols), for both $P1$ (red) and $P2$ (blue).

Simulations

To verify our hypothesis, we employ computer simulations to explore the role of the incorporation distribution on the intrachain energy transfer. We use Brownian Dynamics simulations to generate thermodynamic conformations for semiflexible bead-spring chains of length N, and use a theoretical approach to compute the intrachain energy transfer efficiency from these conformations (see Materials and Methods and ref.[17] for details).

Because the physical dimensions of both donor and acceptor monomers are approximately 1 nm, the coarse-grained approach of modelling the chain as a strand of identically-sized beads is reasonable. In the assignment of acceptor beads along the chain, we chose a random positioning, given one constraint, that is that two acceptors can never occupy adjacent beads. This is physically realistic due to the reaction mechanism employed in the polymer synthesis. In a Suzuki-Miyaura polycondensation, aromatic bromides react with boronic acids to form a direct C-C bond. Since the acceptors are di-bromo-functional, there can never be a direct coupling between two of these units.

These simulations, that account for the binomial acceptor distribution indeed capture the chain length dependence also observed in our experiments. The energy transfer efficiency E grows with increasing chain length N up to a critical chain length beyond which the resulting optical properties remain virtually constant (Figure 4.5c). Interestingly, this effect is very sensitive to the Förster radius r_F. The fraction of zero-acceptor chains has a E that is zero by definition. If the average energy transfer efficiency is low, due to a small r_F, the effect of this $E = 0$ population is modest, while for chains in which a substantial amount of energy is transferred to acceptors, when r_F is large, their effect is strong.

To describe these data, we realise that the ensemble-average value of $\bar{E}$, as measured in experiments, is an average of the the acceptor-free chains, which have $E = 0$, and the acceptor-rich chains. Thus, the measured $\bar{E}$ can be expressed as:

$$\bar{E} = E(n_A > 0) * (1 - (1 - p)^N)) \tag{4.3}$$

in which $E(n_A > 0)$ is the average transfer efficiency of all chains but those lacking an acceptor and the second term the overall probability of chains having $n_A > 0$. The limiting plateau value of $\bar{E}$ at high chain lengths, reflects the value in the absence of acceptor-free chains. Thus, $E(n_A > 0)$ is this plateau value, that can be directly deduced from these computations. Indeed, this form accurately describes the observed changes in $\bar{E}$ with N, as shown from the drawn lines in Figure 4.5b.

Finally, we can compare our experimental data to these simulations results directly. Given that our simulations are parametrized to match the conformational flexibility and dimensions of the experimental polymers, the only unknown is the Förster radius r_F, that sets the efficiency of the energy transfer between donors and acceptors through the dielectric solvent. To enable a comparison, we plot the experimental and theoretical data as $\frac{1-E}{1-E_0} = \frac{\tau}{\tau_0}$. By adjusting the value of r_F, we can fit the experiments and find the effective value for the Förster radius. Interestingly, the agreement between the simulations, simple theoretical description, and experimental results is excellent. This supports the hypothesis that the binomial acceptor incorporation is at least partly responsible for the observed chain-length dependencies.

It is important to note, as we will also evidence in the following section, that this simulation model is highly coarse-grained and only considers the effects of chemical inhomogeneity across a population of chains on the energy transfer. Yet, additional effects, e.g. those related to excitonic migration may very well be chain length dependent as well.

Furthermore, this allows us to measure the Förster radius indirectly. We find a good agreement between simulations and experiments for $r_f = 4.3$ nm for P1; this is close to the value previously measured at 4.9 nm for this design.[17] For $P2$ we find $r_f = 7.3$ nm; this appears high and may hint at the presence of secondary effects not captured by our coarse-grained model.

Streak imaging

Finally, to evaluate if chain length also effects the rate of excitonic migration processes along the chain we perform streak imaging experiments on dilute solutions of our polymer $P1$, such that interchain excitonic transfer is suppressed. The sample is excited with a pulse of a $\lambda = 385$ nm laser source; an example of a resulting time-resolved fluorescence streak

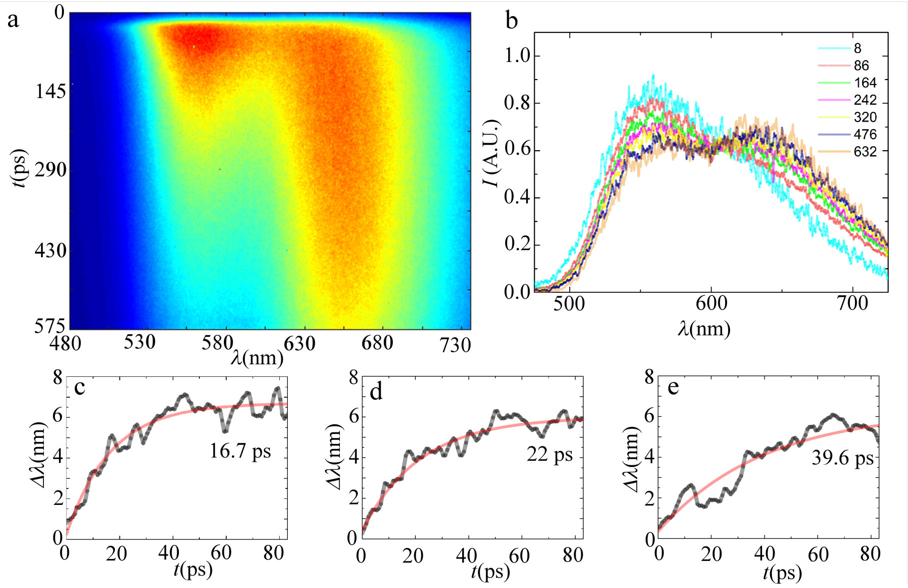

Figure 4.6: a)STREAK image of $P1-F8$ in $CHCl_3$, b) corresponding time-resolved emission spectra at selected timepoints as indicated in the legend (time in ps), c-d) initial donor redhshift as an indicator for exciton migration for $P1-F2$ (c), $P1-F3$ (d) and $P1-F8$ (e).

image is shown in Figure 4.6a.

The donor-acceptor nature of our chains gives rise to an initial donor emission, as shown in time resolved spectra in Figure 4.6b, that gradually gives way to acceptor emission, over the course of several hundreds of picoseconds to nanoseconds through energy transfer. The slow rate of this process hints at a predominance of Förster type transer. Exciton migration in these polymers is established to manifest by a distinct redshift of the donor emission peak with time.[52, 53] For each time point, we spectrally deconvolve the fluorescence spectra to identify the peak position of the donor band. Indeed we observe the temporal red shift of the donor peak that is a signature of exciton migration phenomena (see Figure 4.6c-e). We find that these data are reasonably well described by an exponential function, from which we can extract a characteristic lifetime τ_{ex} for the exciton migration process. For the longest polymer, $P1 - F8$ with $M_w = 75$ kg/mol, we find $\tau_{ex} = 39.6$ ps, which is in agreement with values reported in literature.[52, 54, 55] Also here, we observe a distinct chain length dependency; the excitonic lifetime is substantially shorter for low M_w chains, e.g. reducing to $\tau_{ex} = 16.7$ ps for $F2$ with $M_w = 2.4$ kg/mol and $\tau_{ex} = 22.0$ ps for $F3$ with $M_w = 5.9$ kg/mol of the same polymer. The shortening of the excitonic migration rate with chain length was also observed in solid films of similar polymers.[52, 56] This effect can be explained by considering exciton migration as a one-dimensional diffusion process along individual chains. The excitonic polaron diffuses along the linear chain until it reaches a chain end where it reacts and annihilates [56]. Within this picture, the characteristic lifetime for excitonic migration should grow quadratically with diffusion length and thus with molecular weight of the chain. This is in qualitative agreement with our results.

These results illustrate that the chain length dependent emission patterns we observe are due to a combination of the chemical inhomogeneity resulting from the binomial acceptor incorporation during polymer synthesis and from inherent chain-length effects on excitonic processes along the semiconducting chains.

4.3 Discussion

Doped conjugated polymers have emerged in the past years as attractive platforms to build molecular sensors, capable of detecting a wide variety of solution analytes, ranging from heavy metal ions to complex biomolecules [13], illuminating complex self-assembly processes [47, 7, 16] and enabling the optical detection of miniscule mechanical forces [17]. The inherent polydispersity that results from conjugated polymer synthesis procedures, reduces the accuracy with which signals can be quantitatively interpreted and complicates the direct comparison with theoretical models and simulations. This is particularly problematic when the optical read-out of the molecular sensor is performed at low numbers, or even at the scale of single molecules [17, 57, 58, 59], where large chain length dependencies of the optical response combined with strong polydispersity can be very disadvantageous, especially since the nature of chain length effects remain incompletely understood. In this paper we have used a sets of fractionated conjugated polymers, doped with a minority fraction of acceptor chromophores, to explore the origins of strong length-dependent emission patterns and to shed light on the role of chain polydispersity on the fidelity of sensoric approaches based on these molecular systems.

On the basis of our experiments and computer simulations, we conclude that this is caused in large part by the presence of a finite fraction of chains that do not carry even a single acceptor, due to the binomial statistics of acceptor build-in in the polymerisation reaction. We also showed that chain-length dependent exciton migration rates play a role as well in giving rise to spectral changes with alterations in the molecular weight of these doped polymers.

Removing the main source of chain-length dependent optical properties, which is a particularity of conjugated polymers doped with a minority fraction of acceptors, requires to ensure all chains carry at least one acceptor, or ideally that the acceptor positioning within the chain is well-controlled. Sequence-controlled polymerisation methods have seen a surge in development in the past year for non-semiconducting polymers [60, 61, 62, 63, 64], yet these methods remain to be explored to create sequence-controlled conjugated polymers, where efforts have been limited to the synthesis of well-defined conjugated oligomers [19, 18], that are well-below the length where the interesting coupling between chain conformation and optical response emerges.

4.4 Methods

p(F8-BT-DTBT) (P1)

Conjugated polymers composed primarily of donor moieites, and doped with a minority fraction of acceptors, are prepared via standard Suzuki-Miyaura polycondensation reactions [65, 47, 7, 17, 66, 67]. For poly(dioctyl fluorene - alt - benzothiadiazole - co - dithienyl benzothiadiazole) (P1) we dissolve 10 g (17.90mmol, 7 equivalents) 9,9-dioctylfluorene-2,7-diboronic acid bis (1,3-propanediol) ester, 1.17g (2.56mmol) 4,7-Bis(5-bromo-2-thienyl)--2,1,3-benzothiadiazole and 4.51g (15.34mmol) 4,7-Dibromobenzo[c]-1,2,5-thiadiazole in 350 ml toluene and add 150 ml 2M K_2CO_3 under nitrogen atmosphere. After thorough deoxygenation, we add 524 mg (0.716 mmol) [1,1'-Bis(diphenylphosphino) ferrocene]dichloropalladium(II). The reaction is performed for 96 hours at 100°C. The crude product is obtained by precipitation in cold methanol and Soxhlet extraction against methanol and acetone. Yield: 80% (mol/mol), 9.56g. *P1-Fraction 8: 1H NMR (600MHz, CDCl3) δ*: 8.318(s), 8.106(s), 8.05(s), 8.006-7.886(m), 7.859-7.816(m), 7.804-7.666(m), 7.581-7.52(m), 2.161(s) 1.28-1.088(m), 1.012--0.872(m), 0.8430.782(t)
13C NMR (600MHz, CDCl3) δ: 154.2, 151.69, 140.79, 136.34, 133.44, 128.29, 127.89, 123.88, 119.93, 55.46, 40.12, 31.76, 30.04, 29.22, 23.89, 22.58, 13.97

p(F62-B-DTBT) (P2)

Using the same method, we prepare poly(dioctyl fluorene - alt - benzene - co - dithienyl benzothiadiazole) (P2), using the following amounts: 5.42 gr (9.88 mmol, 6 equivalents)) 9,9-Di-(2-ethylhexyl)-2,7-dibromofluorene, 3.80g (11.53 mmol, 7 equivalents) 1,4-benzene diboronic acid bis(pinacol) ester, 756.04mg (1.65mmol, 1 equivalents)4,7-Bis(5-bromo-2-thienyl)-2,1,3-benzothiadiazole and 250mg [1,1-Bis(diphenylphosphino) ferrocene] dichloro-

palladium(II). This polymer was endcapped after 48h of reacting, by the addition of 300mg phenylboronic acid, and reacting for another 2h, followed by the injection of 2ml of de-oxygenized bromobenzene and reacting for another 12h. Yield = 78% (mol/mol), 4.22 g. %.
P1-Fraction 4C: 1H NMR (400MHz, CDCl3) δ: 7.90-7.74(m), 7.73-7.61(m), 2.13(s), 1.47-1.41(m),1.30-1.18(m), 0.91(s), 0.68(s), 0.59(s)
13C NMR (400MHz, CDCl3) δ: 151.35, 140.58, 127.57, 125.96, 122.48, 120.10, 55.21, 44.58, 34.75, 33.92, 30.33, 28.29, 27.17, 22.77, 14.00, 10.40

Fractionation

All crude polymer batches are purified from monomers, reaction by--products and residual catalyst, by Soxhlet extraction against methanol and acetone. This clean but polydisperse crude product is subsequently fractionated using solvent-gradient Soxhlet fractionation. Product is extracted in several steps, from low to high molecular weight fractions, based on chain-length dependent changes in solubility, which are particularly pronounced for the aromatic semiconducting polymers under study here. To do so, we gradually increase the solvent quality in each subsequent extraction cycle. For each fraction, we isolate the fraction by precipitation in methanol and drying under vacuo. For the initial fractions, we use a combination of hexanes and THF, which have comparable boiling points and vapor pressures, but vastly different solvent qualities. Their respective boiling points are 68°C for hexane and 66°C for THF with vapor pressures of 17.60kPa for Hexanes and 17.59kPa for THF. For high molecular weight fractions, we use mixtures of THF and chloroform, ending with pure chloroform. Details on solvent mixtures and sequence are provided in the SI. For each new solvent, the product is extracted in the Soxhlet apparatus for at least 24h for the shorter fractions and 48h for the high molecular weight fractions. For two fractions of $P2$, we iterate the fractionation a second time, by exposing an initial medium M_w fraction, to a second round of Soxhlet extraction with smaller steps of the THF-hexane mixtures.

Data

By mixing solvents of similar boiling point and vapor pressure, but with vastly different solvent qualities for the conjugated polymers, we are able to fine tune the number of fractions into which the crude product is divided. For $P2$, we initially observed a diminished separating effect for the higher molecular weight fractions. This was most likely caused by shorter chains that were physically trapped within the powder in the Soxhlet thimble, being released together with longer chains as the solvency was increased. We improved upon this, by a secondary fractionation of the initial fractions (Table 1 and 2 SI) using a similar approach. This illustrates that the Soxhlet fractionation approach, while more feasible experimentally as compared to preparative GPC approaches to obtain sufficient material, is sensitive to the physical properties of the crude powders. Fine powders, loosely packed into the thimble, ensure maximum transport of species during the extraction.

This approach gives us access to a set of fractions of increasing average molecular weight (SI figure 4.7a-b), all derived from the same synthesis reaction, and thus featuring identical average chemical composition. When plotting M_w against M_n (SI figure4.7c-d) for both polymers we can see the polydispersity, given as M_w/M_n, thus the slope of the curve in figure 4.7c-d, is improved for all but one fraction with respect to the crude product.

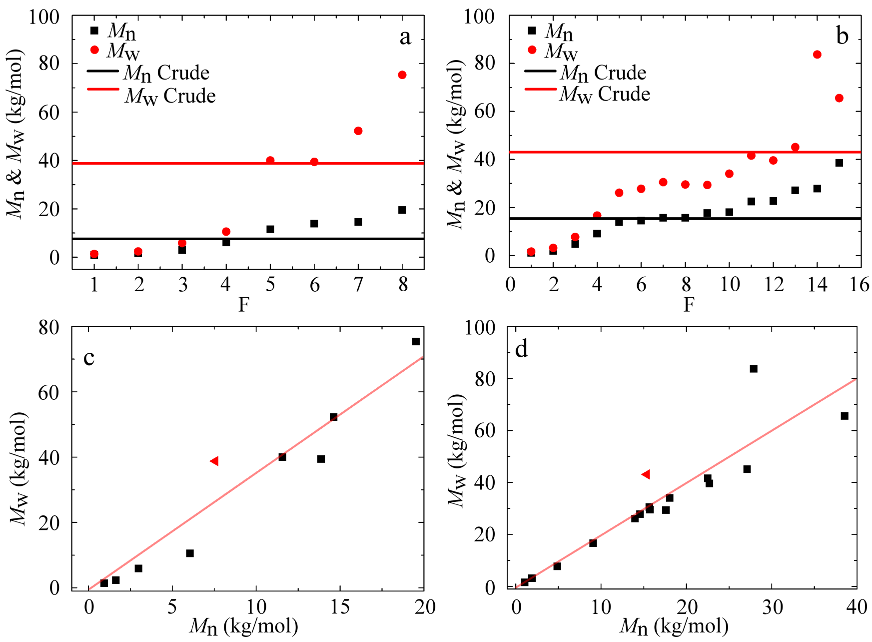

Figure 4.7: a-b) Molecular weights of $P1$ (a) and $P2$ (b) as a function of fraction number (see SI for details); average molecular weight of the crude products is indicated as solid lines. c-d) M_w as a function of M_n for the crude (red triangles) and different sub-fractions (black squares) for $P1$ (c) and $P2$ (d). The slope of the linear fit (solid red line) indicates the average polydispersity index.

GPC

Samples were prepared by dissolving 5-10mg of polymer in 2ml of chromatography-grade chloroform. The samples were heated gently to aid dissolution, and left to dissolve overnight under continuous agitation. All samples were filtrated over a 0.2 micron PTFE syringe filter prior to injection into the column. Measurements are performed at a chloroform flux of 1 ml/minute at 35°C. Molecular weights were calibrated against PS standards, and corrected to compensate for higher rigidity of the polyfluorenes as compared to the standards. [68]

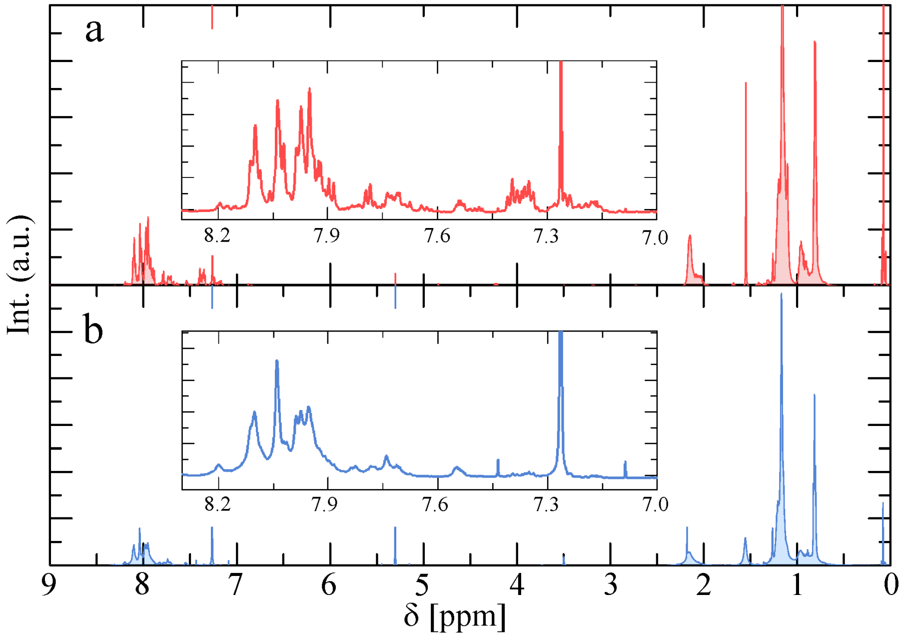

Figure 4.8: a-b)^{1}HNMR spectrum of P1-F2 & P1-F8 in $CDCl_3$

Optical Spectroscopy

All optical spectroscopy experiments are performed in chloroform solutions, containing 5 μg/ml of polymer, placed in a quartz cuvette after filtering over a 0.2 micron PTFE syringe filter. Absorption spectra are recorded on a Shimadzu UV-2600. All fluorescence excitation, emission and lifetime measurements were performed on an Edinburgh FS5, equipped with a 372nm pulsed laser and Time-Correlated Single-Photon Counting module for lifetime measurements. All depicted spectra are an average of two consecutive measurements on duplicate samples. Infrared transmission measurements were performed in the solid state on a Bruker Tensor 27 spectrometer. Time-resolved fluorescence measurements were performed with a streak camera setup (Hamamatsu model C5680 with model M5675 Synchroscan unit) at room temperature. Fs pulses were generated

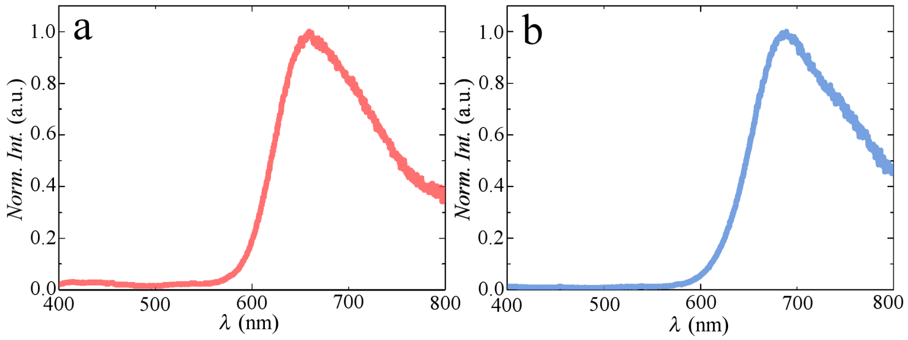

Figure 4.9: a-b)Solid state fluorescence emission spectra of P1-F1 & P1-F8. Drop-casted on quartz and excited at 370nm

P1				
Solvent	Mn (kg/mol)	Mw (kg/mol)	PDI	Fraction number
Crude	7.57	38.78	5.13	na
Acetone	0.93	1.36	1.46	1
Hexanes	1.63	2.36	1.44	2
Hexanes:THF (80:20)	2.99	5.90	1.97	3
Hexanes:THF (50:50)	6.05	10.56	1.74	4
THF	11.56	40.04	3.46	5
THF:$CHCl_3$ (90:10)	14.61	52.24	3.56	7
THF:$CHCl_3$ (70:30)	13.87	39.41	2.83	6
$CHCl_3$	19.52	75.38	3.86	8

Figure 4.10: Soxhlet extraction solvents and GPC data for P1

with a repetition rate of 75.9 MHz using a laser system (Coherent Mira 900F) to generate light at 770 nm. The repetition rate was reduced to 3.8 MHz by a puls picker (APE Berlin). The excitation wavelength was

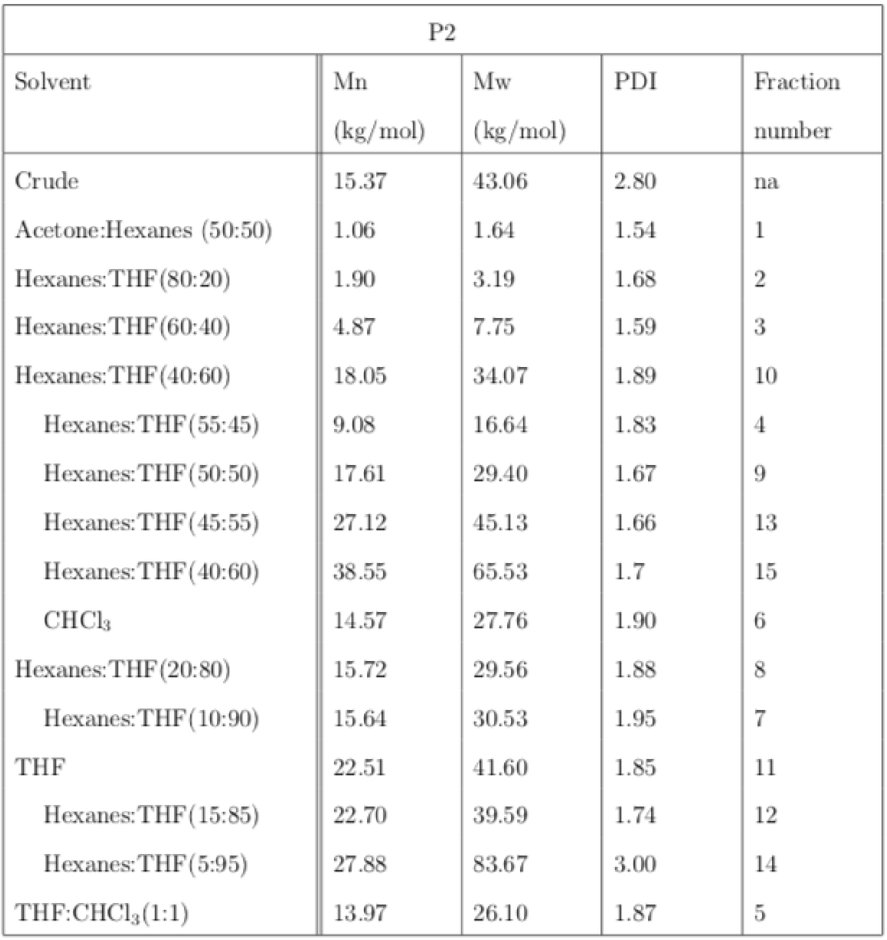

P2				
Solvent	Mn (kg/mol)	Mw (kg/mol)	PDI	Fraction number
Crude	15.37	43.06	2.80	na
Acetone:Hexanes (50:50)	1.06	1.64	1.54	1
Hexanes:THF(80:20)	1.90	3.19	1.68	2
Hexanes:THF(60:40)	4.87	7.75	1.59	3
Hexanes:THF(40:60)	18.05	34.07	1.89	10
Hexanes:THF(55:45)	9.08	16.64	1.83	4
Hexanes:THF(50:50)	17.61	29.40	1.67	9
Hexanes:THF(45:55)	27.12	45.13	1.66	13
Hexanes:THF(40:60)	38.55	65.53	1.7	15
$CHCl_3$	14.57	27.76	1.90	6
Hexanes:THF(20:80)	15.72	29.56	1.88	8
Hexanes:THF(10:90)	15.64	30.53	1.95	7
THF	22.51	41.60	1.85	11
Hexanes:THF(15:85)	22.70	39.59	1.74	12
Hexanes:THF(5:95)	27.88	83.67	3.00	14
THF:$CHCl_3$(1:1)	13.97	26.10	1.87	5

Figure 4.11: Soxhlet extraction solvents and GPC data forP2

made by frequency doubling (APE Berlin) the output of the Ti:sapphire laser. The laser power was reduced to 30 mW (with a focal spot of 150 μm). Measurements were performed at room temperature within a 800ps time-window from 480-730nm.

Simulations

To rationalise our experimental findings, we complement the measurements by in-silico predictions of the chain-length dependence of the intrachain Förster energy transfer in acceptor-doped conjugated donor polymers. We begin by computing thermodynamic polymer chain conformations, using Brownian Dynamics simulations, performed in HOOMD-Blue.[69, 70] We model our polymers as semiflexible bead-spring chains in a good solvent with a degree of polymerisation N, using a modified version of the Kremer-Grest model [71] that includes a bending penalty to impart semiflexibility [72, 73].

All beads along the chain interact by the steeply repulsive Weeks-Chandler-Anderson potential:

$$U_{WCA} \begin{cases} 4\epsilon \left[\left(\frac{\sigma}{r}\right)^{12} - \left(\frac{\sigma}{r}\right)^{6} \right] + C(r_{cut}) & r \leq r_{cut} \\ 0 & r > r_{cut} \end{cases} \tag{4.4}$$

in which σ is the particle diameter, r the distance between two particles, r_{cut} the cut-off distance and $C(r_{cut})$ a vertical shift factor, which using $r_{cut} = 2^{1/6}$ and $C(r_{cut}) = 1$ gives a purely repulsive potential, and ϵ sets the energy scale. Bonded beads interact via a finitely-extensible nonlinear elastic (FENE) spring:

$$U_{FENE} \begin{cases} \frac{-kr_{max}}{2} \ln \left[1 - \left(\frac{r}{r_{max}} \right)^{2} \right] & r \leq r_{max} \\ \infty & r > r_{max} \end{cases} \tag{4.5}$$

where k is the spring constant and r_{max} set the maximum spring extension, here fixed as $r_{max} = 1.5\sigma$. To model the semiflexibility of the polyfluorenes we study in this paper, we also include a bending penalty between adjacent bonds:

$$U_{bend}(\theta_{ijk}) = \kappa[1 - cos(\theta_{ijk})] \tag{4.6}$$

where θ_{ijk} is the bond angle between beads i, j and k, and κ the bending rigidity of the chain.

We parametrize the simulations to match the experimental polymers. Both donor and acceptor moieties in our chains have a dimension of approximately 1 nm, we thus set the bead size $\sigma = 1$ nm. The persistence length l_p, of our donor chains, copolymers of dioctyl fluorene and either benzothiadiazole ($P1$) or phenyl ($P2$), is unknown. However, these data are known for pure homopolymer poly(dioctyl fluorene), measured to be $l_p \sim 7$ nm [74], which is stiff due to the hairy-rod architecture, while alternating copolymers of equimolar mixtures of dioctyl fluorene and our acceptor DTBT, is estimated at $l_p \sim 2$ nm [75]. We estimate that for the non-stoichiometric copolymers we use here, the effective persistence length will be approximately 4 nm. Within our simulation model, it is known that $l_p/\sigma \approx \kappa/k_BT$, we thus choose $\kappa/k_BT = 4$. A chain of given degree of polymerisation was initialized and equilibrated extensively, after which 1000 statistically-independent snapshots of chain conformations were collected.

To go from chain conformations, sampled via Brownian Dynamics simulations, to the intrachain energy transfer efficiency, we use a recently developed coarse-grained theoretical approach[17], which was shown to predict Förster resonant energy transfer (FRET) in polyfluorenes with good accuracy. We note that also excitonic processes, that occur along the semiconducting backbone, occur. In these simulations, for the sake of simplicity, we chose to focus solely on energy transfer through the dieelectric medium; previous work from our group has shown that this is a reasonable approximation [17].

Since the semiconducting chain is composed of many donors and several acceptors, the total energy transfer efficiency can be written as:

$$E = \frac{1}{n_D} \sum_{j}^{nD} \left(\frac{\sum_i^{n_A} (\frac{r_F}{r_{ij}})^6}{1 + \sum_i^{n_A} (\frac{r_F}{r_{ij}})^6} \right) \tag{4.7}$$

in which n_D and n_A are the number of donor and acceptor beads in the chain respectively, with $N = n_D + n_A$, r_{ij} the distance between donor i and acceptor j, and r_F the Förster radius, defining the distance where $E = 0.5$ for a single donor-acceptor pair. For a derivation of this result we refer to previous work[17].

For each chain length, 1000 independent chain configurations were obtained using the BD simulations. To mimic the experimental scenario of random incorporation of the monomers from the reaction mixture, we randomly assign beads a donor or acceptor identity, drawing from a binomial distribution to ensure that over the ensemble of chains, the ratio of donor to acceptor beads is identical to the experiments. For each chain conformation, we generate 10 random donor-acceptor configurations, and compute E using Eq.4.7. The calculated ensemble-averaged transfer efficiency is the mean over all 10 000 conformations generated as such for each chain length.

References

[1] Coakley, K. M. & McGehee, M. D. Conjugated polymer photovoltaic cells. *Chemistry of Materials* **16**, 4533–4542 (2004).

[2] Facchetti, A. Bonjugated polymers for organic electronics and photovoltaic cell applications. *Chemistry of Materials* **23**, 733–758 (2011).

[3] Gross, M. *et al.* Improving the performance of doped π-conjugated polymers for use in organic light-emitting diodes. *Nature* **405**, 661 (2000).

[4] Liu, Y. *et al.* Efficient thermally activated delayed fluorescence conjugated polymeric emitters with tunable nature of excited states regulated via carbazole derivatives for solution-processed oleds. *Macromolecules* **51**, 4615–4623 (2018).

[5] Swager, T. M. The molecular wire approach to sensory signal amplification. *Accounts of Chemical Research* **31**, 201–207 (1998).

[6] Lafferentz, L. *et al.* Conductance of a single conjugated polymer as a continuous function of its length. *Science* **323**, 1193–1197 (2009).

[7] Cingil, H. E. *et al.* Monitoring protein capsid assembly with a conjugated polymer strain sensor. *Journal of the American Chemical Society* **137**, 9800–9803 (2015).

[8] Fan, C. *et al.* Beyond superquenching: Hyper-efficient energy transfer from conjug-

ated polymers to gold nanoparticles. *Proceedings of the National Academy of Sciences* **100**, 6297–6301 (2003).

[9] Kumaraswamy, S. *et al.* Fluorescent-conjugated polymer superquenching facilitates highly sensitive detection of proteases. *Proceedings of the National Academy of Sciences* **101**, 7511–7515 (2004).

[10] Lee, J., Kim, H.-J. & Kim, J. Polydiacetylene liposome arrays for selective potassium detection. *Journal of the American Chemical Society* **130**, 5010–5011 (2008).

[11] Seo, S. *et al.* Polydiacetylene liposome microarray toward influenza a virus detection: Effect of target size on turn-on signaling. *Macromolecular Rapid Communications* **34**, 743–748 (2013).

[12] Yoon, B., Lee, S. & Kim, J.-M. Recent conceptual and technological advances in polydiacetylene-based supramolecular chemosensors. *Chem. Soc. Rev.* **38**, 1958–1968 (2009).

[13] Gaylord, B. S., Heeger, A. J. & Bazan, G. C. Dna hybridization detection with water-soluble conjugated polymers and chromophore-labeled single-stranded dna. *Journal of the American Chemical Society* **125**, 896–900 (2003).

[14] Hong, J., Hemme, W., Keller, G., Rinke, M. & Bazan, G. Conjugated-polymer/dna interpolyelectrolyte complexes for accurate dna concentration determination. *Advanced Materials* **18**, 878–882 (2006).

[15] Feng, L., Liu, L., Lv, F., Bazan, G. C. & Wang, S. Preparation and biofunctionalization of multicolor conjugated polymer nanoparticles for imaging and detection of tumor cells. *Advanced Materials* **26**, 3926–3930 (2014).

[16] Cingil, H. E., Boz, E. B., Wang, J., Stuart, M. A. C. & Sprakel, J. Probing nanoscale coassembly with dual mechanochromic sensors. *Advanced Functional Materials* **26**, 1420–1427 (2016).

[17] van de Laar, T. *et al.* Light from Within: Sensing Weak Strains and FemtoNewton Forces in Single Molecules. *Chem* **4**, 269–284 (2018).

[18] Klaerner, G. & Miller, R. D. Polyfluorene derivatives: effective conjugation lengths from well defined oligomers. *Macromolecules* **31**, 2007–2009 (1998).

[19] Jo, J., Chi, C., Höger, S., Wegner, G. & Yoon, D. Y. Synthesis and characterization of monodisperse oligofluorenes. *Chemistry – A European Journal* **10**, 2681–2688 (2004).

[20] Zhao, Z. *et al.* Oligo(2,7-fluorene ethynylene)s with pyrene moieties: synthesis, characterization, photoluminescence, and electroluminescence. *The Journal of Organic Chemistry* **72**, 8345–8353 (2007).

[21] Lafferentz, L. *et al.* Conductance of a single conjugated polymer as a continuous function of its length. *Science* **323**, 1193–1197 (2009).

[22] Roncali, J., Garnier, F., Lemaire, M. & Garreau, R. Poly mono-, bi- and trithiophene:

Effect of oligomer chain length on the polymer properties. *Synthetic Metals* **15**, 323 – 331 (1986).

[23] Gierschner, J., Cornil, J. & Egelhaaf, H.-J. Optical bandgaps of conjugated organic materials at the polymer limit: Experiment and theory. *Advanced Materials* **19**, 173–191 (2007).

[24] Bredas, J. L., Silbey, R., Boudreaux, D. S. & Chance, R. R. Chain-length dependence of electronic and electrochemical properties of conjugated systems: polyacetylene, polyphenylene, polythiophene, and polypyrrole. *Journal of the American Chemical Society* **105**, 6555–6559 (1983).

[25] Noriega, R. *et al.* A general relationship between disorder, aggregation and charge transport in conjugated polymers. *Nature materials* **12**, 1038 (2013).

[26] Szweda, R., Chendo, C., Charles, L., Baxter, P. N. W. & Lutz, J.-F. Synthesis of oligoarylacetylenes with defined conjugated sequences using tailor-made soluble polymer supports. *Chem. Commun.* **53**, 8312–8315 (2017).

[27] Menon, A., Dong, H., Niazimbetova, Z. I., Rothberg, L. J. & Galvin, M. E. Polydispersity effects on conjugated polymer light-emitting diodes. *Chemistry of Materials* **14**, 3668–3675 (2002).

[28] Gaylord, B. S., Wang, S., Heeger, A. J. & Bazan, G. C. Water-soluble conjugated oligomers: effect of chain length and aggregation on photoluminescence-quenching efficiencies. *Journal of the American Chemical Society* **123**, 6417–6418 (2001).

[29] Cotts, P. M., Swager, T. M. & Zhou, Q. Equilibrium flexibility of a rigid linear conjugated polymer. *Macromolecules* **29**, 7323–7328 (1996).

[30] Meier, H., Stalmach, U. & Kolshorn, H. Effective conjugation length and uv/vis spectra of oligomers. *Acta Polymerica* **48**, 379–384 (1997).

[31] Cho, S. Y., Grimsdale, A. C., Jones, D. J., Watkins, S. E. & Holmes, A. B. Polyfluorenes without monoalkylfluorene defects. *Journal of the American Chemical Society* **129**, 11910–11911 (2007).

[32] Yamamoto, T. *et al.* Preparation of π-conjugated poly (thiophene-2, 5-diyl), poly (p-phenylene), and related polymers using zerovalent nickel complexes. linear structure and properties of the π-conjugated polymers. *Macromolecules* **25**, 1214–1223 (1992).

[33] Jiang, J.-X., Trewin, A., Adams, D. J. & Cooper, A. I. Band gap engineering in fluorescent conjugated microporous polymers. *Chemical Science* **2**, 1777–1781 (2011).

[34] Sanechika, K., Yamamoto, T. & Yamamoto, A. Palladium catalyzed c–c coupling for synthesis of π-conjugated polymers composed of arylene and ethynylene units. *Bulletin of the Chemical Society of Japan* **57**, 752–755 (1984).

[35] Kuehne, A. J., Gather, M. C. & Sprakel, J. Monodisperse conjugated polymer particles by suzuki–miyaura dispersion polymerization. *Nature communications*

3, 1088 (2012).

[36] Yokoyama, A. *et al.* Chain-growth polymerization for the synthesis of polyfluorene via suzuki- miyaura coupling reaction from an externally added initiator unit. *Journal of the American Chemical Society* **129**, 7236–7237 (2007).

[37] Elmalem, E., Kiriy, A. & Huck, W. T. Chain-growth suzuki polymerization of n-type fluorene copolymers. *Macromolecules* **44**, 9057–9061 (2011).

[38] Repenko, T. *et al.* Water-soluble dopamine-based polymers for photoacoustic imaging. *Chemical communications* **51**, 6084–6087 (2015).

[39] Beryozkina, T., Senkovskyy, V., Kaul, E. & Kiriy, A. Kumada catalyst-transfer polycondensation of thiophene-based oligomers: robustness of a chain-growth mechanism. *Macromolecules* **41**, 7817–7823 (2008).

[40] Tkachov, R., Senkovskyy, V., Komber, H. & Kiriy, A. Influence of alkyl substitution pattern on reactivity of thiophene-based monomers in kumada catalyst-transfer polycondensation. *Macromolecules* **44**, 2006–2015 (2011).

[41] Wu, S., Huang, L., Tian, H., Geng, Y. & Wang, F. Licl-promoted chain growth kumada catalyst-transfer polycondensation of the "reversed" thiophene monomer. *Macromolecules* **44**, 7558–7567 (2011).

[42] Sui, A. *et al.* Controlled synthesis of polyfluorenes via kumada catalyst transfer polycondensation with ni (acac) 2/dppp as the catalyst. *Macromolecules* **45**, 5436–5443 (2012).

[43] Lehtinen, A. & Paukkeri, R. Fractionation of polypropylene according to molecular weight and tacticity. *Macromolecular Chemistry and Physics* **195**, 1539–1556 (1994).

[44] Paukkeri, R. & Lehtinen, A. Fractionation of polypropylenes using soxhlet extraction methods. *Polymer* **35**, 1673–1679 (1994).

[45] Meager, I. *et al.* Power conversion efficiency enhancement in diketopyrrolopyrrole based solar cells through polymer fractionation. *Journal of Materials Chemistry C* **2**, 8593–8598 (2014).

[46] Trznadel, M., Pron, A., Zagorska, M., Chrzaszcz, R. & Pielichowski, J. Effect of molecular weight on spectroscopic and spectroelectrochemical properties of regioregular poly (3-hexylthiophene). *Macromolecules* **31**, 5051–5058 (1998).

[47] Cingil, H. E. *et al.* Illuminating the reaction pathways of viromimetic assembly. *Journal of the American Chemical Society* **139**, 4962–4968 (2017).

[48] List, E. J., Guentner, R., Scanducci de Freitas, P. & Scherf, U. The effect of keto defect sites on the emission properties of polyfluorene-type materials. *Advanced materials* **14**, 374–378 (2002).

[49] Scherf, U. & List, E. J. Semiconducting polyfluorenes—towards reliable structure–property relationships. *Advanced Materials* **14**, 477–487 (2002).

[50] Romaner, L. *et al.* The origin of green emission in polyfluorene-based conjugated

polymers: On-chain defect fluorescence. *Advanced functional materials* **13**, 597–601 (2003).

[51] Fauvell, T. J. *et al.* Photophysical and morphological implications of single-strand conjugated polymer folding in solution. *Chemistry of Materials* **28**, 2814–2822 (2016).

[52] Ariu, M. *et al.* Exciton migration in β-phase poly(9,9-dioctylfluorene). *Phys. Rev. B* **67**, 195333 (2003).

[53] Dias, F. B. *et al.* Exciton diffusion in polyfluorene copolymer thin films: Kinetics, energy disorder and thermally assisted hopping. *ChemPhysChem* **10**, 2096–2104.

[54] Dias, F. B., Knaapila, M., Monkman, A. P. & Burrows, H. D. Fast and slow time regimes of fluorescence quenching in conjugated polyfluorene- fluorenone random copolymers: The role of exciton hopping and dexter transfer along the polymer backbone. *Macromolecules* **39**, 1598–1606 (2006).

[55] Buckley, A. *et al.* Energy transfer dynamics in polyfluorene-based polymer blends. *Chemical physics letters* **339**, 331–336 (2001).

[56] Shibano, Y., Imahori, H., Sreearunothai, P., Cook, A. R. & Miller, J. R. Conjugated “molecular wire” for excitons. *The Journal of Physical Chemistry Letters* **1**, 1492–1496 (2010).

[57] Barbara, P. F., Gesquiere, A. J., Park, S.-J. & Lee, Y. J. Single-molecule spectroscopy of conjugated polymers. *Accounts of chemical research* **38**, 602–610 (2005).

[58] Hou, L., Adhikari, S., Tian, Y., Scheblykin, I. G. & Orrit, M. Absorption and quantum yield of single conjugated polymer poly [2-methoxy-5-(2-ethylhexyloxy)-1, 4-phenylenevinylene](meh-ppv) molecules. *Nano letters* **17**, 1575–1581 (2017).

[59] Tenopala-Carmona, F., Fronk, S., Bazan, G. C., Samuel, I. D. & Penedo, J. C. Real-time observation of conformational switching in single conjugated polymer chains. *Science Advances* **4**, eaao5786 (2018).

[60] Lutz, J.-F., Ouchi, M., Liu, D. R. & Sawamoto, M. Sequence-controlled polymers. *Science* **341**, 1238149 (2013).

[61] Gutekunst, W. R. & Hawker, C. J. A general approach to sequence-controlled polymers using macrocyclic ring opening metathesis polymerization. *Journal of the American Chemical Society* **137**, 8038–8041 (2015).

[62] Matsumoto, K., Oba, Y., Nakajima, Y., Shimada, S. & Sato, K. One-pot sequence-controlled synthesis of oligosiloxanes. *Angewandte Chemie* **130**, 4727–4731 (2018).

[63] Yang, C., Flynn, J. P. & Niu, J. Facile synthesis of sequence-regulated synthetic polymers using orthogonal sufex and cuaac click reactions. *Angewandte Chemie International Edition* **57**, 16194–16199 (2018).

[64] Zhang, Z. *et al.* Synthesis of polymers with on-demand sequence structures via dually switchable and interconvertible polymerizations. *Nature communications* **9**,

2577 (2018).

[65] Miyaura, N., Yanagi, T. & Suzuki, A. The palladium-catalyzed cross-coupling reaction of phenylboronic acid with haloarenes in the presence of bases. *Synthetic Communications* **11**, 513–519 (1981).

[66] Liu, B. & Bazan, G. C. Interpolyelectrolyte complexes of conjugated copolymers and dna: platforms for multicolor biosensors. *Journal of the American Chemical Society* **126**, 1942–1943 (2004).

[67] Liu, B., Gaylord, B. S., Wang, S. & Bazan, G. C. Effect of chromophore-charge distance on the energy transfer properties of water-soluble conjugated oligomers. *Journal of the American Chemical Society* **125**, 6705–6714 (2003).

[68] Grell, M. *et al.* Chain geometry, solution aggregation and enhanced dichroism in the liquidcrystalline conjugated polymer poly(9,9-dioctylfluorene). *Acta Polymerica* **49**, 439–444 (1998).

[69] Anderson, J. A., Lorenz, C. D. & Travesset, A. General purpose molecular dynamics simulations fully implemented on graphics processing units. *Journal of Computational Physics* **227**, 5342 – 5359 (2008).

[70] Glaser, J. *et al.* Strong scaling of general-purpose molecular dynamics simulations on gpus. *Computer Physics Communications* **192**, 97 – 107 (2015).

[71] Grest, G. S. & Kremer, K. Molecular dynamics simulation for polymers in the presence of a heat bath. *Physical Review A* **33**, 3628 (1986).

[72] Storm, C. & Nelson, P. C. Theory of high-force dna stretching and overstretching. *Physical Review E* **67**, 051906 (2003).

[73] Huisman, E., Storm, C. & Barkema, G. Monte carlo study of multiply crosslinked semiflexible polymer networks. *Physical Review E* **78**, 051801 (2008).

[74] Fytas, G., Nothofer, H. G., Scherf, U., Vlassopoulos, D. & Meier, G. Structure and dynamics of nondilute polyfluorene solutions. *Macromolecules* **35**, 481–488 (2002).

[75] Vezie, M. S. *et al.* Exploring the origin of high optical absorption in conjugated polymers. *Nature materials* **15**, 746 (2016).

Chapter 5

Mechanochemical deprotection of semiconducting polymers gated by chain architecture

Mechanochemically gating the introduction of π-conjugation into light-emitting polymers opens the pathway towards the processing and manufacturing of functional polymers and devices made from them by using force. For this purpose, we here showcase a methodology relying on the protection of poly(dioctyl fluorene-*co*-anthracene) polymers by Diels-Alder adducts with maleimide. While π-conjugation is effectively interrupted in this form, thermal or mechanochemical activation of the protected polymer induces the cycloelimination to anthracene gradually reforming the conjugated polymer backbone on demand. Importantly, we find that increasing anthracene doping, and thus torsion within the resulting Diels-Alder adduct-containing polymers, increasingly induces conformational strain in the main-chain facilitating both thermal and mechanochemical deprotection. In addition to an unprecedented method to process and manipulate π-conjugated light-emitting polymers, we thus also show that polymer backbone rigidity and torsion considerably influence the mechanochemical reactivity of force-responsive molecular motifs.

This chapter was submitted as:

Pieter van der Scheer, Christoph Baumann, Robert Göstl and Joris Sprakell: *Mechanochemical deprotection of semiconducting polymers gated by chain architecture*

5.1 Introduction

Semiconducting and intrinsically luminescent polymers find use in a wide variety of optoelectronic applications, such as light emitting diodes,[1, 2] lasers,[3, 4, 5] field-effect transistors,[6, 7, 8] memories [9, 10, 11] and solar cells.[12, 13, 14] In all of these, the performance and properties of the device depend sensitively on the spectroscopic and optoelectronic properties of the polymeric building blocks. Tailoring these properties is typically achieved by synthetic chemical means, which offers vast design flexibility.[15, 16, 17, 18] Creating microscopic patterns in properties, such as effective conjugation length, refractive index or peak emission wavelength, enables many of these applications and is often carried out after the polymer has been synthesized and the material deposited onto a substrate. [19] One approach to achieve this is to utilize the coupling, intrinsic to many semiconducting polymers, between the spatial conformation of the chain and its luminescence properties. For example, switching the organisation of conjugated polyfluorene between an amorphous and an organised β-phase state, which can be induced through intensive electron beam radiation, can be used to write microscopic patterns of varying backbone conjugation and refractive indices in a thin film, e.g. to fabricate distributed feedback resonator lasers.[20]

The coupling between chain conformation and luminescence properties has also found use in a very different application. Semiconducting polymers can be used as molecular sensors whose operational principle uses the coupling of a conformational change induced e.g. by mechanical force or binding of an analyte to an optical response. Functionalised semiconducting polymers have, e.g., been used to detect and quantify DNA, proteins and other ionic species[21, 22, 23, 24, 25, 26] or to probe conformational changes during templated supramolecular assembly.[27, 28, 29] Mechanical stress acting on a semiflexible semiconducting macromolecule can also induce a coil-to-stretch transition resulting in a detectable optical response, enabling their use as molecular force sensors, even at the scale of single molecules.[30]

In these examples, mechanical tension induces subtle changes in the optical properties of the semiconducting polymers, sufficient for detection, but the extended π-conjugated system of the chains remains intact in both the relaxed and the mechanically stressed state. Creating a more substantial response, such as the activation and switching of extended π-conjugation along the polymer backbone would be of value, not only to amplify the mechano-optical coupling for sensory applications, but also to enable the mechanical patterning of polymer films to create micropatterned optoelectronic devices.

To date, one approach to achieve this has been reported for a particular type of semiconducting polymers, namely polyacetylenes. Xie and co-workers have shown how mechanochemically-induced cascade cycloeliminations of cyclobutane-like moieties can transform insulating polyladderene into semiconducting polyacetylene.[31, 32, 33, 34] Mechanochemical ring-opening of the ladderene mechanophores, molecules that undergo a mechanochemically induced transformation into a functional form, covalently linked in a polymer chain, leads to the formation of a semiconducting backbone, whose conjugation length increases with increased mechanical stimulation by ultrasound. Moreover, the increasing exposure of double-bonded sections of the polymer chain, not stabilized by solubilizing groups, leads to assembly of the semiconducting chains into larger superstructures broadening the spectral features of the resulting materials. While this work is of seminal character, its approach is limited to the formation of, from an applied point of view, rather unimportant and oxidation-prone polyacetylene. Expanding this concept to a wide variety of different polymers would hence be highly desirable but requires the introduction of mechanoresponsive conjugation gates that are amenable to a wide variety of semiconducting polymer chemistries. To achieve this, the mechanophore building block must gate conjugation upon force application and also be compatible to the standard C–C coupling approaches used for the synthesis of conjugated polymers.

Within the field of mechanochemistry a considerable amount of mechanophores was developed that could act as such a conjugation gate, e.g. benzocyclobutene, spiropyran and Diels-Alder (DA) adducts of anthracene and its derivatives.[35, 36, 37, 38, 39] To date, these mechanophores have been primarily used in non-conjugated materials to optically display mechanochemically induced bond scission. Their incorporation into the backbone of conjugated polymers to enable mechanochemical gating of extended π-conjugation remains unexplored.

Here, we design and synthesize semiconducting polymers with mechanochemically gated conjugation based on DA adducts of poly(dioctyl fluorene-*co*-anthracene) polymers. The DA cycloaddition of anthracene units in the main chain to maleimide derivatives interrupts conjugation along the backbone. This results in macromolecules of chemically connected, but not conjugated, small-molecule emitters. Thermal or mechanical activation of these polymers induce the retro DA reaction which restores extended π-conjugation and results in distinct bathochromic spectroscopic shifts. We show how the degree of anthracene doping in the main chain results in tunable pre-strain on the DA adduct thereby creating a variable susceptibility for the thermal and mechanical activation of extended π-conjugation.

5.2 Results and discussion

We prepare two versions of a poly(dioctyl fluorene-*co*-anthracene) polymer via Suzuki-Miyaura polymerisation[1, 28] with co-monomer ratios of 1:1 and 1:4 of anthracene:dioctyl fluorene, respectively (Fig. 5.1 and Table 5.1, experimental details in the ESI†). Synthesizing the DA adduct of these polymers by reacting the anthracene units with a maleimide derivative can be carried out in two different ways: On the one hand, P1:4 is modified post-polymerisation to its DA adduct by reacting the purified

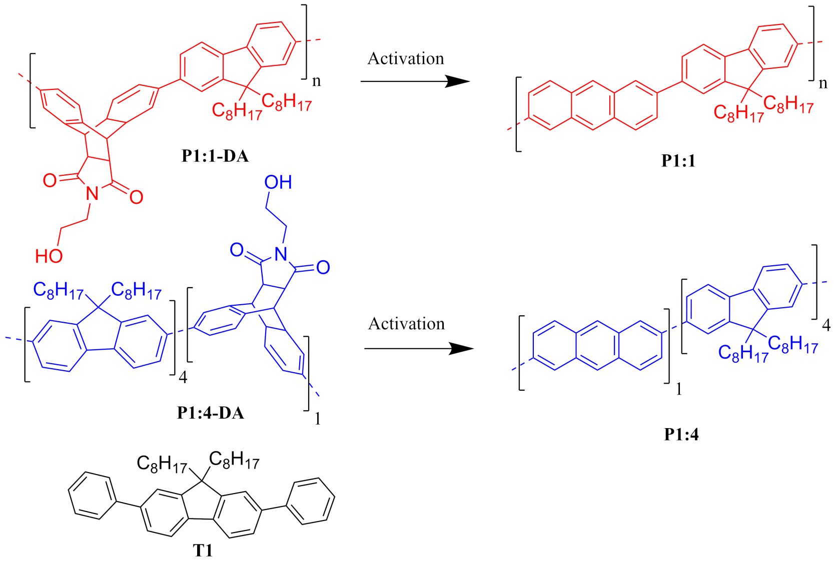

Figure 5.1: Chemical structures of both poly(anthracene-*co*-dioctylfluorene) polymers (P1:1 (red) & P1:4 (blue)) and their DA-adducts with a maleimide derivative (P1:1-DA (red) & P1:4-DA (blue)). In addition, diphenyl dioctylfluorene, denoted T1, is depicted as a reference representing the smallest conjugated repeating unit in the alternating P1:1 polymer after DA cycloaddition of the anthracene unit.

polymer with an excess of the maleimide in xylene. On the other hand, we prepare P1:1-DA in a one-pot procedure, where first a dibromoanthracene is converted to its DA adduct and subsequently this monomer is copolymerized with dioctyl fluorene.

^{1}H-NMR analysis shows that the incorporation of co-monomer ratios of 1:4 and 1:1 are in agreement with the synthetic protocol. For both preparation routes we find complete conversion to the DA adduct: ^{1}H-NMR analysis, as shown in Fig. 5.2, illustrates that peaks, at 8.6, 8.32 and 8.18 ppm, corresponding to the bare anthracene, are completely absent after the DA reaction of P1:4 with *N*-(2-hydroxyethyl)maleimide. These peaks were also absent in the P1:1-DA polymer, in which the DA adduct was prepared prior to polymerization, indicating the absence of retro DA

Polymer	M_n (kDa)	M_w (kDa)	$Đ_M$	k_{RDA} (1·min^{-1})	τ (ns)
P1:1	6.1	27.6	4.5	–	1.93
P1:1-DA	6.8	12.9	1.9	0.103	1.40
P1:4	21.8	42.5	1.95	–	1.08
P1:4-DA	–	–	–	0.006	0.42

Table 5.1: Chemical and spectroscopic properties of the 4 different polymers explored in this work, showing molar mass (M_n, M_w) and dispersity of the molar mass $Đ_M$, from GPC measurements, rate constant k_{RDA} for thermal retro DA reactions at 220 °C and the fluorescence lifetime τ.

reaction during synthesis.

For the P1:1-DA polymer, the Suzuki cross-coupling of dibromoanthracene with a dioctyl fluorene bearing protected boronic acid moieties enforces an alternating chain architecture. The completion of the DA reaction results in a polymer chain composed of small emitters, each featuring a central dioctyl fluorene group flanked on either side by a phenyl ring and interconnected by aliphatic rings. These polymers are thus fluorescent but not conjugated along the backbone. For reference, we have thus also prepared the diphenyl dioctylfluorene small molecule emitter, denoted T1 (Fig. 5.1).

Interruption of the extended π-conjugation of the copolymers results in distinct spectroscopic changes. Reducing the conjugation length along the backbone by DA cycloaddition in both cases causes a hypsochromic spectroscopic shift, as anticipated (Fig. 5.3a-b). This blue-shift is more pronounced for the 1:1 copolymer, shifting by approximately 55 nm (Fig. 5.3a), than for the 1:4 copolymer, which shifts by approximately 35 nm (Fig. 5.3b). This can be explained by the random copolymer nature of P1:4, in which larger regions of interconnected dioctylfluorene units can persist, compared to the strictly alternating nature of P1:1 ensuring that after DA protection the largest conjugated unit is diphenyl dioctylfluorene. Indeed, we observe that the spectrum of P1:1-DA is al-

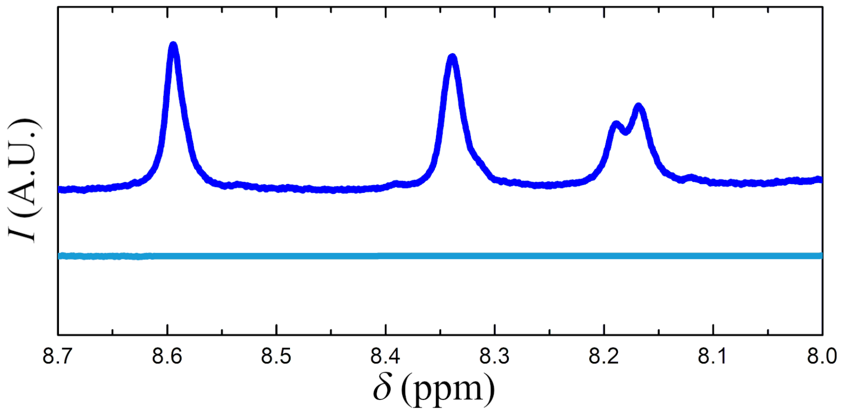

Figure 5.2: Partial ^{1}H-NMR spectra in the aromatic region of P1:4-DA (bottom) and P1:4 (top) indicating the complete disappearance of peaks specific to anthracene after DA reaction with *N*-(2-hydroxyethyl)maleimide

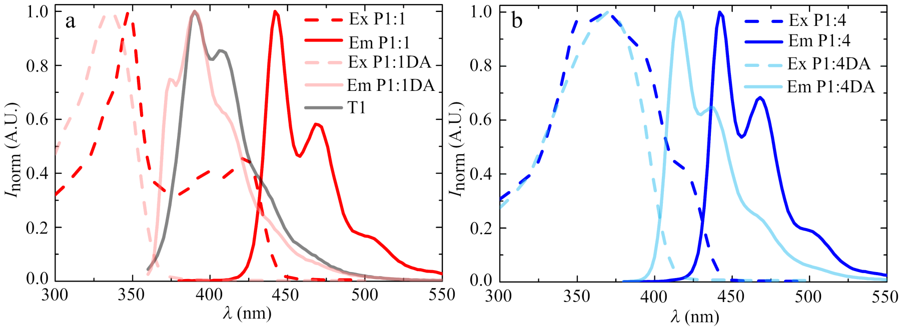

Figure 5.3: Emission and excitation spectra of a) P1:1 (dark-red, λ_{em} = 442 nm) and P1:1-DA (light-red, λ_{em} = 392 nm) and T1 (light-grey, λ_{em} = 392 nm) b) P1:4 (dark-blue, λ_{em} = 416 nm) and P1:4-DA (light-blue, λ_{em} = 442 nm)

most identical to that of the small molecule reference material T1 (Fig. 5.3a). This supports the hypothesis that after DA addition, P1:1-DA is an emitting but non-conjugated polymer composed of interlinked small-molecule emitters. We also observe almost no alteration of the photoluminescence quantum yield Φ_{PL} between P1:1 and P1:1-DA which is in line with the high Φ_{PL} reported for polyfluorene-based conjugated polymers in solution[41, 42] and values for T1 from literature.[43] This is in stark contrast to the complete absence of fluorescence from isolated anthracene molecules after DA adduct formation.[44, 45, 46, 47]

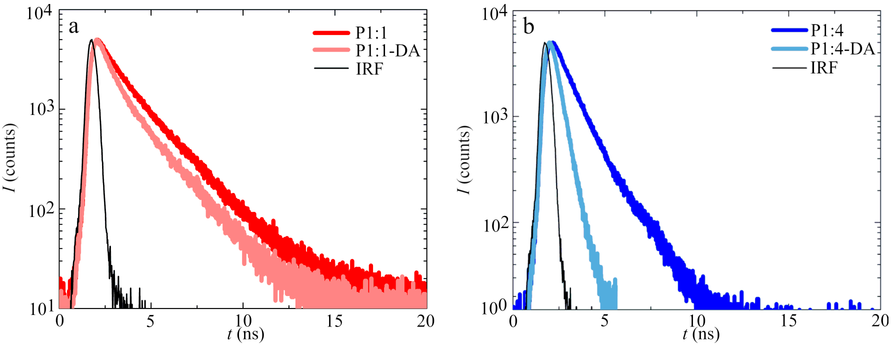

Figure 5.4: Fluorescence lifetime traces for a) P1:1 and P1:1-DA and b) P1:4 and P1:4-DA

The fluorescence lifetimes τ, determined for polymers in solution using time-correlated single photon counting (TCSPC), are substantially larger for the native polymers as compared to their DA adducts (Fig. 5.4 and Table 5.1). For P1:1 we find τ = 1.9 ns for the native polymer and 1.4 ns after DA modification. For P1:4 we find a τ = 1.1 ns before and 0.42 ns after modification. The short τ of the P1:4-DA approaches the values found for poly(dioctyl fluorene) in solution, typically around 0.3 ns,[48] and together with the spectral similarities of P1:4-DA with poly(dioctyl fluorene) hints at the presence of extended regions of oligofluorene in these random copolymers, which are the sole emitters after DA modification. We also observe that τ increases with the degree of anthracene incorporation, which might stem from native anthracene's long fluorescence lifetime of 5.2 ns.[49]

Retro DA reaction of the protected copolymers would thus result in both altered emission spectra and fluorescence lifetimes. To follow the kinetics of the retro DA reaction, during which the conjugation state of the polymer can be increased on demand, we chose fluorescence spectroscopy, as this method offers a considerably higher temporal resolution and increased sensitivity. Firstly, and as a proof of concept underlining our working hypothesis, we investigate the thermally induced retro DA reaction of the modified polymers to their extended π-conjugated forms. Above 200 °C the chemical equilibrium between anthracene and maleimide and their DA adduct shifts to the deprotected form effectively reversing the DA cycloaddition.[50]

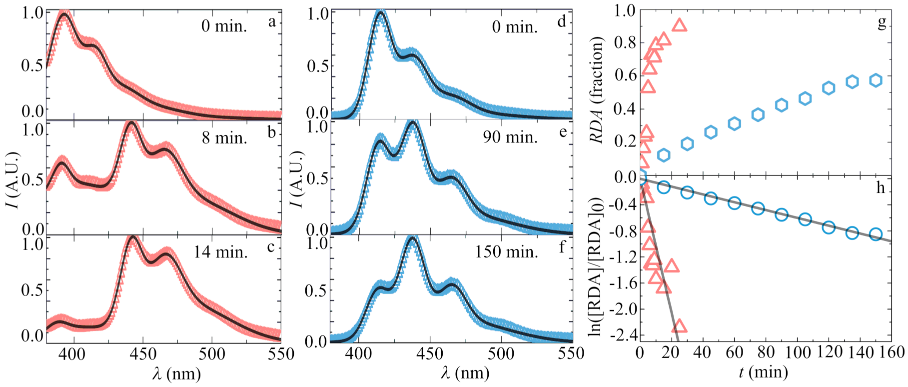

Figure 5.5: a-c) Fluorescence emission spectra of P1:1-DA during thermally induced retro DA reaction at 0, 8 and 14 min. d-f) fluorescence emission spectra of P1:4-DA during thermal retro DA reaction at 0, 90 and 150 min. Solid lines represent multi-Gaussian fits to the data used for spectral deconvolution. g) Fractional conversion to the resulting native polymers of the P1:1 (open red-triangles) and P1:4 (open blue-circles) as a function of reaction time and h) the same data in a linearized plot to confirm the first order rate law of the reaction.

For this, we prepare dilute solutions of the polymers in a high-boiling solvent in which both the DA adduct and the native polymers are well soluble (DMF:Xylene = 1:1). We heat these solutions in septumated vials using microwave radiation to 220 °C and remove small aliquots at given time points. These aliquots are diluted before recording their fluorescence emission spectrum. As time progresses, the extent of the retro DA reaction increases which can be seen in the time-evolution of the emission spectra as shown in Fig. 5.5a-f. Each spectrum represents a convolution of the DA and native states, weighted by their relative abundance in the sample. We note that for these measurements the sample was excited at 370 nm, to enable a comparison with fluorescence lifetime measurements, which excludes determination of the 355 nm peak of P1:1-DA, leaving the 392 nm peak within spectral range for accurate determination of the conversion. However, even for P1:1 there is enough spectral separation to perform a multi-Gaussian fit to the data for quantitative deconvolution. From these, we computed the relative contribution of the DA and native forms to determine the conversion of the thermal retro DA reaction as a function of time. In Fig. 5.5g we plot the fraction of native (deprotected) product formed as a function of time and observe clear difference in the rate of conjugation increase between the P1:1 and P1:4 copolymers.

The retro DA reaction of small-molecule anthracene is reported to be a first-order process.[51] To verify if this holds true for the retro DA reaction in our macromolecules, we re-plot the kinetic data as $ln([RDA]$-$/[RDA]_0)$ as a function of time with $[RDA]/[RDA]_0$ the fractional conversion. Indeed, this linearizes the data, confirming the first-order kinetics underlying the retro DA reaction. The slope gives direct access to the rate constant k_{RDA} for this reaction where We find a factor of 17 difference in the activation rate between P1:1-DA, with $k_{RDA} = 0.103$ min^{-1}, and P1:4-DA with $k_{RDA} = 0.006$ min^{-1}.

We hypothesize that this striking difference in the susceptibility to activation of the conjugation in these polymers originates in the different levels of pre-stress on the DA adduct in chains with different degrees of anthracene doping. The higher the loading level of the geometrically kinked DA adduct of anthracene in the semiflexible chains, the larger the internal strain on the monomers. It is literature-known that flexural strain on the DA adduct within a polymeric chain can enhance the retro DA reaction.[52, 53, 54] If we presume that the activation rate is enhanced exponentially with increasing internal stress, following the Bell-Evans picture of mechanically-enhanced bond rupture,[55] the factor of

17 enhancement of activation rate in P1:1 as compared to P1:4, would hint at a factor of $ln(17) = 2.8$ difference in the effective energy barrier for cycloelimination, provided solely by the chain architecture. This implies that the susceptibility to activate extended π-conjugation in these semiconducting polymers can be tailored by the chain architecture.

Increasing the degree of anthracene doping in these polymers therefore increases the internal pre-strain on the DA adducts and thereby effectively lowers the energy barrier for deprotection. Hence, it is a reasonable assumption that this difference should also reveal itself in the mechanochemical activation of the retro DA reaction without any thermal triggers. DA adducts of anthracene have been used previously as mechanophores for detecting mechanical damage with 'turn-on' fluorescence.[52, 44, 56, 46, 45, 47]

To explore the response of the DA-protected polymers to mechanical stimulation, we subjected solutions of these polymers in xylene to ultrasonication. The design of our polymers does not include a polymeric handle on the maleimide to supply a tensile force to the involved sp^3 carbons. As a result, the retro DA reaction can only be induced by a flexural mechanism.[52, 53, 54] In Fig. 5.6 we show emission spectra for the mechanical activation of P1:1-DA to P1:1 as a function of time. Clearly, mechanical stress imposed on these alternating polymers with a large internal pre-strain induced activation resulting in distinct spectroscopic shifts. Interestingly, we observe that the two main fluorescence emission bands are found at 390 nm and 415 nm, which is dissimilar to the 390 nm and 440 nm bands observed during the thermal retro DA experiments. This most likely stems from obtained gradient conjugation along the polymer backbone as mechanochemical conversion decreases gradually from the central polymer part to its chain end periphery where it almost completely ceases. Furthermore, the polymers are relatively short, which renders the imposition of forces onto the backbone and towards the mechanophore more difficult.[57]

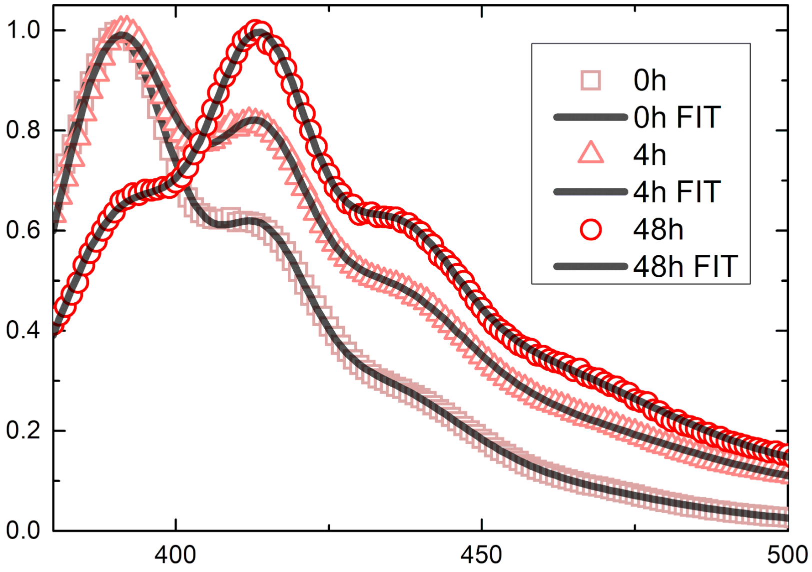

Figure 5.6: Fluorescence emission spectra of P1:1-DA during ultrasonication experiments at 0 h, 4 h and 48 h (open symbols). Solid lines are a multi-Gaussian fit for spectral deconvolution (black line).

By contrast, P1:4-DA, which we speculated to have a lower internal pre-strain on the basis of thermal retro DA experiments, did not show any signs of mechanical activation during the same experiment, even after 48 h of ultrasonic treatment. It thus becomes clear that the effect of pre-strain imposed by chain architecture has a considerable effect on the susceptibility of the polymers with gateable conjugation towards their mechanochemical activation.

In summary, we here showed how the use of anthracene-based DA mechanophores as building blocks in the main-chain of semiconducting polymers can be used to introduce conjugation gating in these systems. Moreover, we have found that changes in the doping degree can result in tunable mechanical and thermal susceptibility for the conversion of the protected to the native state which features extended π-conjugation. Tuning the mechanochemical susceptibility of these polymers could in principle be expanded by attaching polymeric tethers to the alcohol group of the maleimide creating brush-like polymers where the attachment of different chain length polymer tethers can influence the translation of forces to a central mechanophore without changing the mechanical activation of the mechanophore.[57] Since the change in main-chain architecture does not modify the chemistry or bond strength of the maleimide-anthracene DA adduct, the resulting differences in susceptibility to activation must originate from conformational strain in the backbone. The ability to tune this pre-strain by changing the architecture of the backbone creates an additional methodology to directly change the relative force required to activate the mechanophore. Additionally, the incorporation of a small molecule mechanophore into the framework of a conjugated polymer backbone enables continuous monitoring of the degree of activation of the complete macromolecular sensor. Because this can be done spectroscopically, this gives access to this information with high temporal and spatial resolution and goes beyond the 'on/off' response obtainable by a molecular DA adduct-based mechanophore.

References

[1] Friend, R. *et al.* Electroluminescence in conjugated polymers. *Nature* **397**, 121–128 (1999).

[2] Brown, A. *et al.* Conjugated polymer light-emitting diodes. In *Intrinsically conducting polymers: an emerging technology*, 87–106 (Springer, 1993).

[3] Kozlov, V., Bulović, V., Burrows, P. & Forrest, S. Laser action in organic semiconductor waveguide and double-heterostructure devices. *Nature* **389**, 362–364 (1997).

[4] Mikosch, A., Ciftci, S. & Kuehne, A. J. C. Colloidal crystal lasers from monodisperse conjugated polymer particles via bottom-up coassembly in a sol–gel matrix. *ACS Nano* **10**, 10195–10201 (2016).

[5] Coakley, K. M. & McGehee, M. D. Conjugated polymer photovoltaic cells. *Chem. Mater.* **16**, 4533–4542 (2004).

[6] Stutzmann, N., Friend, R. H. & Sirringhaus, H. Self-aligned, vertical-channel, polymer field-effect transistors. *Science* **299**, 1881–1884 (2003).

[7] Sirringhaus, H., Bird, M. & Zhao, N. Charge transport physics of conjugated polymer field-effect transistors. *Adv. Mater.* **22**, 3893–3898 (2010).

[8] Chang, J.-F., Sirringhaus, H., Giles, M., Heeney, M. & McCulloch, I. Relative importance of polaron activation and disorder on charge transport in high-mobility conjugated polymer field-effect transistors. *Phys. Rev. B* **76**, 205204 (2007).

[9] Möller, S., Perlov, C., Jackson, W., Taussig, C. & Forrest, S. R. A polymer/semiconductor write-once read-many-times memory. *Nature* **426**, 166–169 (2003).

[10] Hahm, S. G., Ko, Y.-G., Kwon, W. & Ree, M. Programmable digital polymer memories. *Curr. Opin. Chem. Eng.* **2**, 79–87 (2013).

[11] Prakash, A., Ouyang, J., Lin, J.-L. & Yang, Y. Polymer memory device based on conjugated polymer and gold nanoparticles. *J. Appl. Phys.* **100**, 054309 (2006).

[12] Chen, J.-T. & Hsu, C.-S. Conjugated polymer nanostructures for organic solar cell applications. *Polym. Chem.* **2**, 2707–2722 (2011).

[13] Helgesen, M., Søndergaard, R. & Krebs, F. C. Advanced materials and processes for polymer solar cell devices. *J. Mater. Chem.* **20**, 36–60 (2010).

[14] Hoppe, H. & Sariciftci, N. S. Polymer solar cells. In *Photoresponsive Polymers II*, 1–86 (Springer, 2007).

[15] Chujo, Y. *Conjugated polymer synthesis: methods and reactions* (John Wiley & Sons, 2011).

[16] Pouliot, J.-R., Grenier, F., Blaskovits, J. T., Beaupre, S. & Leclerc, M. Direct (hetero) arylation polymerization: simplicity for conjugated polymer synthesis. *Chem. Rev.* **116**, 14225–14274 (2016).

[17] Sakamoto, J., Rehahn, M., Wegner, G. & Schlüter, A. D. Suzuki polycondensation: Polyarylenes à la carte. *Macromol. Rapid. Commun.* **30**, 653–687 (2009).

[18] Facchetti, A., Vaccaro, L. & Marrocchi, A. Semiconducting polymers prepared by direct arylation polycondensation. *Angew. Chem. Int. Ed.* **51**, 3520–3523 (2012).

[19] Holdcroft, S. Patterning π-conjugated polymers. *Adv. Mater.* **13**, 1753–1765 (2001).

[20] Kuehne, A. J. C. *et al.* Sub-micrometer patterning of amorphous-and β-phase in a crosslinkable poly (9, 9-dioctylfluorene): Dual-wavelength lasing from a mixed-morphology device. *Adv. Funct. Mater.* **21**, 2564–2570 (2011).

[21] Liu, B. & Bazan, G. C. *Conjugated polyelectrolytes: fundamentals and applications* (John Wiley & Sons, 2013).

[22] Fonseca, S. M. *et al.* Selective fluorescence quenching in cationic fluorene-thiophene diblock copolymers for ratiometric sensing of anions. *Macromol. Rapid Commun.* **34**, 717–722 (2013).

[23] Liu, B. & Bazan, G. C. Homogeneous fluorescence-based dna detection with water-soluble conjugated polymers. *Chem. Mater.* **16**, 4467–4476 (2004).

[24] Liu, B., Baudrey, S., Jaeger, L. & Bazan, G. C. Characterization of tectorna assembly with cationic conjugated polymers. *J. Am. Chem. Soc.* **126**, 4076–4077 (2004).

[25] Fan, C. *et al.* Beyond superquenching: hyper-efficient energy transfer from conjugated polymers to gold nanoparticles. *Proc. Natl. Acad. Sci. U.S.A.* **100**, 6297–6301 (2003).

[26] Ambade, A. V., Sandanaraj, B. S., Klaikherd, A. & Thayumanavan, S. Fluorescent polyelectrolytes as protein sensors. *Polym. Int.* **56**, 474–481 (2007).

[27] Cingil, H. E. *et al.* Illuminating the reaction pathways of viromimetic assembly. *J. Am. Chem. Soc.* **139**, 4962–4968 (2017).

[28] Cingil, H. E. *et al.* Monitoring protein capsid assembly with a conjugated polymer strain sensor. *J. Am. Chem. Soc.* **137**, 9800–9803 (2015).

[29] Cingil, H. E., Boz, E. B., Wang, J., Stuart, M. A. C. & Sprakel, J. Probing nanoscale coassembly with dual mechanochromic sensors. *Adv. Funct. Mater.* **26**, 1420–1427 (2016).

[30] van de Laar, T. *et al.* Light from Within: Sensing Weak Strains and FemtoNewton Forces in Single Molecules. *Chem* **4**, 269–284 (2018).

[31] Chen, Z. *et al.* Mechanochemical unzipping of insulating polyladderene to semiconducting polyacetylene. *Science* **357**, 475–479 (2017).

[32] Su, J. K. *et al.* Synthesis and Mechanochemical Activation of Ladderene–Norbornene Block Copolymers. *J. Am. Chem. Soc.* **140**, 12388–12391 (2018).

[33] Yang, J. *et al.* Benzoladderene Mechanophores: Synthesis, Polymerization, and Mechanochemical Transformation. *J. Am. Chem. Soc.* **141**, 6479–6483 (2019).

[34] Chen, Z. *et al.* The cascade unzipping of ladderane reveals dynamic effects in mechanochemistry. *Nat. Chem.* **12**, 302–309 (2020). Number: 3 Publisher: Nature Publishing Group.

[35] Ribas-Arino, J., Shiga, M. & Marx, D. Understanding Covalent Mechanochemistry. *Angew. Chem. Int. Ed.* **48**, 4190–4193 (2009).

[36] Li, J., Nagamani, C. & Moore, J. S. Polymer Mechanochemistry: From Destructive to Productive. *Acc. Chem. Res.* **48**, 2181–2190 (2015).

[37] Akbulatov, S. & Boulatov, R. Experimental Polymer Mechanochemistry and its Interpretational Frameworks. *ChemPhysChem* **18**, 1422–1450 (2017).

[38] Willis-Fox, N., Rognin, E., Aljohani, T. A. & Daly, R. Polymer Mechanochemistry: Manufacturing Is Now a Force to Be Reckoned With. *Chem* **4**, 2499–2537 (2018).

[39] Izak-Nau, E., Campagna, D., Baumann, C. & Göstl, R. Polymer mechanochemistry-enabled pericyclic reactions. *Polym. Chem.* **11**, 2274–2299 (2020). Publisher: The Royal Society of Chemistry.

[40] Miyaura, N., Yanagi, T. & Suzuki, A. The palladium-catalyzed cross-coupling reac-

tion of phenylboronic acid with haloarenes in the presence of bases. *Syn. Commun.* **11**, 513–519 (1981).

[41] Pålsson, L.-O. *et al.* Photophysics of a fluorene co-polymer in solution and films. *Chem. Phys.* **279**, 229–237 (2002).

[42] Monkman, A., Rothe, C., King, S. & Dias, F. Polyfluorene photophysics. In *Polyfluorenes*, 187–225 (Springer, 2008).

[43] Allushi, A., Pham, T. H., Olsson, J. S. & Jannasch, P. Ether-free polyfluorenes tethered with quinuclidinium cations as hydroxide exchange membranes. *J. Mater. Chem. A* 7, 27164–27174 (2019).

[44] Göstl, R. & Sijbesma, R.P. π-extended anthracenes as sensitive probes for mechanical stress. *Chem. Sci.* 7, 370–375 (2016).

[45] Yildiz, D. *et al.* Anti-Stokes Stress Sensing: Mechanochemical Activation of Triplet–Triplet Annihilation Photon Upconversion. *Angew. Chem. Int. Ed.* **58**, 12919–12923 (2019).

[46] Stratigaki, M. *et al.* Fractography of poly(N-isopropylacrylamide) hydrogel networks crosslinked with mechanofluorophores using confocal laser scanning microscopy. *Polym. Chem.* **11**, 358–366 (2020).

[47] Izak-Nau, E. *et al.* Shear-Induced Structural and Functional Transformations of Poly(N-vinylcaprolactam) Microgels. *ACS Appl. Polym. Mater.* DOI: 10.1021/acsapm.0c00111 (2020).

[48] Dias, F. B., Knaapila, M., Monkman, A. P. & Burrows, H. D. Fast and slow time regimes of fluorescence quenching in conjugated polyfluorene- fluorenone random copolymers: The role of exciton hopping and dexter transfer along the polymer backbone. *Macromolecules* **39**, 1598–1606 (2006).

[49] Boens, N. *et al.* Fluorescence lifetime standards for time and frequency domain fluorescence spectroscopy. *Anal. Chem.* **79**, 2137–2149 (2007). PMID: 17269654.

[50] Toncelli, C. *Thermoreversibility in Polymeric Systems*, 199–248 (2011).

[51] Herndon, W. C., Grayson, C. & Manion, J. M. Retro-diels-alder reactions. iii. kinetics of the thermal decompositions of exo-and endo-dicyclopentadiene. *J. Org. Chem.* **32**, 526–529 (1967).

[52] Kabb, C. P., O'Bryan, C. S., Morley, C. D., Angelini, T. E. & Sumerlin, B. S. Anthracene-based mechanophores for compression-activated fluorescence in polymeric networks. *Chem. Sci.* **10**, 7702–7708 (2019).

[53] Gossweiler, G. R. *et al.* Mechanochemical Activation of Covalent Bonds in Polymers with Full and Repeatable Macroscopic Shape Recovery. *ACS Macro Lett.* **3**, 216–219 (2014).

[54] Larsen, M. B. & Boydston, A. J. "flex-activated" mechanophores: Using polymer mechanochemistry to direct bond bending activation. *J. Am. Chem. Soc.* **135**, 8189–

8192 (2013).

[55] Evans, E. & Ritchie, K. Dynamic strength of molecular adhesion bonds. *Biophys. J.* **72**, 1541–1555 (1997).

[56] Li, J. *et al.* Mechanophore activation at heterointerfaces. *J. Am. Chem. Soc.* **136**, 15925–15928 (2014).

[57] May, P. A., Munaretto, N. F., Hamoy, M. B., Robb, M. J. & Moore, J. S. Is molecular weight or degree of polymerization a better descriptor of ultrasound-induced mechanochemical transduction? *ACS Macro Lett.* **5**, 177–180 (2016).

5.3 Appendix

Methods

Chemicals

All chemicals and solvents were purchased from Sigma Aldrich (Merck) Europe, TCI Europe or Biosolve and used as received, unless stated otherwise.

5.3.1 Synthesis of P1:4 via Suzuki-Miyaura polymerisation [1]

To a 250 mL flask, 1396 mg (2.5 mmol) dioctyl fluorene diboronic acid propanediol ester, 822 mg (1.5 mmol) 9,9-dioctyl-2,7-dibromofluorene, 336 mg (1 mmol) 2,6-dibromoanthracene were added. The monomers were dissolved in 50 mL toluene, to which a catalytic amount of Aliquat 336 was added. Then, 40 mL of a 2 M aqueous solution of K_2CO_3 were added to the reaction mixture. The mixture was stirred and degassed by bubbling with N_2 for 45 min. To the deoxygenated mixture was added 2 mol%/(mol monomer) of the catalyst Pd(dppf)Cl_2. The flask was sealed and left to react at 100 °C for 96 h in the dark. After completion, 75 mL of toluene were added to the reaction, and the organic phase precipitated into a mixture of MeOH and 1 M HCl. The product was purified by extensive Soxhlet extraction (2 d methanol, 2 d acetone and 1 d hexane). The product was collected by Soxhlet extraction against $CHCl_3$, concentrated by rotary evaporation, precipitated into MeOH and dried *in vacuo*. Yield: 1.20 g (68 %). ^{1}**H-NMR** (400 MHz, $CDCl_3$, 300 K): δ (ppm) = 8.59(s), 8.34(s), 8.14(d), 7.95-7.5(m), 2.12(s), 1.15(s), 0.84(s). ^{13}**C-NMR** (400 MHz, $CDCl_3$, 300 K): δ (ppm) = 152.09, 140.62, 132.42, 125.94, 120.37, 55.36, 39.00, 31.81, 30.06, 29.24, 22.62, 14.08. **GPC** (against PS standards): $M_n = 21.8$ kg·mol^{-1}, $M_w = 42.5$ kg·mol^{-1} and $Đ_M$ = 1.95.

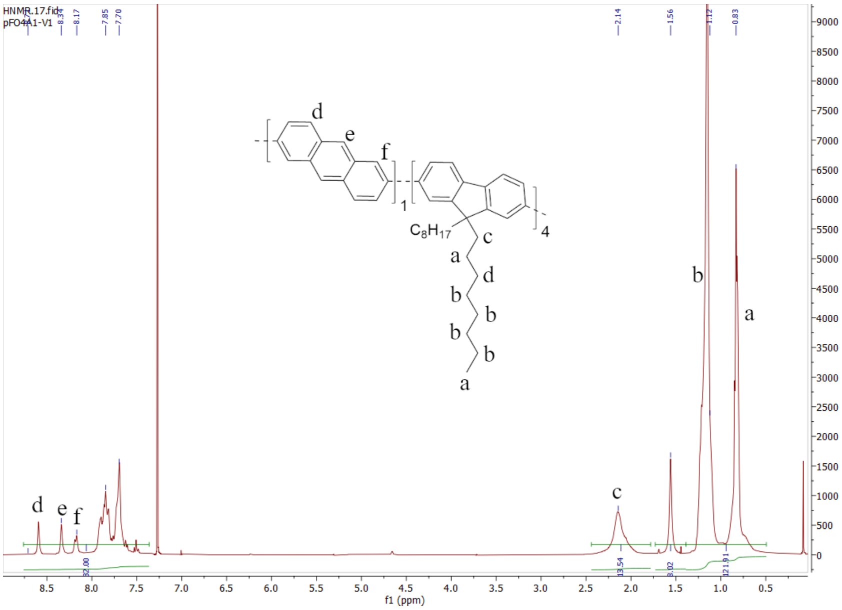

Figure 5.7: ^{1}H-NMR of **P1:4**.

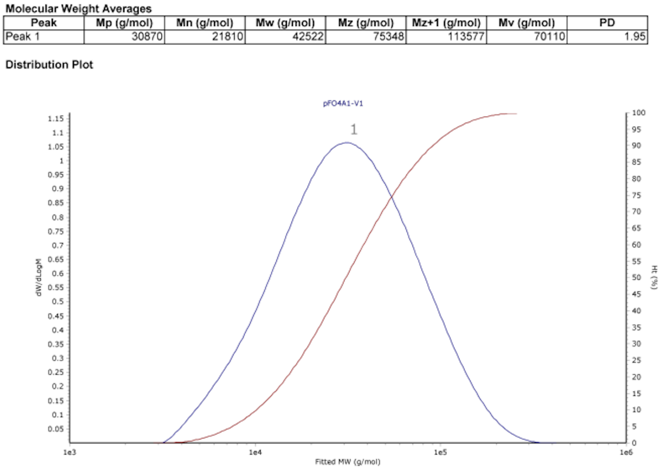
Molecular Weight Averages

Peak	Mp (g/mol)	Mn (g/mol)	Mw (g/mol)	Mz (g/mol)	Mz+1 (g/mol)	Mv (g/mol)	PD
Peak 1	30870	21810	42522	75348	113577	70110	1.95

Distribution Plot

Figure 5.8: GPC elugram of **P1:4**.

5.3.2 Synthesis of P1:4-DA

In a 25 mL glass vial, 300 mg of polymer **P1:4** (synthesized as described above) and a large excess of *N*-(2-hydroxyethyl)maleimide (50 mg) were dissolved in xylenes. The mixture was deoxygenated by bubbling with N_2 for 10 min, after which the vial was hermetically sealed. The reaction was performed at 130 °C overnight, gradually transforming from a bright yellow to a pale yellow and transparent solution. The reaction mixture was filtered and concentrated before precipitation into cold MeOH, resulting in a light yellow solid obtained in quantitative yield. ^{1}**H-NMR** (400 MHz, $CDCl_3$, 300 K): δ (ppm) = 8-7.4 (m), 5.02(s), 3.42(s), 3.18(d), 2.12(d), 1.15(s), 0.83(s). ^{13}**C-NMR** (400 MHz, $CDCl_3$, 300 K): δ (ppm) = 151.83, 140.05, 126.18, 121.50, 119.99, 60.44, 55.35, 45.67, 40.39, 31.81, 30.05, 29.23, 23.91, 22.61, 14.08.

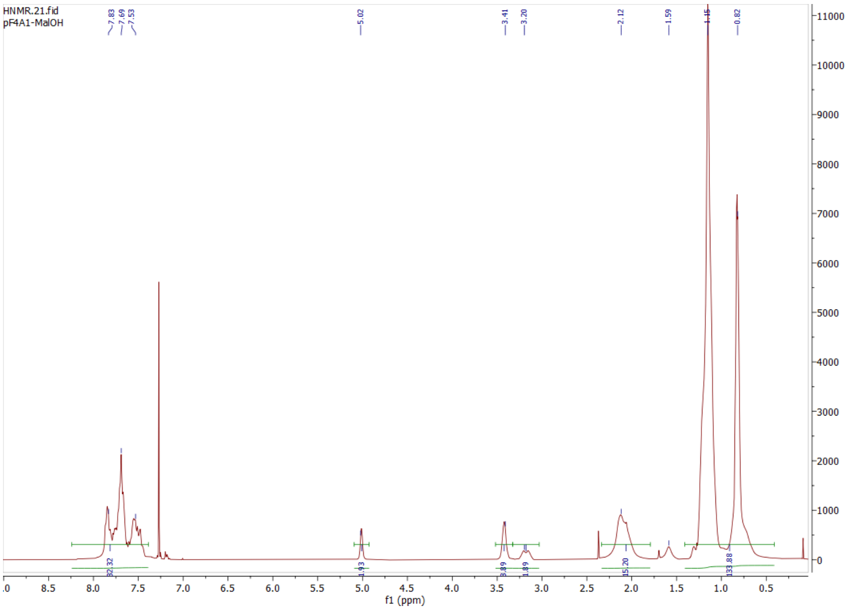

Figure 5.9: ^{1}H-NMR of **P1:4-DA**.

5.3.3 One-pot synthesis of P1:1-DA

First, we prepared the Diels-Alder adduct of 2,6-dibromoanthracene and *N*-(2-hydroxyethyl)-maleimide. To a 25 mL glass vial, were added 300 mg (0.89 mmol) 2,6-dibromoanthracene, 189 mg (1.34 mmol, 1.5× excess) N-(2-hydroxyethyl)maleimide and 10 mL toluene. The mixture was degassed by bubbling with N_2 and sealed hermetically. The mixture was left to react at 130 °C overnight in the dark. The reaction mixture, now colorless and transparent, was cooled to room temperature. To this mixture was added 572 mg (0.89 mmol) 9,9-dioctyl-9H-fluorene-2,7-diboronic acid bis(pinacol) ester, a catalytic amount of Aliquat 336 and 10 mL of a 2 M aqueous solution of K_2CO_3 (deoxygenated by purging with N_2 for 30 min prior to addition). The reaction mixture was degassed by purging with N_2 gas for 15min. To this, 2 mol%/(mol monomer) of the catalyst Pd(dppf)Cl_2 were added under an N_2 atmosphere. The vial was sealed and further deoxygenated by repeated vacuum/N_2 cycles. The mixture was left to react for 4 d at 110 °C in the dark. After cooling to RT, the organic phase was precipitated into cold MeOH. The precipitate (light grey solid) was dried *in vacuo*. Yield: 558mg. **^{1}H-NMR** (400 MHz, $CDCl_3$, 300 K): δ (ppm) = 7.9-7.15 (m), 5.0(s), 3.41(s), 3.21-3.15(m), 3.02(s), 1.06(s), 0.8(s), 0.7(s). **^{13}C-NMR** (400 MHz, $CDCl_3$, 300 K): δ (ppm) = 179.92, 162.31, 153.57, 126.17, 122.17, 122.41, 119.47, 59.02, 54.80, 45.02, 36.51, 31.39, 30.49, 29.59, 23.19, 14.45. **GPC** (against PS standards): $M_n = 6.8$ kg·mol^{-1}, $M_w = 12.9$ kg·mol^{-1} and D_M = 1.9.

5.3.4 Synthesis of **T1**

In a 25 mL vial, 100 mg (0.21 mmol) dioctyl fluorene bisboronic acid and a large excess (1 mL, 6 mmol) bromobenzene were dissolved in 5 mL toluene. To this, 5 mL of a 2 M aqueous Na_2CO_3 solution was added and the mixture degassed by purging extensively with N_2. Then, 5 mg of the catalyst Pd(dppf)Cl_2 was added and the vial was sealed. The reaction was allowed to proceed overnight at 90 °C in the dark. After cooling to RT, the organic phase was extracted with $CHCl_3$. The organic phase was dried over $MgSO_4$ and passed over a basic alumina flash column to remove the catalyst. The solvent and excess bromobenzene were removed by rotary

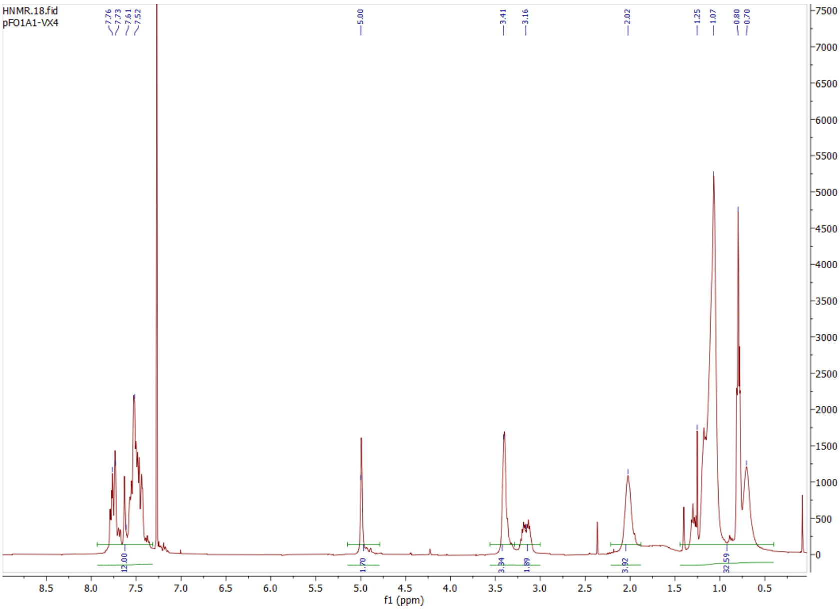

Figure 5.10: ^{1}H-NMR of **P1:1-DA**.

Molecular Weight Averages

Peak	Mp (g/mol)	Mn (g/mol)	Mw (g/mol)	Mz (g/mol)	Mz+1 (g/mol)	Mv (g/mol)	PD
Peak 1	9540	6100	27676	89426	165367	79090	4.537

Distribution Plot

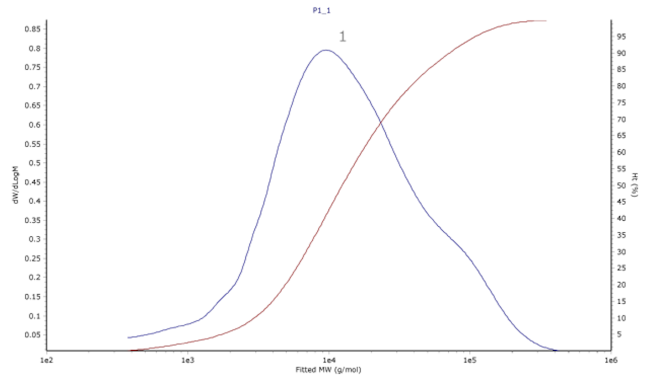

Figure 5.11: GPC trace of **P1:1**.

evaporation. Yield: 40 %. ^{1}**H-NMR** (400 MHz, $CDCl_3$, 300 K): δ (ppm) = 7.80-7.41 (m, 16H), 3.15(m, 4H), 1.19(t, 20H), 0.87 (s, 10H).

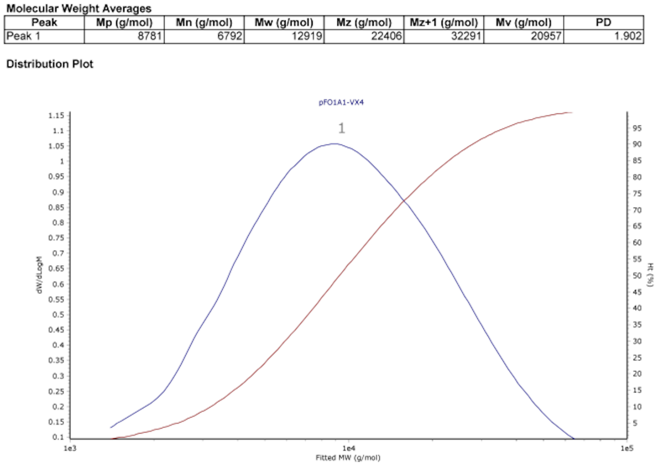

Molecular Weight Averages

Peak	Mp (g/mol)	Mn (g/mol)	Mw (g/mol)	Mz (g/mol)	Mz+1 (g/mol)	Mv (g/mol)	PD
Peak 1	8781	6792	12919	22406	32291	20957	1.902

Distribution Plot

Figure 5.12: GPC trace of **P1:1-DA**.

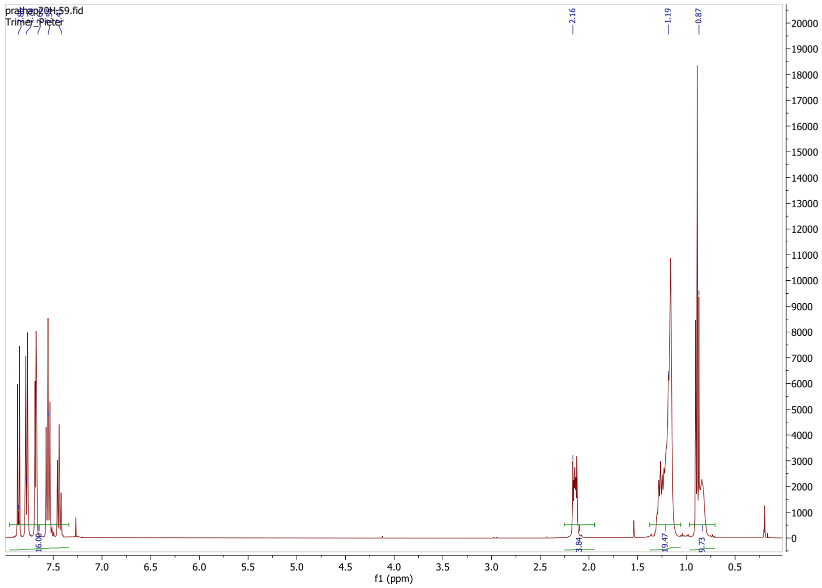

Figure 5.13: ^{1}H-NMR of **T1**.

GPC

Samples were prepared by dissolving 5-10 mg of polymer in 2 mL of chromatography-grade $CHCl_3$. The samples were heated gently to aid dissolution and left to dissolve overnight under continuous agitation. All samples were filtrated over a 0.2 μm PTFE filter prior to injection into the column. Measurements are performed with chloroform as eluens at a flux of 1 mL·min^{-1} at 35 °C. Molar masses were calibrated against PS standards.

Spectroscopy

All optical spectroscopy experiments were performed in toluene solutions, containing 5 μg·mL^{-1} of polymer, filtered over a 0.2 μm PTFE filter into quartz cuvettes. Absorption spectra were recorded on a Shimadzu UV-2600 UV-Vis spectrophotometer. All fluorescence excitation, emission and lifetime measurements were performed on an Edinburgh FS5 spectrometer, equipped with 372 nm and 405 nm pulsed lasers and Time-Correlated Single-Photon Counting module for lifetime measurements. All depicted spectra are an average of two consecutive measurements. Fluorescence lifetimes were obtained from a lifetime-distribution fitting procedure performed in DecayFit 1.4 from FluoroTools.

5.3.5 Kinetics of the thermal retro Diels-Alder reaction

Stock solutions of Diels-Alder protected polymers were prepared in a mixture of (1:1) *p*-xylene:DMF. Samples were heated to 120 °C for two minutes and subsequently filtered over a 0.2 μm PTFE filter to ensure a homogeneous solution at $t = 0$. Solutions were degassed with N_2 and sealed in a glass microwave vial. The thermal retro DA reaction was performed under microwave heating in a Biotage Initiator+ microwave. The solutions were heated at 220 °C for a pre-determined time interval, rapidly cooled (in 30 s) and a aliquot withdrawn by a syringe from the septumated vial. The aliquots were diluted in toluene prior to recording their fluorescence emission spectra.

Deconvolution of the measured emission spectra was performed by multi-Gaussian curve fitting, using a custom routine programmed in MatLab. The conversion fraction was calculated as $c = \frac{I_{438nm} - f \cdot I_{417nm}}{I_{438nm} + I_{417nm}}$, where f is a factor that specifies the ratio of the first and second vibronic peaks of the spectrum at $t = 0$. This compensates for the spectral overlap of the two states. More precisely, it corrects for the contribution of the starting material's fluorescence emission peaks (417 nm and 438 nm) to the first fluorescence emission peak of the product (438 nm).

5.3.6 Mechanochemical activation of the retro DA reaction by ultrasonication

Sonication experiments were performed on solutions of the DA polymers dissolved at 0.5 mg·mL^{-1} in a 1:1 mixture of xylenes:DMF. These solutions were subjected to ultrasonic treatments using a immersion probe sonicator (Bandelin Sonopuls GM70, maximum output power 20W) equipped with a MS72 sonication needle, at an output power of 70 % and 1 s 'on'/1 s 'off' pulse sequence. Samples were thermostated at room temperature during the sonication treatment.

References

[1] Miyaura, N., Yanagi, T. & Suzuki, A. The palladium-catalyzed cross-coupling reaction of phenylboronic acid with haloarenes in the presence of bases. *Syn. Commun.* **11**, 513–519 (1981).

Chapter 6

Fragility and Strength in Nanoparticle Glasses

Glasses formed from nano- and microparticles form a fascinating testing ground to explore and understand the origins of vitrification. For atomic and molecular glasses, a wide range of fragilities have been observed; in colloidal systems these effects can be emulated by adjusting the particle softness. The colloidal glass transition can range from a super-exponential, fragile, increase in viscosity with increasing density for hard spheres to a strong, Arrhenius-like, transition for compressible particles. However, the microscopic origin of fragility and strength remain elusive, both in the colloidal and the atomic domain. In this Chapter, we propose a simple model that explains fragility changes in colloidal glasses by describing the volume regulation of compressible colloids in order to maintain osmotic equilibrium. Our simple model not only provides a microscopic explanation for fragility, but we show that it can describe experimental data for a variety of soft colloidal systems, ranging from microgels to star polymers and proteins. Our results highlight that the elastic energy per particle acts as an effective fragility order parameter, leading to a universal description of the colloidal glass transition.

This chapter was published as:

P. van der Scheer, T. van de Laar, J. van der Gucht, D. Vlassopoulos and J. Sprakel: *Fragility and Strength in Nanoparticle Glasses*, ACS Nano. *11 (7)* (**2017**), 6755-6763.

6.1 Introduction

Suspensions of colloidal hard spheres vitrify when the particle volume fraction ϕ is increased beyond the colloidal glass transition, often identified to occur at $\phi_g \approx 0.59$ [1, 2]. Upon approaching the glass transition, the structural relaxation time of the suspension τ grows rapidly and fingerprints of the glassy state emerge, such as heterogeneous dynamics[3, 4, 5], long-lived local structures[6, 7] and percolating networks of mechanically bonded neighbors[8, 9]. Mode coupling theory (MCT) [10] has been successfully used to demarcate the transition from freely flowing fluid to a glassy state at ϕ_g. On the other hand, experiments suggest that this colloidal glass transition does not involve ergodicity breaking as predicted by MCT, but that this occurs only at slightly higher volume fractions[11].

For molecular and polymeric glasses, Angell proposed a classification scheme depending on how steeply the liquid viscosity η rises as the glass transition temperature T_g is approached [12]. When η shows a very steep, super-exponential increase with T/T_g, the glass is denoted as "fragile". By contrast, when η grows more gradually, following an exponential Arrhenius-law, the glass is classified as "strong". In other words, in a fragile glass former, even small changes in temperature can have dramatic effects on the liquid viscosity; the viscosity is more robust to small temperature fluctuations in a strong glass.

In suspensions of nanoparticles or colloids, the phase behavior of the system is governed by the volume fraction rather than temperature. For hard spheres, the structural relaxation time τ, which is proportional to the suspension viscosity, rises superexponentially as the volume fraction approaches its glass transition point ϕ_g. As a result, the hard-sphere glass can be classified as fragile, in analogy with the concept of fragility and strength for glasses formed by atomic, molecular or polymeric building blocks [12].

Also soft and compressible particles, such as microgels [13, 14, 15], star polymers [16, 17] and even globular proteins [18, 19] and cells[20, 21], exhibit a glass transition when their packing fraction approaches a critical value. However, for many of these soft systems, the fragile transition gradually gives way to a much weaker and exponential growth of the relaxation time $\tau \propto e^{\phi/\phi_g}$ [13, 20], resembling strong, Arrhenius, glasses in the molecular realm [12]. In particular for sufficiently soft microgels, ultrasoft polymer stars and suspensions of cells, a pure Arrhenius behavior has been observed experimentally [13, 16, 17, 20].

This raises the intriguing possibility that the entire range of fragility and strength known to exist for molecular systems, may be explored by studying glasses of colloids with varying softness. For example, for microgel suspensions it has been demonstrated that a transition from fragile to strong glass forming behavior could be induced solely by changing the elasticity of the individual particles. Clearly, a connection must exist between the elasticity at the scale of a single particle, and the nature of the glass transition at the macroscopic scale. For metallic glasses, such a connection was recently established quantitatively in which the "softness" of the interatomic repulsions acts as a tuning fork for fragility [22, 23]. However, such a framework does not yet exist for glasses formed from nanoparticles and colloids. As a result, a universal description of the glass transition that explains the origins of fragility and strength has to date remained unavailable.

In this chapter we propose a description for the microscopic mechanism of fragility transitions in glasses of compressible colloids, based on the regulation of osmotic equilibrium. Using a simple phenomenological model we show how apparent changes in fragility can arise when the particle softness is varied. We find that the elastic energy per particle acts as an effective order parameter for the fragility of the glass transition. A qualitative comparison of our model with experimental data suggests that a fragile-to-strong transition can be induced not only by increasing particle softness, but also by decreasing the particle size. Our results provide a framework to explain the underlying mechanisms that control the nature of the glass transition in a variety of colloidal systems.

6.2 Theoretical framework

In most experiments with purely repulsive colloidal suspensions, the phase behavior is controlled by the particle volume fraction ϕ. For hard and incompressible colloids, the state parameter is unambiguously defined as $\phi = n\frac{4}{3}\pi a^3$, where n is the number concentration of particles with radius a. For compressible particles however, defining the real particle volume fraction is more difficult. As n increases, the osmotic pressure of the bath, comprised of all particles immersed in their solvent, grows. To maintain osmotic equilibrium, compressible particles, which are equilibrated with their surroundings, must increase the pressure in the particle interior. This is accomplished by their deswelling, which increases the internal osmotic pressure of the polymer network.

Due to this osmotic equilibrium, the volume of compressible particles is not constant but becomes a function of n and as such the linear relation between number density and volume fraction is lost. The osmotic deswelling of individual compressible nano- and microparticles has been studied in detail previously[24, 25, 26, 27, 28, 29]. In experiments on microgels, the particle volume fraction is typically measured in dilute conditions and extrapolated to the concentrated regime. This extrapolated packing fraction, which is the experimental control parameter being used, is defined as $\zeta = n\frac{4}{3}\pi a_0^3$, with a_0 the particle size at infinite dilution $\phi \to 0$.

Notably, ζ is linear in n, but not in ϕ[30]; for highly compressible particles, such as soft microgels, ζ may thus increase well beyond unity when $a \ll a_0$. Due to the non-linearity between ζ and ϕ, this discrepancy cannot be resolved by normalising ζ to a characteristic state point in the particle phase diagram, for example the freezing point or glass transition. To resolve this, we propose a simple qualitative model that accounts

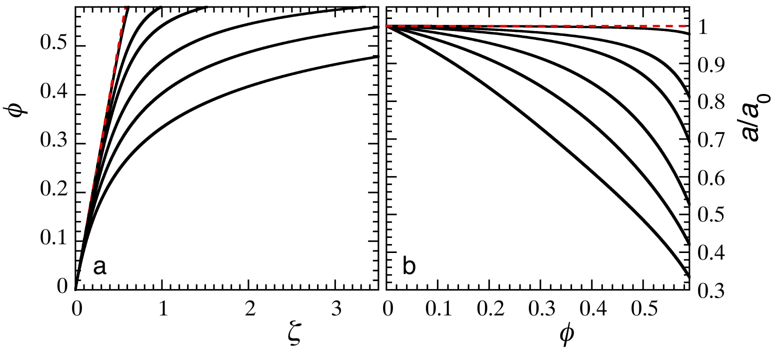

Figure 6.1: a) Real volume fraction ϕ *versus* experimental control parameter ζ as a function of particle elasticity, for (top to bottom) $k = 1 \cdot 10^4, 1 \cdot 10^3, 5 \cdot 10^2$, $2 \cdot 10^2$, $1 \cdot 10^2$ and $5 \cdot 10^1$ Pa, with $a_0 = 50$ nm and $\phi_{p,0} = 0.1$ b) Extent of osmotic deswelling a/a_0 with increasing particle volume fraction for the same settings as in a).

for osmotic shrinkage of compressible particles upon approaching their glass transition. Previously, osmotic shrinkage of compressible spheres has been postulated to lead to the lack of a glassy state all together[31] but a direct link to changes in glass fragility has not been established.

We model colloidal spheres, with equilibrium radius $a(\phi \to 0) = a_0$, where the internal volume fraction of osmolyte $\phi_p = \phi_{p,0}$. For example for microgel colloids, or polymer stars, ϕ_p represents the volume fraction of polymer segments within the particle. The microscopic details of the internal equation of state, which governs the balance between osmotic and elastic pressure within a particle,Π_{in}, vary greatly among different experimental systems. Yet, all systems in osmotic equilibrium with a bath of pure solvent must satisfy: $\Pi_{in}(\phi_{p,0}) \equiv 0$. For microgels, this is achieved by balancing a positive contribution to the internal pressure due to mixing of chains and solvent with a negative contribution resulting from entropic chain elasticity, commonly expressed within the Flory-Rehner theory for gels [32].

Rather than using a microscopic theory, such as the Flory-Rehner theory for hydrogels or the elastic description of single particle micromechanics proposed recently by Riest *et al.*[29], to describe a specific type of compressible spheres, here we start with a phenomenological description of the internal equation of state at a qualitative level such that analytical results can be obtained. The aim of this paper is to arrive at a conceptual understanding of fragility in compressible sphere packings; of course, for specific systems a more quantitative description can be derived if the internal equation-of-state, and that of the suspension bath, are known a-priori.

Here we use a phenomenological form for the sake of simplicity, inspired by the mean-field description of polymers in the marginal (*i.e.* theta-solvent conditions) and semi-dilute regime $\Pi \propto \phi_p^2$ [33]. Given the additional constraint that Π_{in} must be equal to the external pressure at equilibrium, which is zero for very dilute suspensions, we use the functional form:

$$\Pi_{in} = k\left(\phi_p^2 - \phi_{p,0}^2\right) \tag{6.1}$$

where k is an effective stiffness of the particles. We note that this can be easily changed to good-solvent conditions by changing to a power of $\frac{9}{4}$ instead of 2. Since $\phi_p/\phi_{p,0} = a_0^3/a^3$, the internal pressure can be rewritten as

$$\Pi_{in} = k\phi_{p,0}^2\left(\frac{a_0^6}{a^6} - 1\right) \tag{6.2}$$

As the overal particle concentration n increases, a significant colloidal osmotic pressure Π_{out} will develop in the bath, which we describe with the empirical equation of state proposed by Speedy [34]:

$$\Pi_{out} = \frac{s_1 n k_B T}{1 - s_2\phi} \tag{6.3}$$

in which $k_B T$ is the thermal energy and s_1 and s_2 are numerical constants. For hard spheres, it can be parametrized with $s_1 \approx 2.55$ and $s_2 = 1/\phi_{rcp} \approx 1.55$, in which ϕ_{rcp} is the random close packing fraction. Here we choose this description for the equation-of-state of the bath as it describes the pressure at finite volume fractions reasonably well and its simple form allows solving the equations analytically. The Speedy equation-of-state does not accurately represent the limit of $\phi \to 0$; however, this limit is not considered in the present work, hence we do not pursue this point further.

The underlying assumption in choosing this form is that in the limit of full deswelling of the particles, when $\phi_p \to 1$ and all solvent is expelled from the particle interior, the initially soft particles become incompressible which must lead to a divergence of the bath pressure. Moreover, this implies that at equilibrium, the bulk modulus K of the particles must be a function of its degree of deswelling. Within our approximate and phenomenological approach, the bulk modulus of the particles is indeed density-dependent and can be defined as $K = \phi_p d\Pi_{in}/d\phi_p = 2k\phi_p^2$. We note that, also here, for a quantitative description, the bath equation-of-state of the specific system must be known; for example in experiments on microgels, such as those revealing the fragility transitions with softness[13], charged residues on the particles will significantly alter the magnitude of the bath osmotic pressure. In fact, it is the ratio of the intrinsic particle softness k to the bath pressure that governs the behavior.

Using $\phi = a^3\zeta/a_0^3$, we find:

$$\Pi_{out} = \frac{3k_B T s_1 \zeta}{4\pi\left(a_0^3 - s_2 a^3 \zeta\right)} \tag{6.4}$$

At each ζ, a new equilibrium is established by reducing the particle size $a < a_0$, simultaneously increasing Π_{in} and reducing the bath pressure until $\Pi_{in} = \Pi_{out}$. With

$$\lambda = \left(\frac{a}{a_0}\right)^3 \tag{6.5}$$

and

$$A = \frac{3s_1}{4\pi s_2} \frac{k_B T}{k\phi_{p,0}^2 a_0^3} \tag{6.6}$$

we can define the equilibrium condition as:

$$\zeta = \frac{1 - \lambda^2}{s_2 \left(A\lambda^2 - \lambda^3 + \lambda\right)} \tag{6.7}$$

which gives direct access to the relationship between number density and volume fraction . Interestingly, the extent to which osmotic balance creates a non-linearity between ϕ and ζ is governed solely by the normalised elastic energy per particle $\bar{k}a_0^3/k_B T$, with $\bar{k} = k\phi_{p,0}^2$ the intrinsic particle elasticity. The elastic energy per particle is directly coupled to the external equation-of-state, since $3s_1/4\pi s_2 A = \bar{k}a_0^3/k_B T$, such that 'softness' can be defined as the relative resistance to volume changes of the particles as compared to how steep the osmotic pressure in the bath grows with ϕ.

In the limit of very soft particles $\bar{k}a_0^3 \ll k_B T$, so that osmotic shrinkage is strong $\lambda \ll 1$. In this limit Eq.6.7 is approximated as

$$\zeta \approx 1/s_2 \left(A\lambda^2 + \lambda\right) \tag{6.8}$$

which yields

$$\lambda \approx \frac{1}{2A} \left(\sqrt{1 + \frac{4A}{s_2 \zeta}} - 1 \right) \tag{6.9}$$

At high number densities, $\zeta \gg A$, this leads to $\lambda \approx 1/s_2\zeta$. With $\phi = \zeta\lambda$, we find $\phi \approx 1/s_2 = \phi_{rcp}$. This implies that for very soft particles at sufficiently high number concentrations, the system equilibrates at random close packing; addition of more particles results in a proportional isotropic compression of the system such that the volume fraction remains constant; this could explain the lack of a glassy state in certain cases[31]. We finally note that in this derivation we assume that the particles respond to increasing particle density by osmotic deswelling only, and thus that particle deformation can be ignored. This implies that the particles we describe have a Poisson's ratio $\nu < 0.5$, which is a reasonable assumption for hydrogel systems under the appropriate conditions[35].

6.3 Results & Discussion

We first evaluate the effect of particle softness, regulated by k, on the relationship between real volume fraction ϕ and extrapolated packing parameter ζ. For small colloids, $a_0 = 50$ nm, a significant bath pressure develops already at moderate volume fractions. When the particles are stiff, the hard sphere limit $\bar{k} = \infty$ is approached for which $\phi \equiv \zeta$ (dotted line Fig.6.1a). When the effective particle elasticity is reduced, and osmotic regulation effects become pronounced, the non-linearity between ζ and the real volume fraction ϕ grows. The corresponding osmotic shrinkage of the particles, expressed here by the deswelling ratio a/a_0, as shown in Fig.6.1b, can be very strong for the softest particles, with actual radii $a(\phi)$ more than a factor of 3 smaller than their fully swollen dimension a_0, at reasonable volume fractions; this is in direct agreement with experiments on microgel particles[36, 30].

To explore the implications this pronounced osmotic shrinkage has on the apparent fragility of the glass transition we adopt the ansatz that structural relaxation slows down universally with ϕ below the ideal mode-coupling glass transition. The structural relaxation time, normalised to the characteristic time of unhindered Brownian diffusion, τ/τ_0 is thus assumed to be described by a single equation as a function of ϕ. To this end, we use an equivalent of the classical VFT equation in which particle volume fraction governs the dynamics[37, 11]:

$$\log\left(\frac{\tau}{\tau_0}\right) = \frac{C}{\frac{\phi_c}{\phi} - 1} \tag{6.10}$$

where C is a numerical constant and ϕ_c is a critical volume fraction at

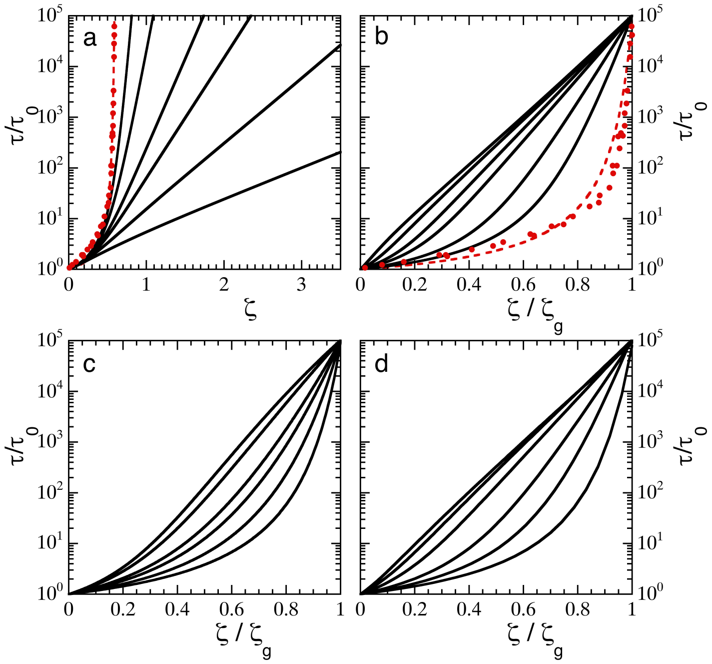

Figure 6.2: a) Structural relaxation time τ, normalised to the Brownian time scale τ_0, as a function of extrapolated particle packing fraction ζ for (solid lines, top to bottom) $\bar{k} = 20$, 10, 5, 3.5, 2 and 1 Pa, with $a_0 = 50$ nm, using Eq.6.7. Symbols: experimental data for colloidal hard spheres from [11] fitted to the VFT equation as described in the text (dotted line). b) Same data as in a) in the so-called Angell representation where the packing fraction is normalised to the glass transition ζ_g. c) Angell plot for theoretical predictions using the harmonic approximation for Π_{in} (Eq.6.11) for $\kappa = 350, 400, 500, 600, 1000$ and 5000 J/m^2. d) Angell plot for theoretical predictions using the Flory-Rehner equation of state (Eq.6.12) for $N_x = 100, 500, 1000, 2000, 3000$ and 4000.

which the system becomes non-ergodic. According to extensive light scattering experiments on colloidal hard spheres [11], the point of ergodicity breaking lies above the MCT glass transition $\phi_c > \phi_g$. For the purposes of this manuscript, we parameterise the VFT law by fitting it to experimental data for hard spheres ($\bar{k} \approx \infty$) as reported by Brambilla *et al.* [11] (symbols Fig.6.2); these experimental data are well fitted by $C = 0.7$ and

$\phi_c = 0.625$ (dotted line Fig.6.2).

Having expressions for both $\tau(\phi)$ and $\phi(\zeta)$, we can now explore how suspensions of compressible colloids vitrify by reconstructing $\tau(\zeta)$, which is typically measured in experiments. Our simple model qualitatively reproduces the results observed experimentally for microgel colloids[13], where τ/τ_0 grows more slowly for softer particles, and extrapolated packing fractions of well over unity are required to reach the glassy state (Fig.6.2a).

To evaluate the fragility of these predicted glass transitions, we first define the glass transition as the packing fraction where $\tau/\tau_0 \equiv 10^5$, following Mattsson *et al.* [13]. For the hard sphere data of Brambilla *et al.* [11], this yields $\phi_g \approx 0.59$, in agreement with MCT predictions and experimental findings[10, 2]. Having defined ϕ_g we can replot our predictions in the Angell representation [12, 38], where the relaxation time is plotted as a function of the rescaled packing fraction ζ/ζ_g; indeed our model reproduces the experimentally observed fragility transition[13] with decreasing $\bar{k}$ (Fig.6.2b).

One may wonder if the observed fragility change as a function of particle softness is a robust feature of any system which exhibits osmotic regulation, many of which will have a different form of their internal or external equation-of-state as compared to the choices above. For example, we can argue that close to their equilibrium size a_0, for small degrees of deswelling $a/a_0 \approx 1$, the free energy of a single compressible particle may be considered to be parabolic: $\Delta G = \kappa(a - a_0)^2$, in which κ is the spring constant, a related measure for the particle softness as compared to k, but with different dimensions. Since $\Pi_{in} = -d\Delta G/dV$ and the particle volume $V = \frac{4}{3}\pi a^3$, we have:

$$\Pi_{in} = \frac{-3d\Delta G}{4\pi a^2 da} = \frac{-3\kappa(a - a_0)}{2\pi a^2} \tag{6.11}$$

Also for this form of the internal pressure, using the Speedy equation-of-state for the bath, we can predict how the relaxation time grows with ζ. We solve these equations numerically, and find that also for this different shape of the internal equation-of-state, a fragile-to-strong transition emerges upon changing the spring constant κ (Fig.6.2c). This highlights how the conceptual idea that osmotic equilibrium governs the fragility of the colloidal glass transition is not sensitive to the exact choice for the internal pressure. It is interesting to note that the "strong" limit of our model does not produce a true Arrhenius curve, since some curvature remains at low values of ζ where the efects of osmotic regulation are weak and the inherent curvature in $\tau(\phi)$ of the VFT equation remains. Thus, the analogy with Arrhenius behavior is only an apparent one and not truly reflective of a pure exponential decay of relaxation rates with ζ/ζ_g.

For certain specific soft sphere systems, more precise and microscopic descriptions of the internal equation-of-state exist. One particular example is the Flory-Rehner swelling theory that describes the internal pressure of uncharged microgel particles as a balance between a mixing term to promote swelling and the entropic elasticity of the polymer segments between crosslinks that counteracts swelling. Within this framework the internal equation of state can be written as [39]:

$$\Pi_{in} = \frac{k_B T}{l_k^3}\left(\left[\phi_p + \ln(1-\phi_p) + \chi\phi_p^2\right] - \frac{\phi_{p,c}}{N_x}\left[\frac{\phi_p}{\phi_{p,c}} - \left(\frac{\phi_p}{\phi_{p,c}}\right)^{1/3}\right]\right) \tag{6.12}$$

which is governed by microscopic properties such as the monomer dimension l_k and the solvent-polymer interaction parameter χ and the polymer volume fraction of the collapsed particle $\phi_{p,c}$ where the elastic contribution to the internal pressure vanishes. Softness is controlled by the crosslinking density, which determines the number of monomer repeat units between crosslinks N_x, which is thus an inverse softness parameter within this model.

Aiming to describe for example pNIPAM microgels, we choose $l_k = 1$ nm, $\phi_{p,c} = 0.5$ and good solvency such that $\chi = 0$. Indeed, also for this microscopic internal equation-of-state, an apparent fragility transition emerges upon changing the crosslinking density N_x (Fig.6.2d). We note that the values of N_x required to induce fragility changes are somewhat higher than those expected in experiments [13]; we attribute this to the fact that we assume a hard-sphere equation of state for the bath, while these experiments worked with partially charged microgels, in which the bath pressure rises much more steeply thus resulting in effectively softer particles, as discussed in more detail below. Finally, we observe that the exact line shape of τ *versus* ζ/ζ_g differs depending on the choice of the internal equation of state. This may hold the promise of deducing the internal equation-of-state of compressible particles from high-resolution measurements of the structural relaxation time and to quantify their softness directly.

To further validate the predictions of our model, we collect published data for particle self-diffusion in a variety of systems composed of compressible spherical objects, ranging from microgels of different softness [13, 40], star polymers [37] and globular proteins [41] (symbols in Fig.6.3). While the microscopic mechanisms with which osmotic equilibrium is regulated differ between these systems, as does the exact form of the equation-of-state, we fit all these data with the analytical form of our model (Eq.6.5-6.7). Since a_0 is known from the experiments this leaves $\bar{k}$ as the only adjustable parameter. We note explicitly, that a comparison of the absolute values of $\bar{k}$ are meaningless, since the underlying equations-of-state for these different systems are not the same; hence the value of $\bar{k}$ needed to fit the data is the effective softness of these particles with the Speedy equation-of-state as an internal standard.

Nonetheless, the line shape, and entire range of experimentally observed fragilities in these soft colloidal systems can be qualitatively reproduced with a simple phenomenological model (drawn lines Fig.6.3a). This highlights how fragility transitions in colloidal systems can be the direct result of osmotic regulation of particle size, providing a mechanism of feedback between number density, particle size and thus volume fraction

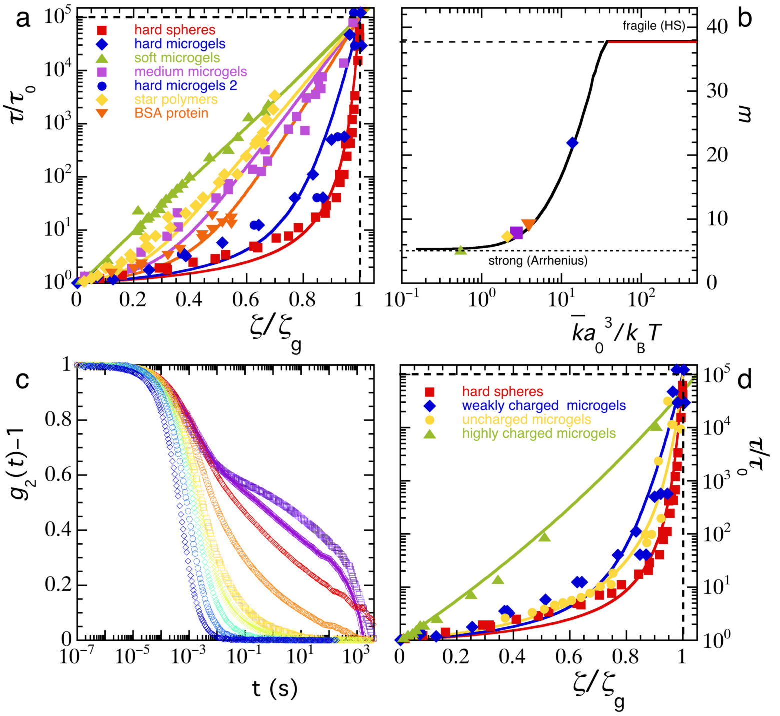

Figure 6.3: a) Angell plot for various systems of compressible spheres, symbols (defined in legend): experimental data for hard spheres ($a_0 \sim 130$ nm) [11], various microgels ($a_0 \sim 90$ nm)[13, 40], star polymers ($a_0 \sim 20$ nm) [37] and the globular protein bovine serum albumin ($a_0 \sim 5$ nm) [41], drawn lines: predictions from the model as outlined in the text with $\bar{k}$ as the adjustable parameter, b) fragility index m as a function of $\bar{k}a_0^3$ as predicted by the model (line) and for the data sets in a) (symbols), c) intensity correlation functions from dynamic light scattering for uncharged polystyrene microgels with (from left to right) $\zeta = 0.64$, 0.88, 1.02, 1.03, 1.19, 1.25, 1.30, 1.35, d) Angell plot for compressible colloids of varying charge density: hard spheres [11], weakly charged microgels [13, 40], uncharged microgels from c), and highly charged microgels [36], drawn lines: predictions from the model.

and the macroscopic structural relaxation time. This provides a theoretical foundation to the idea put forth by Mattsson *et al.* that the fragility changes in microgel suspensions are directly related to local elasticity [13]. Above we have shown how the steepness with which the structural relaxations slow down as the particle concentration is increased are governed by the parameter $\bar{k}a_0^3$. This implies that not only the particle softness, expressed by $\bar{k}$, but also the particle size has an effect on the fragility of the glass. In other words, hard colloids may make strong glasses if the particles are small enough, and soft colloids may make fragile glasses if they are sufficiently large. To make this idea more quantitative, we can compute the kinetic fragility index from the data for $\tau(\zeta)$ as:

$$m = \left.\frac{d\log(\tau/\tau_0)}{d(\zeta/\zeta_g)}\right|_{\zeta=\zeta_g} \tag{6.13}$$

We note that this is an approximation to the kinetic fragility index that is defined as the local slope of the viscosity with temperature in atomic and molecular glass formers. While a more proper analogy would use the pressure rather than packing fraction[42], this is experimentally intractable and beyond the scope of this paper. Thus, to allow for a comparison to experimental data we use the slope of relaxation time *versus* packing fraction as a proxy for the kinetic fragility index of the colloidal glass.

The lower limit of m, for strong glasses that exhibit ideal Arrhenius behavior, is set at m =5, by our definition of the glass transition at $\log(\tau/\tau_0) = 5$. At the other extreme we have the hard sphere glass transition, as the most fragile case of fully incompressible particles, which has $m \approx 37$ based on experimental data [11].

Interestingly, when the elastic energy per particle is $\bar{k}a_0^3 \ll k_BT$, osmotic shrinkage is pronounced, which results in strong glasses, such as for the softest microgels (Fig.6.3b). When $\bar{k}a_0^3$ becomes of the order of the thermal energy, the intrinsic particle elasticity effectively competes with the pressure which develops in the bath, and the transition becomes increasingly fragile until the hard-sphere limit is reached when $\bar{k}a_0^3 \gg k_BT$ (Fig.6.3b). The bulk elastic energy per particle thus acts as an order parameter for the fragility of the colloidal glass transition. Indeed, the experimental data can be collapsed onto the predicted relation between the fragility index m and the normalised particle elasticity when the experimentally-determined fragility is plotted against $\bar{k}a_0/k_BT$, with $\bar{k}$ determined from the fits shown in Fig.6.3a, and a_0 taken from the experimental publications as indicated in the figure caption.

Our phenomenological model does not take the microscopic origins of internal and external pressures into account. For example the Speedy equation-of-state is only valid for particles interacting by volume exclusion alone. Additional contributions, for example due to charges, will affect the osmotic balance both inside the particles and in the bath. This can have significant effects on the phase behavior of soft particle suspensions, *e.g.* leading to the absence of a solid phase in fully ionic microgels even at very high densities[31, 43]. For a comprehensive description of the swelling behavior of ionic microgels which accounts for both polymeric and ionic terms, we refer to Colla *et al.* [44].

To illustrate the effects of charges we start from published experimental data for strongly crosslinked microgels, both for systems that are highly charged [36] and microgels that carry a small amount of charges due to the ionic initiator used during particle synthesis [40, 13]. As no experimental data is available for microgels which carry absolutely zero charges, we synthesize polystyrene microgels using a non-ionic initiator resulting in particles free of ionic groups [45] (see also the Materials & Methods section). These particles are suspended in a mixture of bromo- and iodobenzene which is both a good solvent for the polystyrene gel network and matches their refractive index. We determine the structural relaxation of suspensions of these uncharged microgels with dynamic light scattering (DLS), as a function of ζ, which is determined by capillary viscosimetry in the dilute limit.

With increasing particle concentration, the autocorrelation curves $g_2(t) - 1$ obtained from DLS experiments, show both the slowing down of particle diffusion and the emergence of a plateau at intermediate times, indicative of the formation of repulsive cages which hinder particle motion

(Fig.6.3c). These data are consistent with DLS experiments on aqueous, and slightly charged, microgels [40, 13]. We note that at very long lag times $t > 500$ s, a lack of statistics, due to the experimental aqcuisition time leads to an artifical superexponential decay of the correlation function. Nonetheless, the data clearly show the glass transition as the particle concentration is increased. We do not use the data beyond > 500s to extract the characteristic structural relaxation time such that this does not effect our results. For these uncharged microgels, the glass transition is very fragile and virtually traces the hard sphere line with $m = 37$ (Fig.6.3d). For the weakly charged microgels a small decrease in fragility can be seen, whereas a nearly exponential, Arrhenius, behaviour results for highly charged microgels (Fig.6.3d). This, surprisingly, suggests that a high concentration of charges, which increases the internal osmotic pressure and thus provides additional resistance to deswelling, effectively "softens" the particles by reducing the effective value of $\bar{k}a_0^3$ required to describe the vitrification with our phenomenological model (lines Fig.6.3d).

The counter-intuitive observation that charged microgels act "softer" than uncharged particles at the same crosslinking density, is in agreement with the observation that the osmotic deswelling of ionic microgels can be so severe that the volume fraction at which a liquid-solid transition must occur is not reached, even at exceedingly high values of the extrapolated packing fraction $\zeta > 35$ [31, 43]. This emergent softness was attributed to the high osmotic pressure of the bath, governed by mobile ions unbound to the microgel particles[46], which result in strong compression of the particles as the solid-liquid transition is approached. This argument, and its experimental proof [31], underpins the concept we have raised above, that rather than particle softness alone, as hypothesized previously [13], it is in fact the balance between the osmotic pressure of the bath and the intrinsic softness of the particle that governs the solid-liquid transition and its fragility. Even when the single-particle mechanics indicate a relatively high bulk modulus, if the bath osmotic pressure is high enough, for example due to the presence of ions or for sufficiently small particles, osmotic deswelling may be significant, resulting in a strong rather than a fragile glass. The unusually strong deswelling of ionic microgels furthermore leads to unexpected behavior, such as the strong shrinkage of large microgels in a crystal of smaller particles to accomodate to the lattice and minimize the energy penalty associated with defect formation[47, 48].

6.4 Conclusion

We have presented a simple model, based on the osmotic deswelling of compressible colloids, which qualitatively captures fragility changes observed in colloidal glasses. The change from a fragile to a strong glass transition can be explained by a non-linear relation between the experimental control parameter ζ and the real particle volume fraction which dictates the dynamics of the suspension. The degree of non-linearity depends only on the elastic energy per particle, which thus serves as an effective order parameter for fragility. As the elastic energy per particle scales inversely with particle volume, hard colloids may make strong glasses and soft colloids may make fragile glasses depending on nominal particle size, the particle softness and the equation-of-state of the bath. While the phenomenological description we present provides new insight into the nature of the colloidal glass transition at the macroscopic scale, it does not yet account for spatial heterogeneity at microscopic length scales. Experiments and simulations have shown that softness reduces both the magnitude and spatial extent of dynamical heterogeneities [49] and extends the validity range of the Stokes-Einstein relation to higher packing densities [50, 51]. Perhaps this can be explained by the weaker dependence of relaxation time on local density for softer particles due to osmotic regulation. Extending the simple model proposed here to account for such local effects could aid in elucidating the intriguing connection between glass fragility and dynamical heterogeneity[52, 53, 54].

6.5 Materials & Methods

We prepared stricktly uncharged microgels using a method described in detail elsewhere [45]. Briefly, we dissolved 2 g sodium dodecyl sulfate in 320 ml deionized water in a round bottom flask. Seperately, we prepared a solution of 96 g styrene, 6 g of the crosslinker divinylbenzene, 5 ml hexadecane and 1 g of the radical initiator 2,2-azobis(2-methylpropionitrile). We mix the aqueous and monomer phase and first created a coarse pre-emulsion by using a high-shear rotor-stator mixer. We subsequently formed a stable mini-emulsion using high-intensity ultrasonication. After purging the reaction flask with nitrogen, we allowed the mixture to react overnight at 65°C. The microgel particles were purified by precipitation in cold methanol, filtration and drying in vacuo, followed by resuspension in THF and precipitation in methanol. This is repeated 3x to ensure complete removal of surfactant and reaction byproducts. Finally we resuspend the microgels in THF to swell the microgels completely, which allows any linear polystyrene to diffuse out of the microgels, which we remove by centrifugation at 30000 g and removal of the supernatant. This was repeated three times to ensure complete removal of all linear polystyrene as confirmed by gel permeation chromatography. We then dried the microgels in vacuo. The resulting particles have a hydrodynamic radius in the dilute limit of $a_0 = 93$ nm, measured in the index-matching solvent.

Samples are prepared by suspending a known weight of dried microgels in an index-matching mixture of iodobenze and bromobenzene (70:30 by volume). Samples are mixed extensively by vortexing and repeated centrifugation for the most viscous samples; in all cases, the sample was centrifuged at 1500 g in the sample tube prior to measurement to remove any air bubbles and dust from the scattering volume. Samples were equilibrated for at least 1 hour in the thermostated sample bath at 21°C to ensure a homogeneous temperature within the sample. Measurements were performed using a dynamic light scattering (DLS) setup based on an ALV/CGS-3 goniometer, equipped with an avalanche photon detector, 633 nm diode laser (JDSU) and dual ALV LSE-5004 hardware correlators for cross-correlation. All measurements were performed at a scattering angle of $150°$, which gives a scattering vector $q = \frac{4\pi}{\lambda} sin\frac{\theta}{2} = 0.02~\mathrm{nm}^{-1}$. We note that to measure true self-diffusion, measurements should be performed at scattering vectors $qa \leq 2\pi$, with a the particle radius. For the polystyrene microgels we study here, this implies a minimum scattering vector of $q = \frac{2\pi}{a} \approx 0.07~\mathrm{nm}^{-1}$ which is not attainable in this set-up. Since our scattering vector was below this value, we probed dynamics on somewhat larger characteristic length scales, which we took as a measure of the sample's viscosity or long-time particle self-diffusivity.

References

[1] Pusey, P. N. Colloidal Suspensions. In Hansen, J. P., Levesque, D. & Zinn-Justin, J. (eds.) *Liquids, Freezing and the Glass Transition*, 765–942 (Elsevier, Amsterdam, 1991).

[2] Hunter, G. L. & Weeks, E. R. The Physics of the Colloidal Glass Transition. *Rep. Prog. Phys.* **75**, 66501 (2012).

[3] Kegel, W. K., van Blaaderen & Alfons. Direct Observation of Dynamical Heterogeneities in Colloidal Hard-Sphere Suspensions. *Science* **287**, 290 – 293 (2000).

[4] van de Laar, T., Higler, R., Schroën, K. & Sprakel, J. Discontinuous Nature of the Repulsive-to-Attractive Colloidal Glass Transition. *Sci. Rep.* **6**, 22725 (2016).

[5] Weeks, E., Crocker, J., Levitt, A., Schofield, A. & Weitz, D. A. Three-Dimensional Direct Imaging of Structural Relaxation Near the Colloidal Glass Transition. *Science* **287**, 627–631 (2000).

[6] Malins, A., Eggers, J., Royall, C. P., Williams, S. R. & Tanaka, H. Identification of Long-Lived Clusters and Their Link to Slow Dynamics in a Model Glass Former. *J. Chem. Phys.* **138**, 12A535 (2013).

[7] Patrick Royall, C., Williams, S. R., Ohtsuka, T. & Tanaka, H. Direct Observation of a Local Structural Mechanism for Dynamic Arrest. *Nat. Mater* **7**, 556–561 (2008).

[8] Laurati, M., Maßhoff, P., Mutch, K. J., Egelhaaf, S. U. & Zaccone, A. Long-Lived Neighbors Determine the Rheological Response of Glasses. *Phys. Rev. Lett.* **118**, 18002 (2017).

[9] Conrad, J. C., Dhillon, P. P., Weeks, E. R., Reichman, D. R. & Weitz, D. A. Contri-

bution of Slow Clusters to the Bulk Elasticity Near the Colloidal Glass Transition. *Phys. Rev. Lett.* **97**, 265701 (2006).

[10] Götze, W. Recent Tests of the Mode-Coupling Theory for Glassy Dynamics. *J. Phys.: Condens. Matter* **11**, A1 (1999).

[11] Brambilla, G. *et al.* Probing the Equilibrium Dynamics of Colloidal Hard Spheres Above the Mode-Coupling Glass Transition. *Phys. Rev. Lett.* **102**, 85703 (2009).

[12] Angell, C. A. Formation of Glasses from Liquids and Biopolymers. *Science* **267**, 1924–1935 (1995).

[13] Mattsson, J. *et al.* Soft Colloids Make Strong Glasses. *Nature* **462**, 83–86 (2009).

[14] Liu, Y. H. *et al.* Characterization of Nanoscale Mechanical Heterogeneity in a Metallic Glass by Dynamic Force Microscopy. *Phys. Rev. Lett.* **106**, 125504 (2011).

[15] McKenna, G. B., Narita, T. & Lequeux, F. Soft Colloidal Matter: A Phenomenological Comparison of the Aging and Mechanical Responses With Those of Molecular Glasses. *J. Rheol.* **53**, 489–516 (2009).

[16] Mayer, C. *et al.* Asymmetric Caging in Soft Colloidal Mixtures. *Nat. Mater* 7, 780–784 (2008).

[17] Roovers, D. V., Fytas, G., Pakula, T. & Jacques. Multiarm Star Polymers Dynamics. *J. Phys.: Condens. Matter* **13**, R855 (2001).

[18] Vitkup, D., Ringe, D., Petsko, G. A. & Karplus, M. Solvent Mobility and the Protein 'Glass' Transition. *Nat. Struct. Mol. Biol.* 7, 34–38 (2000).

[19] Lee, A. L. & Wand, A. J. Microscopic Origins of Entropy, Heat Capacity and the Glass Transition in Proteins. *Nature* **411**, 501–504 (2001).

[20] Zhou, E. H. *et al.* Universal Behavior of the Osmotically Compressed Cell and its Analogy to the Colloidal Glass Transition. *Proc. Natl. Acad. Sci.* **106**, 10632–10637 (2009).

[21] Angelini, T. E. *et al.* Glass-like Dynamics of Collective Cell Migration. *Proc. Natl. Acad. Sci.* **108**, 4714–4719 (2011).

[22] Krausser, J., Samwer, K. H. & Zaccone, A. Interatomic Repulsion Softness Directly Controls the Fragility of Supercooled Metallic Melts. *Proc. Natl. Acad. Sci.* **112**, 13762–13767 (2015).

[23] Zaccone, A. E. L., Krausser, J., Evenson, Z., Samwer, K. & A. Unifying Interatomic Potential, g (r), Elasticity, Viscosity, and Fragility of Metallic Glasses: Analytical model, Simulations, and Experiments. *J. Stat. Mech.: Theory Exp.* **2016**, 84001 (2016).

[24] Fernández-Nieves, A., Fernández-Barbero, A., Vincent, B. & de las Nieves, F. J. Osmotic De-Swelling of Ionic Microgel Particles. *J. Chem. Phys.* **119**, 10383–10388 (2003).

[25] Saunders, B. R. & Vincent, B. Osmotic De-Swelling of Polystyrene Microgel

Particles. *Colloid Polym. Sci.* **275**, 9–17 (1997).

[26] Saunders, B. R., Crowther, H. M. & Vincent, B. Poly[(methyl methacrylate)-co-(methacrylic acid)] Microgel Particles: Swelling Control Using pH, Cononsolvency, and Osmotic Deswelling. *Macromolecules* **30**, 482–487 (1997).

[27] Evans, I. D. & Lips, A. Concentration Dependence of the Linear Elastic Behaviour of Model Microgel Dispersions. *J. Chem. Soc., Faraday Trans.* **86**, 3413–3417 (1990).

[28] Hashmi, S. M. & Dufresne, E. R. Mechanical Properties of Individual Microgel Particles Through the Deswelling Transition. *Soft Matter* **5**, 3682–3688 (2009).

[29] Riest, J., Athanasopoulou, L., Egorov, S. A., Likos, C. N. & Ziherl, P. Elasticity of Polymeric Nanocolloidal Particles. *Sci. Rep.* **5**, 15854 (2015).

[30] Pellet, C. & Cloitre, M. The glass and jamming transitions of soft polyelectrolyte microgel suspensions. *Soft matter* **12**, 3710–3720 (2016).

[31] Pelaez-Fernandez, M., Souslov, A., Lyon, L. A., Goldbart, P. M. & Fernandez-Nieves, A. Impact of Single-Particle Compressibility on the Fluid-Solid Phase Transition for Ionic Microgel Suspensions. *Phys. Rev. Lett.* **114**, 98303 (2015).

[32] Flory, P. J. & Rehner, J. Statistical Mechanics of Cross-Linked Polymer Networks II. Swelling. *J. Chem. Phys.* **11** (1943).

[33] Flory, P. J. *Principles of Polymer Chemistry: Paul J. Flory*. The George Fisher Baker Non-Resident Lectureship in Chemistry At Cornell University (Cornell University, 1953).

[34] Speedy, R. J. The Equation of State for the Hard Sphere Fluid at High Density. The Glass Transition. *Physica B+C* **121**, 153–161 (1983).

[35] Li, Y., Hu, Z. & Li, C. New Method for Measuring Poisson's Ratio in Polymer Gels. *J. Appl. Polym. Sci.* **50**, 1107–1111 (1993).

[36] Romeo, G., Imperiali, L., Kim, J.-W., Fernández-Nieves, A. & Weitz, D. A. Origin of De-Swelling and Dynamics of Dense Ionic Microgel Suspensions. *J. Chem. Phys.* **136**, 124905 (2012).

[37] Fleischer, G., Fytas, G., Vlassopoulos, D., Roovers, J. & Hadjichristidis, N. Self-Diffusion of Multiarm Star Polymers in Solution Far From and Near the Ordering Transition. *Phys. A* **280**, 266–278 (2000).

[38] Angell, C. A. The Old Problems of Glass and the Glass Transition, and the Many New Twists. *Proc. Natl. Acad. Sci.* **92**, 6675–6682 (1995).

[39] Voudouris, P., Florea, D., van der Schoot, P. & Wyss, H. M. Micromechanics of temperature sensitive microgels: Dip in the poisson ratio near the lcst. *Soft Matter* **9**, 7158–7166 (2013).

[40] Kasper, A., Bartsch, E. & Sillescu, H. Self-Diffusion in Concentrated Colloid Suspensions Studied By Digital Video Microscopy of Core-Shell Tracer Particles. *Langmuir* **14**, 5004–5010 (1998).

[41] Roosen-Runge, F. *et al.* Protein Self-Diffusion in Crowded Solutions. *Proc. Natl. Acad. Sci.* **108**, 11815–11820 (2011).

[42] Berthier, L. & Witten, T. A. Glass transition of dense fluids of hard and compressible spheres. *Phys. Rev. E* **80**, 021502 (2009).

[43] Sierra-Martin, B. & Fernandez-Nieves, A. Phase and Non-Equilibrium Behaviour of Microgel Suspensions as a Function of Particle Stiffness. *Soft Matter* **8**, 4141–4150 (2012).

[44] Colla, T., Likos, C. N. & Levin, Y. Equilibrium properties of charged microgels: A poisson-boltzmann-flory approach. *J. Chem. Phys.* **141**, 234902 (2014).

[45] Antonietti, M., Pakula, T. & Bremser, W. Rheology of Small Spherical Polystyrene Microgels: A Direct Proof for a New Transport Mechanism in Bulk Polymers besides Reptation. *Macromolecules* **28**, 4227–4233 (1995).

[46] Levin, Y., Diehl, A., Fernández-Nieves, A. & Fernández-Barbero, A. Thermodynamics of Ionic Microgels. *Phys. Rev. E* **65**, 36143 (2002).

[47] Scotti, A. *et al.* The Role of Ions in the Self-Healing Behavior of Soft Particle Suspensions. *Proc. Natl. Acad. Sci.* **113**, 5576–5581 (2016).

[48] Iyer, A. S. & Lyon, L. Self-Healing Colloidal Crystals. *Angew. Chem., Int. Ed.* **48**, 4562–4566 (2009).

[49] Rahmani, Y. *et al.* Dynamic Heterogeneity in Hard and Soft Sphere Colloidal Glasses. *Soft Matter* **8**, 4264–4270 (2012).

[50] Ikeda, A. & Miyazaki, K. Glass transition of the monodisperse gaussian core model. *Phys. Rev. Lett.* **106**, 015701 (2011).

[51] Gupta, S. *et al.* Validity of the stokes-einstein relation in soft colloids up to the glass transition. *Phys. Rev. Lett.* **115**, 128302 (2015).

[52] Debenedetti, P. G. & Stillinger, F. H. Supercooled Liquids and the Glass Transition. *Nature* **410**, 259–267 (2001).

[53] Kanaya, T., Tsukushi, I., Kaji, K., Gabrys, B. & Bennington, S. M. Heterogeneity of Amorphous Polymers With Various Fragility Indices as Studied in Terms of Non-Gaussian Parameter. *J. Non-Cryst. Solids* **235–237**, 212–218 (1998).

[54] Starr, F. W., Douglas, J. F. & Sastry, S. The Relationship of Dynamical Heterogeneity to the Adam-Gibbs and Random First-Order Transition Theories of Glass Formation. *J. Chem. Phys.* **138**, 12A541 (2013).

Chapter 7

Two-dimensional crystals of star polymers: a tale of tails

The formation of non-hexagonal crystalline structures by the organisation of colloidal nanoparticles often involves the use of complex particles with anisotropic shape or interactions or the imposition of non-uniform external fields. Here we explore how unusual symmetries can be created using experimentally realistic particles that interact through isotropic and purely repulsive potentials. In particular, we use simulations to explore the phase behavior of two-dimensional systems of star polymers. We uncover how the tail of the pair potential has a large role in dictating the phase behavior. Star polymers interacting in the far field with a Gaussian potential only form hexagonal phases, while an exponential tail gives rise to stable primitive oblique and honeycomb lattices. We identify the ratio in strength between long and short range interactions and the nature of the transition between these regimes as crucial parameters to predict when non-hexagonal crystals of star polymers can be stable. This leads to experimental design rules for creating star polymers which should exhibit unusual lattice formation.

This chapter was published as:

I. Bos , P. van der Scheer, W. G. Ellenbroek and J. Sprakel: *Deswelling and Deformation of Microgels in Concentrated Packings,* Soft Matter, 2019,15, 615-622

7.1 Introduction

The self-organisation of colloids and nanoparticles into ordered two-dimensional lattices offers the potential for the creation of new electronic and photonic metamaterials [1, 2, 3, 4, 5]. The symmetry of the two-dimensional lattice, which governs the transport of electrons or photons through the structure, is dictated by the interactions between the particulate building blocks. For particles interaction through relatively 'simple' isotropic repulsive interactions, such as hard sphere-like or exponential potentials, a hexagonal crystal is found to be the only stable solid phase [6, 7, 8, 9]. Obtaining non-hexagonal crystal symmetries requires tailoring of the pair interactions. For example, breaking the isotropic symmetry of the interaction forces can result in stable non-hexagonal crystal monolayers; this can be achieved in a variety of ways, for example by introducing shape anisotropy[10], chemically-reactive facets[3], a patchy particle surface[11], directional attractions mediated by supramolecular motifs [12], the use of bidisperse particle populations [13] or the imposition of non-uniform fields [14].

In the past decade, extensive computer simulations have revealed that a plethora of non-hexagonal crystals and quasicrystals can also be formed by particles that interact through isotropic potentials. For example, square lattices can be stable in systems with a square softened single well [15], whereas a double well leads to the formation of decagonal and dodecagonal two-dimensional quasicrystals[16]. More complex and designed potentials featuring multiple attractive minima and repulsive regions, can give rise to the sought-after honeycomb lattice [17], which exhibits unique electronic and photonic properties [3, 18]. Even with purely repulsive and isotropic potentials, non-hexagonal crystals have been predicted to occur. For example, introducing an inflection point in a core-softened repulsive potential can lead to string-like and Kagome phases[19].

It appears that the presence of two distinct length scales and interactions beyond a first nearest-neighbor shell are crucial to stabilise many of these uncommon crystals and quasicrystals [20, 21]. A well-studied example is the repulsive hard-core/square-shoulder potential. This potential is used as a simplified description of the interactions between particles with a hard and impenetrable core decorated with a soft corona. By varying the size and softness ratio of hard core and soft corona a variety of two-dimensional lattices can theoretically be obtained [22, 20, 23]. Also for elastic spheres that interact by means of bounded Hertzian potentials a rich phase behavior has been predicted, including square, honeycomb, Kagome and snub square tilings[24], despite the fact that these potentials only have one length scale.

Despite the overwhelming choice of potentials to create non-hexagonal two-dimensional crystals in computer simulations, most of these potentials are impossible to create experimentally, given only a few exceptions[23, 24]. To make the translation from the in-silico results to systems that could be achieved in experiments, it is necessary to explore what realistic potentials can yield the same rich phase behavior in order to establish experimental design rules. Moreover, if the stability of the crystalline phase depends very sensitively on the exact shape of the potential, its success in experiments will be largely hampered by the inherent dispersity in the particle size, shape, conformation and softness during particle synthesis. Finding experimentally-realistic, isotropic and purely-repulsive potentials capable of stabilising non-hexagonal two-dimensional lattices in a robust manner thus remains an open challenge.

In this paper, we attempt to further bridge the gap between simulations and experiments in the quest for self-organised particle-based metamaterials. We explore the phase behavior of two-dimensional systems of star polymers anchored to a planar interface, parameterised by previously developed potentials for surface-adsorbed star polymers [25]. In three dimensions, star polymers and star-like micelles are known to exhibit a rich phase behavior, exhibiting body-centered orthogonal and diamond crystal structures [26, 27, 28, 29, 30, 31, 32]. Experiments have even revealed a stable quasicrystalline phase [21]. Here we explore if these same star polymer particles can be used for the creation of non-hexagonal crystalline lattices in two dimensions. In particular, we explore the effect of the weak and long-ranged tail of the interactions, which we show to have a drastic effect on the phase behavior and the stability of non-hexagonal phases.

Both for the two- and three-dimensional case, the short-ranged interactions between star polymer cores can be analytically derived, whereas the exact shape of interactions at longer distances, beyond the diameter of the star, remains unknown. In some cases, the tail of the pair potential is presumed to have a Gaussian shape [25, 28], based on the idea that the interaction between dilute polymer chains that protrude from the star is ideal. In other cases, the tail of the potential is presumed to decay exponentially, in the form of a Yukawa potential, with a decay length set by the blob size at the periphery of the star-shaped polymer[26, 27], depending on the number of arms and the effective star diameter [33]. Molecular dynamics simulations are inconclusive as to the appropriate form for the interaction tail; whereas some confirm the Yukawa tail [27], other studies find support for the Gaussian shape of the long-ranged forces[28].

Here we show how the shape of the tail has a drastic effect on the phase behavior; while only hexagonal crystals are stable for Gaussian tails, a much richer phase behavior with multiple crystalline states is found for the exponential tail. Moreover, we also explore what happens if we assume there is no long-ranged tail in the star-star interactions. Our results shed light on the importance of the tail in the interaction potential for the realisation of non-hexagonal two-dimensional solids and provides clues how these structures can be realised experimentally.

7.2 Methods

Since the phase behavior of three-dimensional star polymer solutions is well studied[26, 27, 28, 29, 30, 31, 32], we choose a form of the two-dimensional potential for star polymers that matches the three-dimensional formulation more closely. As compared to the original Gaussian-tail potential for adsorbed star polmers [25], we choose the star diameter σ as the separation distance where the transition between the short-range and long-range sections of the interactions occur, in accord with the formulation for three-dimensional stars. In addition, we have shifted the potential and adjusted the prefactor of the tail interaction to ensure its derivative is continuous at the transition point $r = \sigma$:

$$\frac{V(r)}{k_B T} = \frac{2 + 9f^2}{24} \begin{cases} -\ln(r/\sigma) + \frac{1}{2}, & r \leq \sigma \\ \frac{1}{2} \exp\left[1 - (r/\sigma)^2\right], & r > \sigma \end{cases} \tag{7.1}$$

Here, r is the centre-to-centre distance between the stars and f its number of arms.

To construct a two-dimensional star potential with an exponential tail, we use the outer blob diameter as the characteristic decay length in a Yukawa potential. The potential, again shifted and adjusted to ensure continuity in force at $r = \sigma$, reads:

$$\frac{V(r)}{k_B T} = \frac{2 + 9f^2}{24} \begin{cases} -\ln(r/\sigma) + \frac{\pi}{\pi + f}, & r \leq \sigma \\ \frac{\pi}{\pi + f} \frac{\sigma}{r} \exp\left[-\frac{f}{\pi}(r/\sigma - 1)\right], & r > \sigma \end{cases} \tag{7.2}$$

Finally, we also explore a potential in which the star polymers do not interact at separation distances beyond their diameter, thus assuming the absence of chains that protrude beyond σ. In this case, the force is discontinuous at the star boundary:

$$\frac{V(r)}{k_B T} = \frac{2+9f^2}{24} \begin{cases} -\ln(r/\sigma), & r \leq \sigma \\ 0, & r > \sigma \end{cases} \tag{7.3}$$

We perform Monte Carlo (MC) simulations in the canonical ensemble by placing $N = 400$ stars in a square periodic box of length L. The area fraction η is defined as $\eta = N\pi\sigma^2/(4L^2)$. We initialise the simulation with a low density fluid configuration, which is compressed to the desired area fraction after which the structure is equilibrated. To construct the ground state diagram, we slowly quench the simulations until a zero-temperature configuration was found. For low arm numbers, $f = 6$ and $f = 8$, on occasion we observed quenched structures that differed strongly from the surrounding ground states. In these cases, we computed the lattice sum of the interaction energy of the observed and surrounding symmetries to find the lattice of lowest energy, from which the complete ground-state diagram was constructed.

7.3 Results & Discussion

The exact functional form of the tail of the interactions between adsorbed star polymers, confined to a two-dimensional interface, remains unclear; whereas some studies predict a Gaussian shape of the interactions between dangling chains that extend beyond the average star diameter, others have suggested an exponential form is more appropriate [27, 28]. Interestingly, we find that the exact choice has a very strong effect on the observed phase behavior. This could provide clues to the appropriate experimental design of star polymers for the two-dimensional templating of non-hexagonal symmetries in creating novel electronic or photonic materials.

For star polymers interacting beyond their diameter with a Guassian potential, the phase diagram only exhibits a stable solid phase with

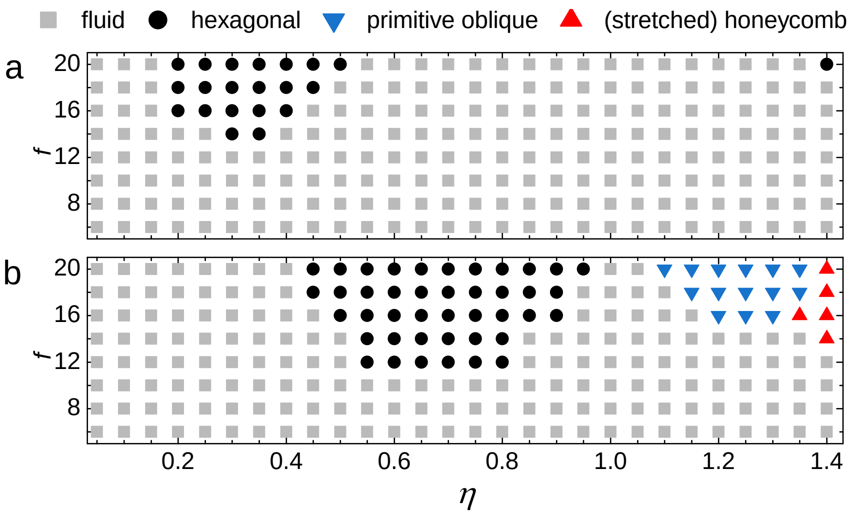

Figure 7.1: Phase diagrams of two-dimensional star polymer systems with a tail interaction of the Gaussian (a) and Yukawa (b) form.

a hexagonal symmetry for $f > 12$ (Fig.7.1). This liquid-solid transition also leads to the emergence of distinct Bragg peaks in the computed two-dimensional structure factor as shown in Figure 7.2a-b. Interestingly, compressing a stable hexagonal phase of these stars leads to a re-entrance of the fluid phase. The same fluid re-entrance is observed in simulations of particles that interact by means of a Gaussian potential only[34]. By contrast, star polymers with an exponential Yukawa tail in their interaction potential, show, in addition to the hexagonal phase and the re-entrant fluid, two additional non-hexagonal crystal states. At intermediate densities we find a primitive oblique phase, which has a parallellogram-shaped unit cell (Fig.7.2c), and at high packing densities we find the sought-after honeycomb symmetry (Fig.7.1 and Fig.7.2d). Compressing the primitive oblique structure first gives rise to a strained honeycomb (Fig.7.2e), whose strain axis is set by that of the parent primitive oblique lattice, before the symmetric honeycomb lattice is formed at higher densities. In all cases, a minimum arm number of ≈ 12 is required to find ordered solid phases.

Lower arm numbers result in interactions that are too soft to give rise to an distinct liquid-solid transition; this is in direct agreement with theoretical predictions and experimental data for three-dimensional phases of star polymers [26, 27, 28, 29, 30, 31, 32].

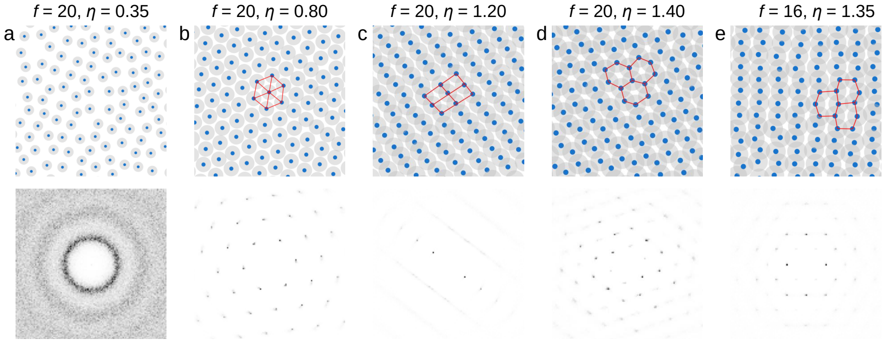

Figure 7.2: Representative examples of two-dimensional phases formed in star polymer systems with a Yukawa tail in their interactions (top) and the corresponding two dimensional structure factors $S(q_x, q_y)$ (bottom). Grey spheres indicate the diameter σ of the star polymers to indicate the degree of star-star interpenetration, while blue dots are drawn for the sake of clarity. Unit cell structures are indicated with red lines. For the calculation of the structure factors with sufficient resolution, we simulated structures with $N = 3600$ for $2 \cdot 10^8$ MC steps.

Clearly, despite the softness of the tail interactions, the exact shape of this tail has a drastic effect on the phase behavior of the two-dimensional system. The transition from fluid to hexagonal solid followed by re-entrant melting, which is observed for stars with a Guassian tail, is typical for purely Gaussian particles. [34] The initial phase behavior of the stars with an exponential tail also corresponds to the behavior known for two-dimensional phases of Yukawa particles[35, 36]. Thus, as expected, at low densities, only the tail of the pair potential is important. The logarithmic interactions of the star polymer core begin to contribute when the stars begin to overlap. Assuming a hexagonal symmetry, star overlap begins to contribute significantly when the packing fraction exceeds the close packing limit for hard spheres $\eta = \pi/(2\sqrt{3}) \approx 0.9$. For both potentials, the stars behave as a fluid from this point, even when they crystallized at lower packing fractions. This re-entrant melting at intermediate densities is a property of certain bounded repulsive potentials whose Fourier transform is positive definite [37]. The logarithmic interaction of the core belongs to this class of potentials, and the re-entrant fluid phase is found both in two (Fig. 7.1) and in three dimensions[32]. This suggests that at intermediate densities the phase behavior of these adsorbed star polymers is determined in part by the core potential. Since the Gaussian potential also belongs to class of bounded repulsive potentials, the re-entrant melting in this case occurs already at lower packing fractions.

Interestingly, the largest difference between the Yukawa and Gaussian-tailed stars occurs at the highest packing fractions, where one might have assumed that only core interactions contribute significantly to the phase behavior. Clearly, even at densities well above the overlap concentration,

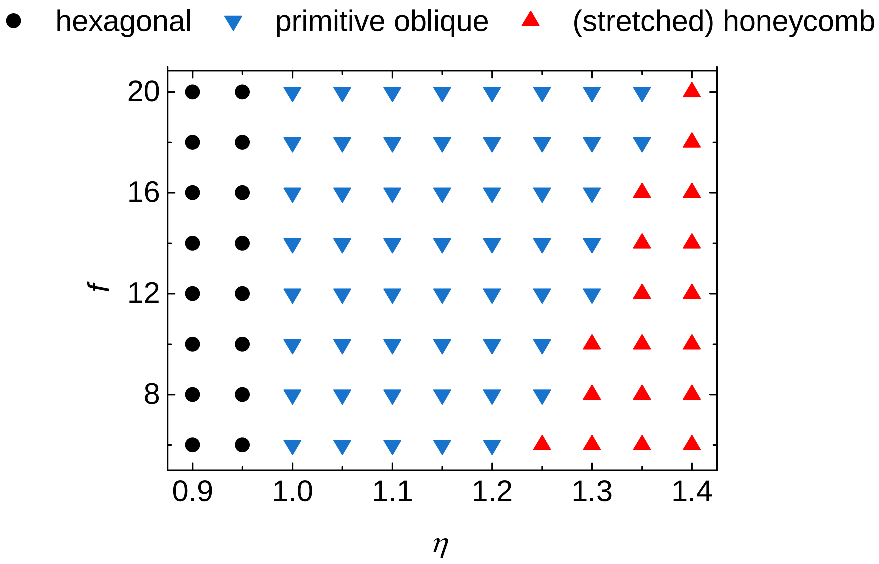

Figure 7.3: Ground state diagram of two-dimensional stars with a Yukawa tail for the long range interactions.

the tail interactions play a significant role in governing the behavior of the two-dimensional system.

To further elucidate these effects, we also determined the ground state diagrams, in which fluid phases and hence the re-entrance are suppressed. Here, we approach the ground state by quenching an equilibrated particle configuration by gradually increasing the interaction strength. Since this may lead to kinetically trapped states, we also computed the total potential energy of the structures we observed using a lattice sum of the interaction energies. However, we cannot rule out that there are other, more exotic structures that we have not observed with a lower overal energy. It is not necessary to quench all the configurations of the finite-temperature phase diagram. At the lowest packing fractions only the Gaussian or Yukawa tail contributes to the ground state symmetry, which have been established to lead to hexagonal solids[34, 38]. Moreover, for the stars with a Gaussian tail, the number of arms f only appears in the prefactor of the potential and thus has no influence on the shape of the potential; as a result, changing the arm number has no effect on the ground state. Thus, for the star potential with a Guassian tail, the entire ground state diagram shows only a hexagonal symmetry. By contrast, for the Yukawa tail, we find stable ground states with the same primitive oblique and honeycomb structures also observed in the phase diagrams (Fig. 7.3).

To explain the difference between the behaviour of stars with a Yukawa versus Gaussian tail, we must understand what occurs at the transition from a hexagonal symmetry to the other crystal structures. At this transition, a few neighbors move in to a closer star-star distance, while others move further away to a separation distance inbetween the original first and second neighbours distances, as can be seen in the distance scaled pair correlation functions (Fig. 7.4a). For a transition away from the high-symmetry hexagonal phase to be favorable, the combination of moving some neighbors closer while increasing the separation with others should result in a net decrease of the potential energy of interaction. In

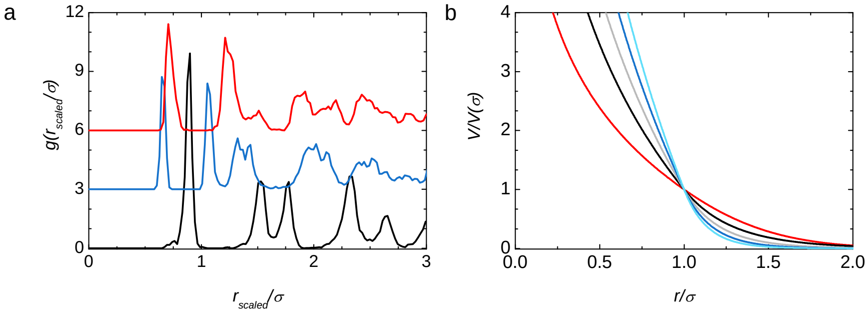

Figure 7.4: (a) Two-dimensional pair correlation functions for a hexagonal (black), primitive oblique (blue) and honeycomb lattice (red) obtained by quenching the configurations of two-dimensional Yukawa stars with $f = 14$ at $\eta = 0.9$, $\eta = 1.2$ and $\eta = 1.4$, respectively. For a direct comparison, the distance axis is scaled to the relative degree of compression, taking $\eta = 1.2$ as the reference state: $r_{scaled} = rL(\eta = 1.2)/L(\eta)$. (b) Interaction potentials normalized to the interaction energy at the transition point $r = \sigma$, for a Gaussian-tailed potential (red) and a Yukawa-tailed potential with $f = 8$ (black), $f = 12$ (grey), $f = 16$ (blue) and $f = 20$ (light blue).

other words, this is most likely to occur when the increase in energy of the new nearest-neighbour is weak while the decrease in energy for moving some neighbors slightly further away significantly reduces their interactions with a central test particle.

To satisfy the first constraint, softness in the potential is a crucial requirement. If the potential increases too steeply upon decreasing r, the energy cost of bringing only a few closer is already larger than the energy of the sum of the energy of the original first row of neighbours in the hexagonal crystal. For star polymers, the short range interaction is logarithmic in form and thus provides the required softness. The second requirement explains why the shape of the tail interactions plays such a large role in governing the phase behavior. Transforming the hexagonal phase to a different symmetry creates a new second row of neighbors at distances $r > \sigma$; these thus interact through the long range regime of the potential. By normalizing these two types of potentials to the energy at the transition $r = \sigma$ (Fig. 7.4b), we observe how the long range interaction is weak for a Yukawa tailed interaction, as compared to the core-core repulsion, especially for larger arm numbers. On the other hand, for stars with a Gaussian tail, the long ranged interaction is relatively strong. Thus, for the Yukawa stars, the energy gain of moving some nearest-neighbors to a second shell significantly reduces the energy; by contrast, for the Gaussian stars this energetic gain is very limited. Since it is this energy gain that balances against the energy cost of the closer contact between the nearest neighbors to determine if lower energy states exist beyond the hexagonal symmetry, this explains why only the exponential tail gives rise to lower symmetry lattices.

These normalized potentials also shed light on the reason that the honeycomb lattice becomes stable at lower densities for stars with fewer arms, as can be seen in the ground state diagram in Fig. 7.3a. Upon transforming from the primitive oblique to the honeycomb lattice, the number of nearest-neighbours increases from 2 to 3 (see Fig. 7.2). Simultaneously, the second row of neighbours move further away, as can be clearly seen when comparing the scaled pair correlation functions (Fig. 7.4). This shows how the mechanisms for the primitive oblique to honeycomb transition lies in the fact that further compression of the primitive phase leads to such a high energy cost for second nearest neighbors, that energy can be gained by adding an additional nearest neighbor allowing the second row to move further away. It is exactly the same mechanism that causes a transition from the body-centered orthogonal to a diamond symmetry in three dimensional star polymer phases[32]. The normalized potentials show how the relative strength of the tail interactions decreases with f, such that the transition occurs at lower packing fractions as f is decreased.

These arguments give us a qualitative explanation for the phase changes we observe in our simulations. To support this line of thought, we can make an analytical lattice sum of the potential energy to compare the ground state energies of hexagonal and honeycomb configurations. We choose the symmetrical $(6)^3$ honeycomb and $(6)^6$ hexagonal symmetries for this comparison as their lattice coordinates are well-defined and subject only to isotropic compression as the density is increased. By contrast, the ratio of side lengths of the less symmetric primitive oblique varies with density such that an analytical comparison is more cumbersome. In our analytical calculation of the lattice energy we sum interactions over the 6 nearest-neighbors for the hexagonal lattice and 3 first nearest- and 6 second-nearest neighbors for the honeycomb, along the lines of our qualitative arguments described above. Interaction energies beyond these neighbors are sufficiently small at relevant densities that they contribute marginally to the ground state energy and are thus ignored for the purposes of this comparison. At a given packing fraction, the first nearest-neighbor distances for the hexagonal and honeycomb lattice follow from the lattice geometry (Fig. 7.5) as $r_{hex} = \sigma\sqrt{\phi_{hex}/\eta}$ and $r_{hc} = \sigma\sqrt{\phi_{hc}/\eta} = \sqrt{2/3}r_{hex}$, with ϕ_{hex} and ϕ_{hc} the maximum hard-sphere packing fractions of the two lattices, respectively, and the second nearest-neighbour distance for the honeycomb pattern is $r_{hc2} = \sqrt{3}r_{hc}$.

This analytical calculation echoes the findings in our simulation that the Guassian-tailed stars can only form hexagonal solids, as the ratio of lattice energies of the honeycomb $V_{hc,tot}$ to that for the hexagonal lattice at equal density $V_{hex,tot}$ never goes below unity irrespective of density of arm number f (Fig.7.5). Indeed, for the exponential tail, the honeycomb lattice gains a lower energy than the hexagonal phase, giving rise to a hexagonal-to-honeycomb transformation. In reality, this transition occurs through the primitive oblique phase as an intermediary, which continuously transforms into a stretched honeycomb until the symmetrical honeycomb becomes stable. We note however that the phase boundary predicted analytically is not exactly matched with what we observe in the simulations. According to the analytical description, for $f = 8$ the hexagonal patterns are always favored as the energy ratio remains

> 1, while the simulated ground state diagram shows a stable honeycomb phase for $f = 8$ and even for $f = 6$. Apparently, taking into account the interactions up to only the second-nearest neighbor shell cannot capture the behavior exactly. In experimental realisations of this system however, one can wonder how relevant such long ranged interactions are, since this would require the stars to interpenetrate to such an extent that chains extend to well beyond the first row. Obviously, also non-additive effects that are ignored in these simulations and calculations may come into play at these densities in real star polymer phases [39].

Clearly, the exact shape of the tail of the interactions has tremendous effects on the phase behavior of two-dimensional star polymer phases. This raises the question what would occur if we shift and truncate the interaction potential at the star diameter such that there is no tail interaction $V = 0$ for $r > \sigma$. We find that particles interacting *via* this potential form very unusual and low symmetry structures in the overlap regime (Fig. 7.6b), which we can understand by inspecting the pair correlation function. These structures represent the packings in which the fewest number of particles have $r < \sigma$, thereby minimizing the potential energy. To still accomodate for significant packing fractions, this is achieved by placing as many particles possible at a distance of exactly $r = \sigma$, as this is the closest packing that is energetically cost-free. Therefore, the largest peak in the pair correlation function is at $r = \sigma$ for all densities above a certain threshold. This strong effect of the truncation point was not observed for Hertz potentials,[24] which also show now interactions for $r > \sigma$. However, for the Hertzian case, the force is continuous at $r = \sigma$, while this is not possible for the logarithmic form of the star polymer potential. Even this subtle effect of continuity versus discontinuity in the force at the transition point has a large effect on the phase behavior. While Hertzian spheres exhibit a variety of ordered structures, the truncated star potential behaves hard-sphere like up to a critical density beyond which we find the unusual phases with a large number of particles position at exactly $r = \sigma$. In experimental system a discontinuity is not likely to occur since the transition between core and corona is not a sharp wall but defined by a internal density gradient that remains smooth [33, 40, 41].

7.4 Conclusions

We have shown how the possibility of star polymers to form non-hexagonal lattices in two dimensions depends strongly on the exact details of the tail of their interaction potential. Since it remains unclear how these interactions take shape for existing experimental star polymer systems it is impossible to predict the viability of star polymers as an experimental platform to template for example honeycomb lattices. Therefore, the most promising approach would be to design chemical routes to prepare star polymers whose tail interactions can be tuned, taking advantage of the recent developments in polymer synthesis[42, 43, 44]. For example, synthetic routes exist to functionalise the end group at each of the f arms attached to the star core[45, 46]. To approach the Yukawa-tailed pair potential, functionalisation of the arm ends with a charged group may give rise to an exponential tail whose range can be tailored by means of ionic strength. Interestingly, if the star arm interpenetrate during compression, the electrostatic repulsion emerging from these charged end groups would be maximum at contact $r = \sigma$, while further compression reduces the electrostatic repulsion as the charged ends of the two opposing stars move further apart either by backfolding or interpenetration of the arms. This could hypothetically result in a shoulder in the potential, which has been shown to greatly increase the complexity of the phase diagram[19, 15]. A second strategy to tune the tail interactions, is the use of special miktoarm stars, whose arms are identical in chemical composition but bidisperse in length. In this case, a dense core of short arms will set the range and strength of the core repulsion while a dilute corona of longer arms governs the interactions beyond the star diameter. This system would offer excellent tuneability through arm number and ratio, and length ratio of the short and long arms.

7.5 Acknowledgements

The authors acknowledge Ruben Higler for assistance with data analysis. The work of PvdS is funded by the Netherlands Organisation for Scientific Research (NWO) under the TOP-PUNT superficial superstructures programme. Project number: 718.015.002.

References

[1] Park, M., Harrison, C., Chaikin, P. M., Register, R. A. & Adamson, D. H. Block copolymer lithography: periodic arrays of˜ 1011 holes in 1 square centimeter. *Science* **276**, 1401–1404 (1997).

[2] Vogel, N., Weiss, C. K. & Landfester, K. From soft to hard: the generation of functional and complex colloidal monolayers for nanolithography. *Soft Matter* **8**, 4044–4061 (2012).

[3] Boneschanscher, M. P. *et al.* Long-range orientation and atomic attachment of nanocrystals in 2d honeycomb superlattices. *Science* **344**, 1377–1380 (2014).

[4] Zheng, J. *et al.* Two-dimensional nanoparticle arrays show the organizational power of robust dna motifs. *Nano letters* **6**, 1502–1504 (2006).

[5] Kalsin, A. M. *et al.* Electrostatic self-assembly of binary nanoparticle crystals with a diamond-like lattice. *Science* **312**, 420–424 (2006).

[6] Kosterlitz, J. M. & Thouless, D. J. Ordering, metastability and phase transitions in two-dimensional systems. *Journal of Physics C: Solid State Physics* **6**, 1181 (1973).

[7] Hartmann, P., Kalman, G. J., Donkó, Z. & Kutasi, K. Equilibrium properties and phase diagram of two-dimensional yukawa systems. *Phys. Rev. E* **72**, 026409 (2005).

[8] Pieranski, P., Strzelecki, L. & Pansu, B. Thin colloidal crystals. *Phys. Rev. Lett.* **50**, 900–903 (1983).

[9] Alder, B. J. & Wainwright, T. E. Phase transition in elastic disks. *Phys. Rev.* **127**, 359–361 (1962).

[10] Glotzer, S. C. & Solomon, M. J. Anisotropy of building blocks and their assembly into complex structures. *Nature materials* **6**, 557–562 (2007).

[11] Chen, Q., Bae, S. C. & Granick, S. Directed self-assembly of a colloidal kagome lattice. *Nature* **469**, 381–384 (2011).

[12] Winfree, E., Liu, F., Wenzler, L. A. & Seeman, N. C. Design and self-assembly of two-dimensional dna crystals. *Nature* **394**, 539–544 (1998).

[13] Vogel, N., de Viguerie, L., Jonas, U., Weiss, C. K. & Landfester, K. Wafer-scale fabrication of ordered binary colloidal monolayers with adjustable stoichiometries. *Advanced functional materials* **21**, 3064–3073 (2011).

[14] Ershov, D., Sprakel, J., Appel, J., Stuart, M. A. C. & van der Gucht, J. Capillarity-induced ordering of spherical colloids on an interface with anisotropic curvature. *Proceedings of the National Academy of Sciences* **110**, 9220–9224 (2013).

[15] Costa Campos, L. Q., de Souza Silva, C. C. & Apolinario, S. W. S. Structural phases of colloids interacting via a flat-well potential. *Phys. Rev. E* **86**, 051402 (2012).

[16] Engel, M. & Trebin, H.-R. Self-assembly of monatomic complex crystals and quasicrystals with a double-well interaction potential. *Phys. Rev. Lett.* **98**, 225505 (2007).

[17] Rechtsman, M. C., Stillinger, F. H. & Torquato, S. Optimized interactions for targeted self-assembly: Application to a honeycomb lattice. *Phys. Rev. Lett.* **95**, 228301 (2005).

[18] Sinelnik, A. D., Rybin, M. V., Lukashenko, S. Y., Limonov, M. F. & Samusev, K. B. Optical properties of honeycomb photonic structures. *Phys. Rev. A* **95**, 063837 (2017).

[19] Camp, P. J. Structure and phase behavior of a two-dimensional system with core-softened and long-range repulsive interactions. *Phys. Rev. E* **68**, 061506 (2003).

[20] Dotera, T., Oshiro, T. & Ziherl, P. Mosaic two-lengthscale quasicrystals. *Nature* **506**, 208–211 (2014).

[21] Fischer, S. *et al.* Colloidal quasicrystals with 12-fold and 18-fold diffraction symmetry. *Proceedings of the National Academy of Sciences* **108**, 1810–1814 (2011).

[22] Malescio, G. & Pellicane, G. Stripe patterns in two-dimensional systems with core-corona molecular architecture. *Phys. Rev. E* **70**, 021202 (2004).

[23] Schoberth, H. G. *et al.* Molecular dynamics study of colloidal quasicrystals. *Soft Matter* **12**, 7644–7654 (2016).

[24] Miller, W. L. & Cacciuto, A. Two-dimensional packing of soft particles and the soft generalized thomson problem. *Soft Matter* **7**, 7552–7559 (2011).

[25] Egorov, S. A., Paturej, J., Likos, C. N. & Milchev, A. Controlling the interactions between soft colloids via surface adsorption. *Macromolecules* **46**, 3648–3653 (2013).

[26] Likos, C. N. *et al.* Star polymers viewed as ultrasoft colloidal particles. *Phys. Rev. Lett.* **80**, 4450–4453 (1998).

[27] Jusufi, A., Watzlawek, M. & Löwen, H. Effective interaction between star polymers.

Macromolecules **32**, 4470–4473 (1999).

[28] Cerda, J. J., Sintes, T. & Toral, R. Pair interaction between end-grafted polymers onto spherical surfaces: A monte carlo study. *Macromolecules* **36**, 1407–1413 (2003).

[29] Von Ferber, C., Jusufi, A., Likos, C., Löwen, H. & Watzlawek, M. Triplet interactions in star polymer solutions. *The European Physical Journal E* **2**, 311–318 (2000).

[30] Huissmann, S., Blaak, R. & Likos, C. N. Star polymers in solvents of varying quality. *Macromolecules* **42**, 2806–2816 (2009).

[31] von Ferber, C., Jusufi, A., Watzlawek, M., Likos, C. N. & Löwen, H. Polydisperse star polymer solutions. *Phys. Rev. E* **62**, 6949–6956 (2000).

[32] Watzlawek, M., Likos, C. N. & Löwen, H. Phase diagram of star polymer solutions. *Phys. Rev. Lett.* **82**, 5289–5292 (1999).

[33] Daoud, M. & Cotton, J.P. Star shaped polymers : a model for the conformation and its concentration dependence. *J. Phys. France* **43**, 531–538 (1982).

[34] Prestipino, S., Saija, F. & Giaquinta, P. V. Hexatic phase in the two-dimensional gaussian-core model. *Phys. Rev. Lett.* **106**, 235701 (2011).

[35] Totsuji, H., Totsuji, C. & Tsuruta, K. Structure of finite two-dimensional yukawa lattices: Dust crystals. *Physical Review E* **64**, 066402 (2001).

[36] Hartmann, P., Kalman, G., Donkó, Z. & Kutasi, K. Equilibrium properties and phase diagram of two-dimensional yukawa systems. *Physical Review E* **72**, 026409 (2005).

[37] Likos, C. N., Lang, A., Watzlawek, M. & Löwen, H. Criterion for determining clustering versus reentrant melting behavior for bounded interaction potentials. *Phys. Rev. E* **63**, 031206 (2001).

[38] Peeters, F. & Wu, X. Wigner crystal of a screened-coulomb-interaction colloidal system in two dimensions. *Physical Review A* **35**, 3109 (1987).

[39] Ziherl, P. & Kamien, R. D. Soap froths and crystal structures. *Phys. Rev. Lett.* **85**, 3528–3531 (2000).

[40] Grest, G. S., Kremer, K. & Witten, T. Structure of many arm star polymers: a molecular dynamics simulation. *Macromolecules* **20**, 1376–1383 (1987).

[41] Huissmann, S., Blaak, R. & Likos, C. N. Star polymers in solvents of varying quality. *Macromolecules* **42**, 2806–2816 (2009).

[42] Ren, J. M. *et al.* Star polymers. *Chemical reviews* **116**, 6743–6836 (2016).

[43] Gao, H. & Matyjaszewski, K. Synthesis of functional polymers with controlled architecture by crp of monomers in the presence of cross-linkers: from stars to gels. *Progress in Polymer Science* **34**, 317–350 (2009).

[44] Blencowe, A., Tan, J. F., Goh, T. K. & Qiao, G. G. Core cross-linked star polymers via controlled radical polymerisation. *Polymer* **50**, 5 – 32 (2009).

[45] Zhang, X., Xia, J. & Matyjaszewski, K. End-functional poly (tert-butyl acrylate) star polymers by controlled radical polymerization. *Macromolecules* **33**, 2340–2345

(2000).

[46] Boyer, C., Whittaker, M. & Davis, T. P. Synthesis and postfunctionalization of well-defined star polymers via “double” click chemistry. *Journal of Polymer Science Part A: Polymer Chemistry* **49**, 5245–5256 (2011).

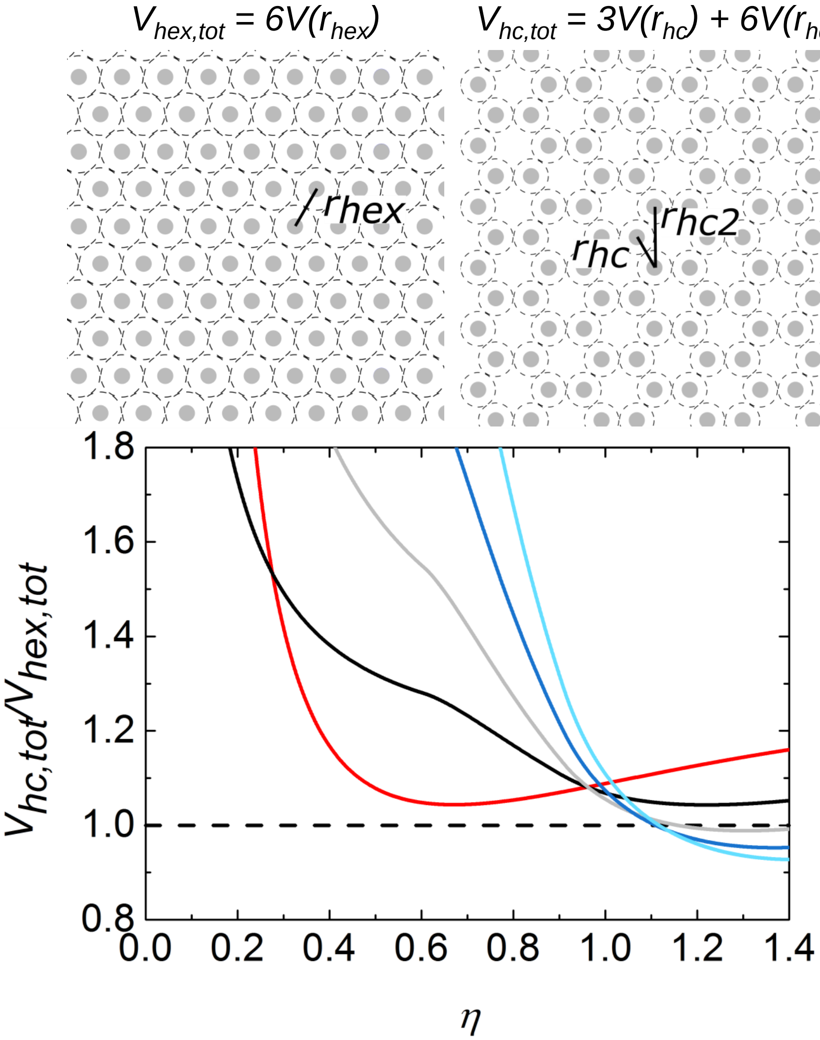

Figure 7.5: Analytical comparison of the ground-state energy of hexagonal and honeycomb lattices. Top: example structures of hexagonal pattern and honeycomb pattern, both with the same star packing fraction η. Top left: stars (grey spheres) are positioned in a hexagonal pattern of hard spheres (indicated with striped lines). The diameter of the hard spheres and thus the first neighbour distance is r_{hex}. Top right: stars are positioned in honeycomb pattern at a distance r_{hc} from each other. Bottom: comparison of the hexagonal and honeycomb energy as function of packing fraction.

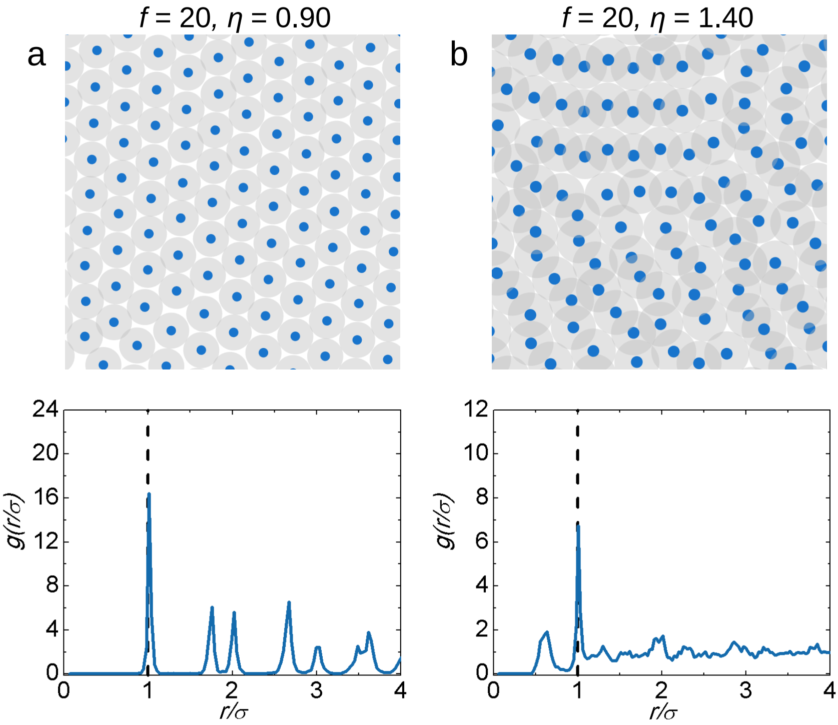

Figure 7.6: Examples of structures formed with a two-dimensional shifted and truncated star potential without long range interactions (top) and their corresponding pair correlation functions (bottom). Vertical striped line indicates the distance at which $r = \sigma$.

General Discussion

The central question underlying the work presented in this thesis is to understand how how the properties and interactions of the constituent building blocks of a material on the smallest scale, influences the properties of that material at the macroscopic scale. In this thesis, we have explored the phase behaviour and dynamics of soft colloidal particles, in glasses and crystals, and explored the development of a new class of mechanically-responsive macromolecular sensors. Due to the broadness of this research, and the wide application potential of the sensors developed in the previous chapters, many questions remain unanswered. This last chapter addresses several of these questions and how they may be answered in future research, supported by preliminary data.

8.1 Calibration of molecular strain sensors

Understanding the coupling between mechanics at the molecular scale, and macroscopic behavior in soft polymer materials is a challenging task. A new class of macromolecular sensors, which use a sensitive coupling between intramolecular energy transfer and chain conformation, are capable of resolving mechanical features at the smallest length scales. These sensors offer new opportunities to address this challenge. In this thesis, we have strived to arrive at a deeper understanding of these macromolecular sensors by addressing two main problems.

The backbone of these polymeric sensors consists of donor units, into which acceptor units are introduced as dopants. If the polymer chain is in a relaxed and coiled conformation, figure8.1a, the local density of donors, within a volume set by the Forster radius of the donor-acceptor pair, is large. This gives rise to efficient transfer of the excited state energy of the donor units to the acceptors; thus the FRET efficiency is high. When mechanical stress acts on the polymer, it becomes stretched and the local donor density around acceptors decreases, resulting in a reduction of the energy transfer efficiency.

In **Chapter 4**, we addressed the issue of chain length polydispersity that, until recently, was the norm for the macromolecular mechanosensors developed by our group in the past [1]. In this Chapter, we have shown that the intramolecular energy transfer, on the basis of which the mechanosensors derive their function, is strongly dependent on the chain length of the acceptor-doped conjugated polymers. We have shown how this results from the probabilistic nature of the incorporation of the acceptor units during synthetic procedures, resulting in strong chain-length dependencies at short chain lengths. These results imply that strong chain length polydispersity limits the resolution with which these sensors can resolve mechanical features in the materials in which they are embedded. In **Chapter 4**, we show how to resolve this. By using an extensive solvent-gradient Soxhlet-extractions, we are now able to separate fractions of the polymer chain population which have a more homogeneous distribution of both chain-length and acceptor distribution. These Chapters provide a deeper understanding of the limits of these mechanosensors, and form a basis to work towards increasing the accuracy and sensitivity of these acceptor-doped conjugated polymers in sensory applications.[2, 3, 4]

The conformation-dependent energy transfer in these polymers has been exploited for example to study self-assembly of viruses, detection of DNA and other sensory applications.[5, 6, 7] Recently, it was shown that by considering the polymer chain as an entropic spring with a corresponding spring constant the optical response of the polymeric sensor can

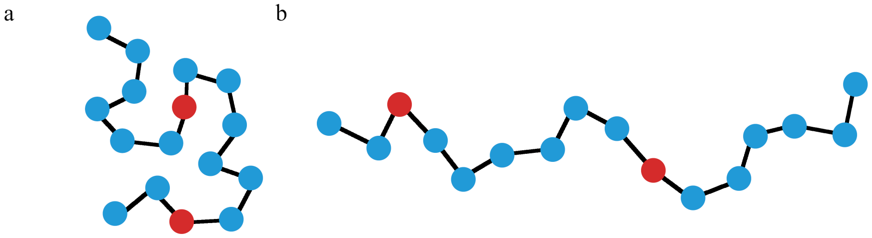

Figure 8.1: Schematic overview of an acceptor-doped polymer chain in a coiled and stretched conformation with the red monomers indicating an acceptor unit.

be used to deduce local mechanical strains on the individual molecules.[1] Since conjugated polymers are highly suitability for single molecule spectroscopy experiments, due to their brightness and relative photostability, this creates possibilities to not only measure minute strains with high temporal resolution but on nanometric length scales.

However, due to chemical variations between different batches of polymers or when altering the sensor design, each new sample required renewed calibration of the mechano-optical response. At current, these calibrations are based on single-molecule spectroscopy experiments, which are laborious and challenging.

To reduce the time required to construct a quantitative calibration curve, and to increase the range of strains that can be explored, we explored a new calibration method based on flow-focussing microfluidics. In a hydrodynamic focussing experiment, figure8.2a, a central fluid stream is focused by two lateral fluid flow channels. By changing the ratio of the flow rates between the central and lateral channels, the strength of the flow focusing can be tuned. In the narrowing region of the central fluid stream, a strong gradient in flow velocity is established, which results in substantial tensile forces applied onto the molecules dissolved in the central fluid. These hydrodynamic stresses cause polymer coils to stretch. This approach has already been successfully used to stretch and align worm-like micelles [8] and DNA [9, 10]. Extensive theoretical exploration of the coil-stretch transition in these types of flows have also been performed, most notably by DeGennes, Zimm, and others. [11, 12, 13, 14] In the focussing junction, a wide range of extensional strain rates occur as a function of position in the junction. At each of these positions, the strain rate can in principle be measured quantitatively through the use of Particle Imaging Velocimetry experiments. [15, 16] While the residence time of polymers in the focussing junction is low, of the order of milliseconds, excitation and fluorescence emission, occurs on much smaller (nanosecond) timescales, such that optical interrogation of the molecules in the device enables accurate measurement of the conformational state. By ensuring acquisition times well in excess of millisecond residence time, large ensemble-averages can be obtained in these experiments. Because these devices can be engineered from optically transparent materials, microspectroscopic imaging, gives access to the optical response of the molecules at each point in the focussing junction. In a single-experiment, one thus obtains a large set of strain rates and corresponding optical responses, in principle enabling the construction of quantitative calibration curves in a very short amount of time.

The spectral information obtained from a confocal laser scanning microscopy (CLSM) experiment is limited due to the splitting of all the detected light into two pre-defined channels. To accurately measure the energy transfer between the donors and acceptors in the molecules of interest, additional steps must be taken. In fluorescence emission spectroscopy, the FRET ratio E is often determined by the ratio of the donor (D) and acceptor (A) peak integrals according to: $E = \frac{\sum I_A}{\sum I_A + \sum I_D}$. The CLSM detects light on separate channels with a pre-defined spectral range. The wavelength range of each channel is pre-set by the selected filters and dichroics and does not guarantee that the complete emission band of either donor or acceptor is captured; this must be corrected in the data analysis. There can also be some contribution from direct excitation of the acceptor and the donor emission band could bleed into the acceptor chan-

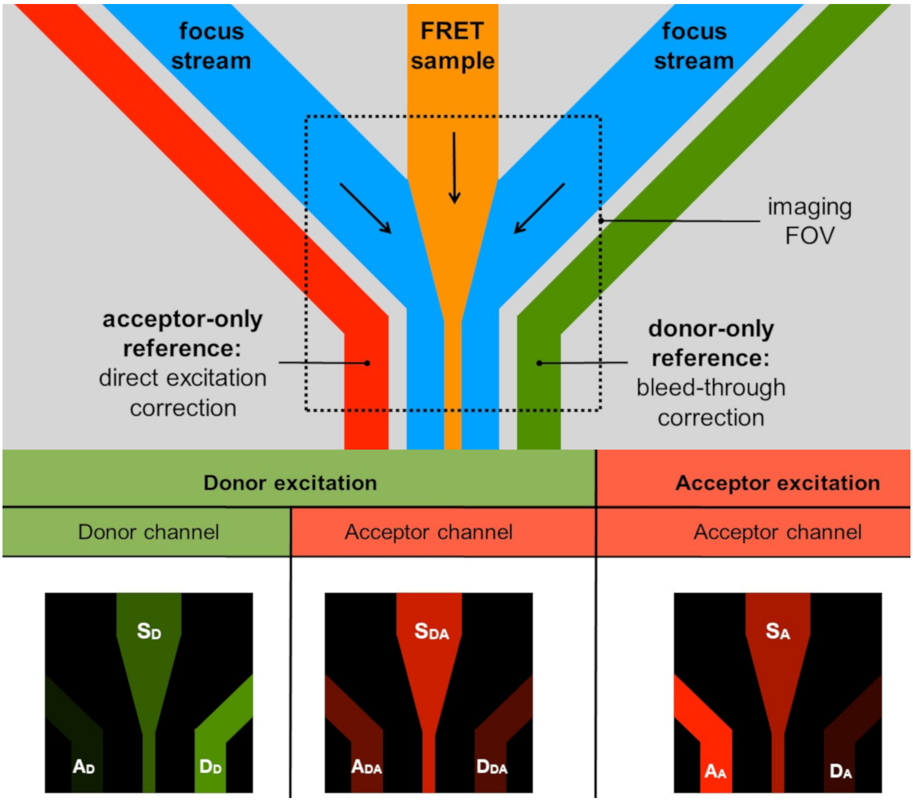

Figure 8.2: a) A schematic overview of the microfluidic cross-flow focussing device. The FRET-sample channel containing a donor-acceptor labelled polymer is focused at the intersection by the two focusing channels. The acceptor-only and donor-only channels contain the identical polymer doped with either donor or acceptor chromophore exclusively. The dimensions of the FOV are 200μm by 200μm and the height of the channels is 40μm. b) A schematic representation of the optical response of the device upon donor excitation and detection with the donor channel and acceptor channels of the CLSM. And the optical response upon direct acceptor excitation and detection in the acceptor channel of the CLSM. The specific excitation and detection states are abbreviated for each channel and used as such in equation 8.4 to calculate the normalized energy transfer.

nel. To compensate for these effects and calculate an accurate unbiased FRET ratio a method has been developed by Gascoine *et al.*[17] This method requires emission data of the donor in absence of the acceptor and vice-versa. To avoid inaccuracies in our calibration due to small optical variations between experiments, we extend our micro-fluidic design to also contain a donor- and acceptor-only channel. In figure 8.2a we show a new design for a flow-focussing microfluidic chip, where, in a single field of view of 200 by 200 microns, we can determine not only the cross-flow focusing of our sensor solution, but simultaneously detect the required reference data for quantitative determination of the FRET response. To convert the measured donor-acceptor ratio into a quantitative FRET efficiency we use the approach of Gascoine[17], which we have schematically illustrated in figure 8.2b. From this, the normalized FRET is obtained as follows:

$$E_{norm} = \frac{S_{DA} - R_{DE}S_A - R_{BT}S_D}{S_{DA} - R_{DE}S_A + (G - R_{BT})S_D} \tag{8.4}$$

in which R_{DE} a correction for the direct acceptor excitation and is defined as $R_{DE} = \frac{A_{DA}}{A_A}$, R_{BT} is used to correct for donor bleed-through and defined as $R_{BT} = \frac{D_{DA}}{D_D}$. The only parameter not measurable directly is G, which is defined as $G = \frac{Q_A\phi_A}{Q_D\phi_D}$ where the Q_A and Q_D are the respective quantum yields of the donor and acceptor and ϕ_D and ϕ_A are the filter transmission values for the donor and acceptor, respectively. These can be determined from their fluorescence emission spectra and the spectral cutoffs of the respective channels.

We prepare the device from optically-clear PDMS by soft UV-lithography. The PDMS device is bonded to a spectroscopy-grade glass slide by plasma activation. In figure 8.3 we show experimental data in the same representation as used in the schematic in figure 8.2b, with fig.8.2a the donor channel upon donor excitation, fig. 8.2b the acceptor channel upon donor excitation and fig. 8.2c the acceptor channel upon direct acceptor excitation. As a molecular probe, we use a water soluble polylysine polymer of 400 repeat units which has been covalently labelled with the water-soluble fluorescent dyes ATTO-465 as donor and RITC as acceptor. We

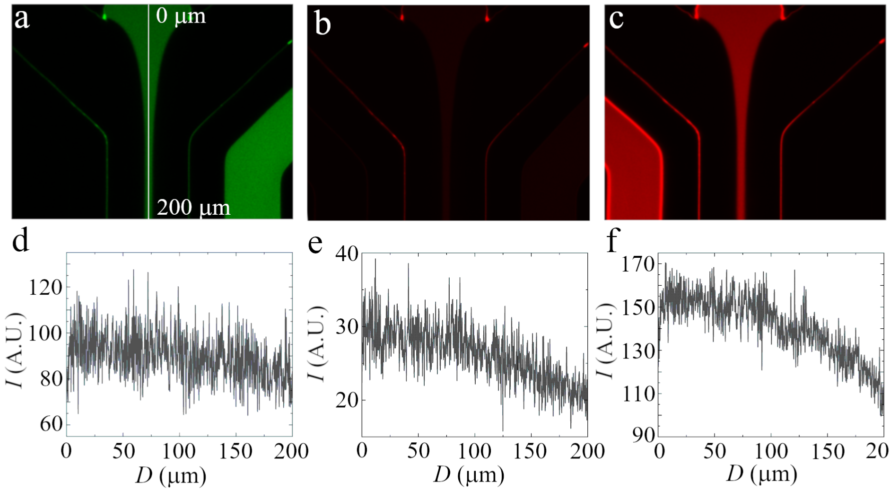

Figure 8.3: Experimental confocal laser scanning microscopy data of microfluidic devices with our fluorescent polymers in flow. Where a) the donor channel upon excitation of the donor chromophore b) the acceptor channel upon excitation of the donor chromophore and c) the acceptor channel upon excitation of the acceptor chromophore. d-f) the corresponding intensity traces along the flow direction for each channel as shown in a.

compose an intensity profile of the emission of the different channels in the center of the flow channel as indicated by the light line in figure 8.2a. Upon direct excitation, both donor and acceptor show strong emission, both on the FRET polymer, which carries both probes, and on the reference polymers which carry only donors or only acceptors. This indicates that neither the attachment chemistry nor the presence of both dye interferes with its fluorescent properties. The acceptor emission upon excitation of the donor, which only emits if FRET occurs, is almost not visible. If we look at the intensity trace in figure 8.3e we can see it is a factor five lower than when the acceptor is directly excited and its signal is not much higher than the background. Although there is a decrease in fluorescence emission in the direction of the channel this follows the same trend as the decrease in the acceptor when it is directly excited.

However, due to the very low intensity of the signal we were forced to reconsider the design of the polymer sensor. To reduce the average distance between donor and acceptor chromophores and increase the energy transfer between them we increased the overall doping. However, we found there was a practical limitation to this caused by hydrophobic interactions between the dye. Absorption spectra showed additional red-shifted absorption bands attributed in literature to intramolecular aggregation of dye molecules.[18, 19] This was also confirmed by quantum yield measurements, which which were increasingly low at higher fluorescent-labelling degrees. Due to time constraints, not further explorations have been possible. However, since the approach appears promising, explorations of other chemistries to create mechanoresponsive polymers, compatible with PDMS (which precludes the use of organic solvents), or the construction of the device from glass to enable the use of our molecular sensors developed in **Chapter 4 & 3**, are logically future directions for this research.

Although this method is promising for the applied purpose of spectral calibration of polymeric force sensors its use can also be extended. There has been an rise in interest over the past years in mechano-chemistry with an increase in development of new dynamic materials. [20, 21, 22, 23] (Many of whom show a spectroscopic change as a function of a mechanical response. Because forces have to be transferred to a such mechanophores, polymeric tethers must be attached to help transfer these forces to the central molecule of interest. With further development, this microfluidic method should make it possible to quickly screen the mechano-activity of molecular constructs.

8.2 Length-scale dependence of the response of molecular rotors

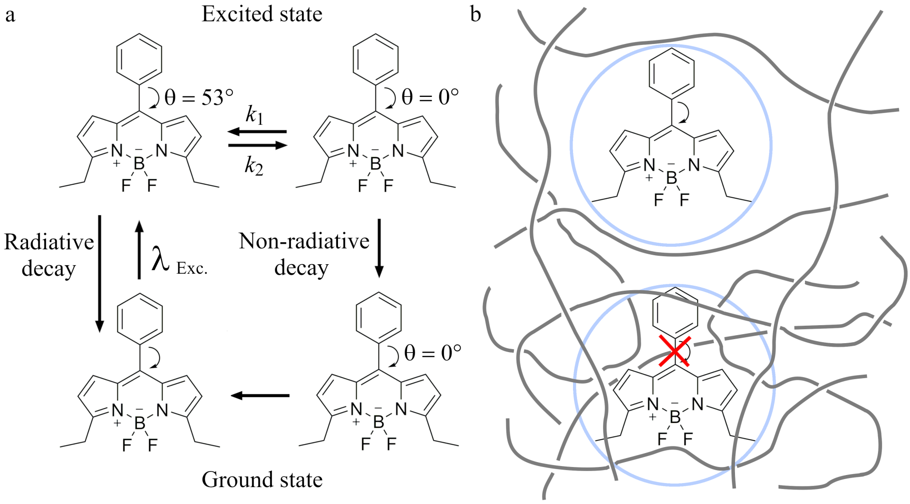

Figure 8.4: a) A systematic overview of the different relaxation pathways available to a bodipy based molecular rotor upon excitation. b) The influence of steric hinderance of a complex polymeric material on the rotation of a bodipy rotor illustrating the effect of the length-scale of the molecule.

Molecular rotors are molecular probes which undergo an internal rotation upon photo-excitation. Rotation to this twisted state enables a pathway for non-radiative decay of the excited state. Since the rate of rotation can be hindered by a mechanical coupling to the environment, molecular rotors feature a unique mechano-optical fluorescence response which can be used for micromechanical imaging. Molecular rotors are often advertised as being rigidochromic, i.e. responding to the viscosity of the surrounding medium.[24, 25] However, their use in the quantitative determination of local viscosities is hindered by some additional effects, which remain incompletely understood. In fact, in scenarios that are more complex than simple molecular solvents, such as their applications in materials and/or biological systems, what is measured exactly is not entirely clear. The mechanisms of the mechano-optical coupling for the BODIPY class of rotors, which we have used in this thesis, is shown in figure 8.4a. In the ground state, the energetically most favorable conformation features a 53° angle between the BODIPY core and the phenyl ring.[26, 27, 28] Upon photo-excitation, this conformation becomes energetically unfavorable and leading to an internal rotational motion to a flat configuration with a 0° angle between phenyl ring and BODIPY core. In a non-viscous medium relaxation will predominately occur non-radiatively by allowing this rotation to occur more rapidly than fluorescence emission. However, when the medium becomes more viscous the rotation of the phenyl ring becomes hindered, leading to fluorescence emission as the primary decay pathway of the excited state. This leads to an increase in fluorescence intensity and in the lifetime of the excited state.

In **Chapter 3**, we have shown that the incorporation of molecular rotors, of the BODIPY class, into conjugated polymers retains rotor function and enables the use of the rotor-doped conjugated polymer as a ratiometric micromechanical probe. This design combines high quantum yield of a conjugated polymer with high local rotor concentration. This enables its use in single molecule measurements retaining high local rotor concentrations. These macromolecular polyrotors respond very consistently upon calibrating their optical response, either spectroscopically or through fluorescence lifetime measurements, in simple viscous solutions of molecular solvents.

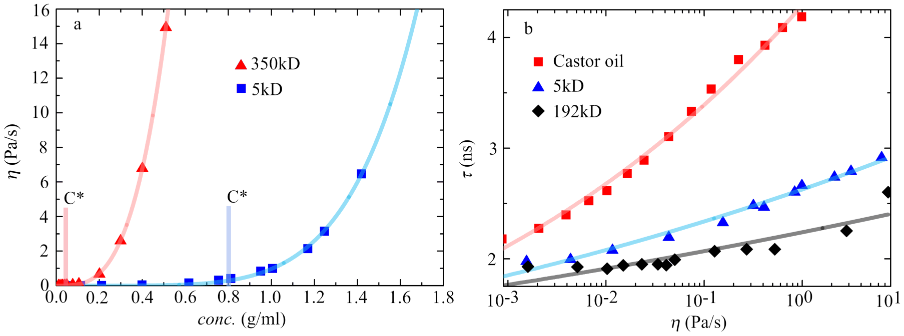

Figure 8.5: a) The viscosity as a function of concentration for polystyrene of 350 and 5kD in different weight percentages in NMP determined by rheology. The critical overlap concentration for each polymer is marked as c*. b) The fluorescent-lifetime response of a bodipy molecular rotor as a function of viscosity for different polymer solutions.

However, for complex materials such as polymer or protein solutions the macroscopic properties such as viscosity are caused by interactions between large macromolecules. These 'complex' fluids thus feature larger length scales than in the case of a simple liquid formed from small molecules. The rotation of the rotor is sensitive to a local coupling to the medium at a length scale comparable to its molecular dimensions. A solution consisting of a small weight percent of high molecular weight polymer, although largely consisting of solvent, can have a high macroscopic viscosity. At the scale of the molecular rotor however, the complex fluid consists largely of empty liquid (as illustrated in Fig.8.4b). Thus, the rotor probes a length-scale dependent hydrodynamic coupling to the medium, which cannot always be interpreted in terms of a macroscopic viscosity. In this sense, rotors are not sensitive to viscosity per-se, by to the local free volume available to perform their internal rotational motion. We could in principle prepare two solutions of polymers of differing molecular weight with identical macroscopic viscosity, but in which the hindrance of the rotational motion of a molecular probe is vastly different (Fig.8.4b).

To verify this, we performed fluorescent lifetime measurements and rheology on polymer solutions containing a BODIPY molecular rotor. We vary the polymer chain-length and compare these results with those obtained for castor oil, as an example of a small-molecule viscous fluid. In figure 8.5b , we show the fluorescent lifetime response of the molecular rotor as a function of the viscosity for these different samples. We can clearly see that there is a difference in rotor response for the different samples. The castor oil shows a continuous response whereas both the polymer solutions show a plateau at low concentrations, below the polymer overlap concentration c^{*}, which is shorter for the higher molecular weight polymer, as this has a lower c^{*}. Plotted as a function of the macroscopic viscosity, our point becomes directly clear. There is no collapse of the fluorescent lifetime curves as a function of macroscopic viscosity, but rather, a length-scale dependence emerges.

These data form a cautionary warning to the users of molecular rotors as viscosity probes; calibration of the viscosity-lifetime response in low-molecular weight solvents does not enable to deduction of macroscopic viscosities in more complex environments such as in materials or biological systems. Rather, rotors can be used as qualitative probes to reveal spatial inhomogeneities in local free volume, or must be calibrated in media of similar nature and length scale as the sample of interest.

8.3 Sensing phase separations in confinement

One of the ultimate aims in our explorations and development of mechanically-responsive optical probes was to explore phenomena in soft materials at scales that are not readily accessible by conventional bulk-measurement methods. One of these examples relates to the study of soft materials under extreme confinement. Confinement can greatly alter the stability boundaries and transition kinetics of condensed phases. In particular in polymeric systems, where the primary building blocks are of mesoscopic dimensions, confinement to the nanoscale can drastically influence not only the rate with which phase transitions occur, but alter the location of phase boundaries and even give rise to phases which are not stable in bulk systems. These confinement effect emerge across a wide variety of transitions ranging from phase separation in blends, the glass transition to crystallisation and aggregation in monocomponent systems and mixtures. Studying polymeric phase transitions in confinement is not only of interest from a fundamental perspective, to understand how boundary effects alter polymeric dynamics and influence the very nature of the resulting phases itself, but also of crucial interest to the development of complex polymeric nanomaterials. Most experimental studies attempting to resolve the effects of confinement on phase transitions and their kinetics in polymers have focussed on two-dimensional confinement in supported or free-standing polymer films, or on one-dimensional confinement, e.g. in cylindrical nanopores. In these cases, macroscopic proportions remain at least in one spatial dimension. The effects of confinement in zero dimensions, in which matter is confined into nanoparticles, has been studied in detail for inorganic semiconductors, where the confinement not only induces quantum mechanical properties not found in the bulk, such as the confined-induced quantization of energy levels in quantum dots, but the strong interfacial curvature of the resulting nanoparticles activates the thermodynamic laws of Kelvin and Laplace, leading to strong changes in particle stability and mechanics. For polymers, the effects of zero-dimensional (0-D) confinement on phase stability and transition kinetics has remained relatively unexplored, despite its obvious importance in the preparation and use of polymeric nanoparticles. Polymer nanoparticles prepared from conventional polymer find widespread use in an immense variety of consumer products, for example as binders in sustainable coatings, fillers in nanocomposites, or in drug delivery formulations. In many cases, these particles are prepared from blends of polymers to tailor their mechanical or functional properties; for example, in coatings, core-shell architectures are often used to achieve the desired application properties. Polymer particles prepared from semiconducting polymers, as organic alternatives to semiconductor quantum dots, have emerged as promising building blocks for a new generation of nanostructured photovoltaic and optoelectronic devices. Also here, blending and control of their internal structure is used to tailor their optoelectronic profiles to meet the desired requirements. Nonetheless, little is known on the effects of 0-D confinement on phase transitions in mixed polymeric systems. While it is known that polymer blends often phase separate, which can even induce partial crystallisation of one or both of the polymers in certain cases, it remains unclear how this is effected by a strong and homogeneous confinement down to the nanoscale. This is in part caused by the lack of experimental approaches to resolve phase transitions in polymeric systems at these small length scales in-situ as the phase transition occurs.

Here we show our preliminary efforts in using macromolecular sensors as a probe to unravel the kinetics of phase separation in confined polymeric blends. For our preliminary experiments, we prepare a polymer solution of our acceptor-doped conjugated sensor, as described in detail in **Chapter 4**, mixed with polystyrene in toluene below the concentration where these two incompatible polymer demix. To expose these mixtures to strong confinement, we encapsulate them in small emulsion droplets, by preparation of a mini-emulsion of our organic phase in toluene-saturated water.[31, 29] The emulsion droplets are stabilized by surfactant and stable in the water phase, and have dimensions of 50 - 250 nm, tunable by the preparation protocol.[30, 31] We ensure that the water-phase is pre-saturated with toluene, such that the size of the droplets is stable as long as evapor-

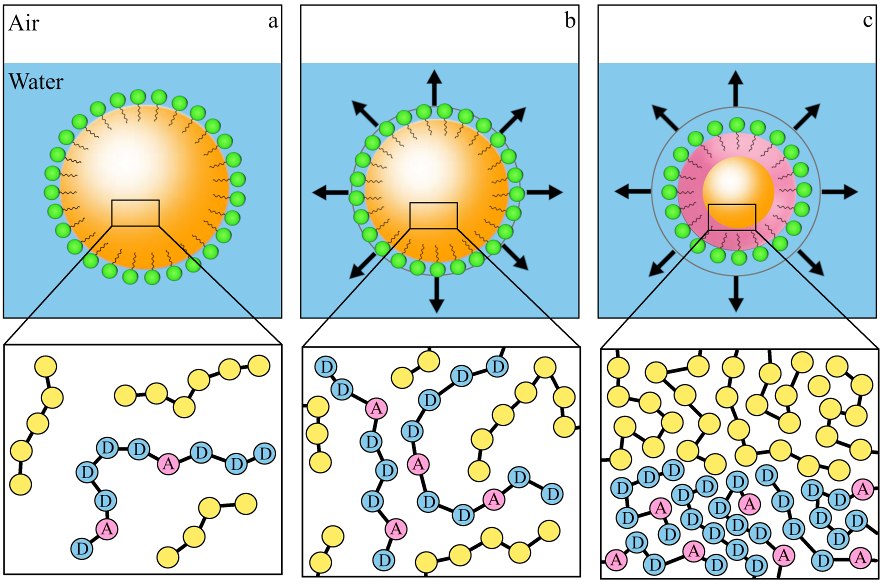

Figure 8.6: a) A schematic overview of an emulsion droplet consisting of a mixture of two polymers in toluene. As the emulsion is exposed to air the solent, toluene, will evaporate. The particles will shrink, b, and the polymer concentration will increase within the particle. Up to the point where phase separation of the two polymers will occur within the droplet, c.

ation is prohibited. Once the dilute emulsion is allowed to evaporate the emulsion droplets will evaporate their solvent upon which the internal polymer concentration in the droplets rises. Below the critical phase separation concentration, the polymers will stay mixed and the intermolecular distance between all polymers will decrease homogeneously. The average distance between donor and acceptor monomers becomes smaller and on average the energy transfer, not nescesarilly within the same chain, will increase. Once the critical concentration limit has been passed, the polymer liquid can phase-separate if the situation allows. Because this has no effect on the solvent flux out of the emulsion droplet the droplet will continue to shrink at the same rate. However the intermolecular distances between conjugated polymers will decrease more sharply due to the fractionation of the two polymer phases. If we monitor the fluorescence emission of the conjugated polymer we can obtain the energy transfer as a function of time of which the rate should show different regimes depending on the phase stability of the emulsion droplet. Because we can change the size of the emulsion droplet and the starting polymer concentration we are able to control at which size of the confining droplet the critical phase separation concentration is reached. More importantly we are able to study the phase separation at different degrees of confinement.

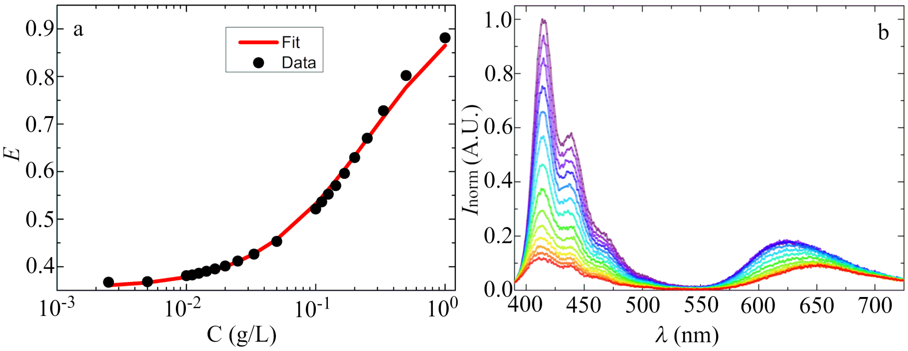

Figure 8.7: a) The energy transfer ratio, obtained from fluorescence emission spectra, as a function of concentration for our acceptor doped conjugated polymer. Fitted with an adapted form of the Förster equation using polymer concentration instead of distance between donor and acceptor, showing a quantitive relation between polymer concentration and energy transfer ratio. b) Fluorescence emission spectra for our conjugated polymer inside an emulsion as a function of time.

First, we verify that the intermolecular energy transfer between our sensor polymers occurs at concentrations which are experimentally relevant. In figure 8.7a we show the concentration dependent FRET ratio fitted to an adapted form of the Forster equation, derived for these sensor polymers in previous work in our group by de Laar *et al.*[1]. This not only shows that the intermolecular energy transfer is responsive to concentration in the relevant concentration regime, but that the energy transfer has a predictable shape with changing concentration, and can thus be used as a local probe to deduce polymer concentrations optically. Using this curve, and knowing the starting volume and polymer concentrations inside the droplet, measurements of the energy transfer efficiency E as s function of time allows computation of the exact size of the droplet and evaporative solvent flux.

We prepare our experimental sample as described above and measure the fluorescence emission at given intervals over time. In figure8.7b we show these spectra with the highest emission peak normalized to one. From this it is clear that over the course of the experiment the sensor is able to maintain a high enough quantum yield to enable measurements and that there is a clear change in energy transfer during this process. If we now calculate the energy transfer as a function of time, figure8.8a, we see a clear increase of energy transfer over time which shows three regimes. We plot the local slope of $E(t)$ as a function of time, 8.8b, we can see that after an some initial unsteadiness, a plateau is reached at 200 min which sharply increases at 500 min to reach another plateau. While preliminary, we believe that the change that occurs at around 400min signals the phase separation inside the nanoscopic droplets.

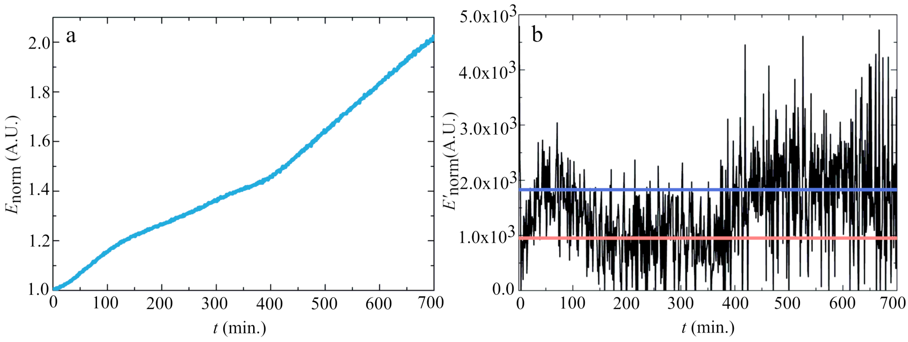

Figure 8.8: a) The normalized energy transfer ratio from an evaporation experiment obtained from fluorescence emission spectra. b) Direction coefficient of the normalized energy transfer ratio as a function of time. The lower plateau highlighted with a red line and the higher plateau with a blue line.

These results, figure8.7a, show that the intermolecular energy transfer between acceptor-doped conjugated polymers can also be harnessed for sensoric applications in a concentration range which has experimental relevance. The fluorescence emission spectra, as shown in figure8.8b, of conjugated polymers within the droplets making up the dilute emulsion, show almost no noise on the data. The small amount of conjugated polymer inside the droplets is able to produce enough fluorescence light to overcome experimental issues that could be expected in emulsions due to their strong scattering. At long times, we observe a red-shift of the acceptor emission band which could indicate aggregation of the sensor polymers. However, the data in figure8.8a shows no deviations up to 700 minutes and a change in kinetics due to phase separation can still be observed. Although not necessarily problematic, the solubility of the conjugated polymer sensor could be improved upon by reducing its length or by modifying the acceptor units with ethyl-hexyl side-groups to increase solubility and prevent crystallisation and stacking by steric hindrance. To ensure that particle sizes can be reached which are small enough to potentially suppress phase separation a systematic study should be performed to control the binodal of the conjugated polymer and a co-polymer. If the binodal of the two polymers at a given mixing ratio is too low the resulting emulsion will not be stable and monodisperse. And only a limited amount of solvent can be lost before phase separation occurs, limiting the control over particle size to the limits of the microemulsion protocol. If it is too high the solubility limit of the conjugated polymer could become problematic. If adequate control over the particle size range and dispersity can be gained, the conjugated polymer additionally gives information about its concentration in the particle. Giving us direct quantitative access to the evaporation kinetics with high temporal resolution. Due to time constraints no systematic study was performed on the influence of the droplet size on the demixing kinetics, however these preliminary data indicate it should be possible to do so with the sensors developed in this thesis.

References

[1] van de Laar, T. *et al.* Light from Within: Sensing Weak Strains and FemtoNewton Forces in Single Molecules. *Chem* **4**, 269–284 (2018).

[2] Gaylord, B. S., Heeger, A. J. & Bazan, G. C. Dna hybridization detection with water-soluble conjugated polymers and chromophore-labeled single-stranded dna. *Journal of the American Chemical Society* **125**, 896–900 (2003).

[3] Hong, J., Hemme, W., Keller, G., Rinke, M. & Bazan, G. Conjugated-polymer/dna interpolyelectrolyte complexes for accurate dna concentration determination. *Advanced Materials* **18**, 878–882 (2006).

[4] Feng, L., Liu, L., Lv, F., Bazan, G. C. & Wang, S. Preparation and biofunctionalization of multicolor conjugated polymer nanoparticles for imaging and detection of tumor cells. *Advanced Materials* **26**, 3926–3930 (2014).

[5] Lee, J., Kim, H.-J. & Kim, J. Polydiacetylene liposome arrays for selective potassium detection. *Journal of the American Chemical Society* **130**, 5010–5011 (2008).

[6] Seo, S. *et al.* Polydiacetylene liposome microarray toward influenza a virus detection: Effect of target size on turn-on signaling. *Macromolecular Rapid Communications* **34**, 743–748 (2013).

[7] Yoon, B., Lee, S. & Kim, J.-M. Recent conceptual and technological advances in polydiacetylene-based supramolecular chemosensors. *Chem. Soc. Rev.* **38**, 1958–1968 (2009).

[8] Pathak, J. A. & Hudson, S. D. Rheo-optics of equilibrium polymer solutions: Wormlike micelles in elongational flow in a microfluidic cross-slot. *Macromolecules* **39**, 8782–8792 (2006).

[9] Zimm, B. H. Extension in flow of a dna molecule tethered at one end. *Macromolecules* **31**, 6089–6098 (1998).

[10] Schroeder, C. M., Babcock, H. P., Shaqfeh, E. S. & Chu, S. Observation of polymer conformation hysteresis in extensional flow. *Science* **301**, 1515–1519 (2003).

[11] De Gennes, P. Coil-stretch transition of dilute flexible polymers under ultrahigh velocity gradients. *The Journal of Chemical Physics* **60**, 5030–5042 (1974).

[12] Peterlin, A. Hydrodynamics of linear macromolecules. *Pure and Applied Chemistry* **12**, 563–586 (1966).

[13] Lumley, J. L. Drag reduction by additives. *Annual review of fluid mechanics* **1**, 367–384 (1969).

[14] Zimm, B. H. Dynamics of polymer molecules in dilute solution: viscoelasticity, flow birefringence and dielectric loss. *The journal of chemical physics* **24**, 269–278 (1956).

[15] Zeighami, R. *et al.* Experimental investigation of flow transition in microchannels

using micron-resolution particle image velocimetry. In *ITHERM 2000. The Seventh Intersociety Conference on Thermal and Thermomechanical Phenomena in Electronic Systems (Cat. No. 00CH37069)*, vol. 2, 148–153 (IEEE, 2000).

[16] Grant, I. Particle image velocimetry: a review. *Proceedings of the Institution of Mechanical Engineers, Part C: Journal of Mechanical Engineering Science* **211**, 55–76 (1997).

[17] Zal, T. & Gascoigne, N. R. Photobleaching-corrected fret efficiency imaging of live cells. *Biophysical journal* **86**, 3923–3939 (2004).

[18] Fauvell, T. J. *et al.* Photophysical and morphological implications of single-strand conjugated polymer folding in solution. *Chemistry of Materials* **28**, 2814–2822 (2016).

[19] Cao, X. *et al.* Large red-shifted fluorescent emission via intermolecular π–π stacking in 4-ethynyl-1, 8-naphthalimide-based supramolecular assemblies. *Langmuir* **30**, 11753–11760 (2014).

[20] Paulusse, J. M. & Sijbesma, R. P. Reversible mechanochemistry of a pdii coordination polymer. *Angewandte Chemie International Edition* **43**, 4460–4462 (2004).

[21] Verstraeten, F., Göstl, R. & Sijbesma, R. Stress-induced colouration and crosslinking of polymeric materials by mechanochemical formation of triphenylimidazolyl radicals. *Chemical Communications* **52**, 8608–8611 (2016).

[22] Karthikeyan, S. & Sijbesma, R. P. Mechanochemistry: Forcing a molecule's hand. *Nature chemistry* **2**, 436 (2010).

[23] Takacs, L. The historical development of mechanochemistry. *Chemical Society Reviews* **42**, 7649–7659 (2013).

[24] Peinado, C., Salvador, E., Catalina, F. & Lozano, A. Solvatochromic and rigidochromic fluorescent probes based on d–π-a diaryl ethylene and butadiene derivatives for uv-curing monitoring. *Polymer* **42**, 2815–2825 (2001).

[25] Lees, A. J. The luminescence rigidochromic effect exhibited by organometallic complexes: rationale and applications. *Comments on Inorganic Chemistry* **17**, 319–346 (1995).

[26] Toliautas, S. *et al.* Enhancing the viscosity-sensitive range of a bodipy molecular rotor by two orders of magnitude. *Chemistry–A European Journal* (2019).

[27] Li, F. *et al.* Design, synthesis, and photodynamics of light-harvesting arrays comprised of a porphyrin and one, two, or eight boron-dipyrrin accessory pigments. *Journal of the American Chemical Society* **120**, 10001–10017 (1998).

[28] Kee, H. L. *et al.* Structural control of the photodynamics of boron- dipyrrin complexes. *The journal of physical chemistry B* **109**, 20433–20443 (2005).

[29] Landfester, K. & Crespy, D. Miniemulsion polymerization. *Materials Science and Technology* 449–474 (2006).

[30] Antonietti, M. & Landfester, K. Polyreactions in miniemulsions. *Progress in polymer science* **27**, 689–757 (2002).

[31] Staff, R. H., Landfester, K. & Crespy, D. Recent advances in the emulsion solvent evaporation technique for the preparation of nanoparticles and nanocapsules. In *Hierarchical Macromolecular Structures: 60 Years after the Staudinger Nobel Prize II*, 329–344 (Springer, 2013).

Summary

This thesis describes our explorations in the development of new molecular tools to probe complex soft material systems at the nanoscale. In large part, our efforts have been dedicated to conjugated polymer-based molecular sensors for applications in complex fluids. We have contributed both to developing new chemical strategies for incoorporating new function in these macromolecular sensors, but also to develop a deeper understanding of how they work and what their intrinsic limitations are.

In *Chapters 2, 3, 5* we explore new ways to introduce mechanoresponsive moieties into the backbone of semiconducting sensor polymers. In *Chapter 2* we introduce a spiropyran moiety into a polyfluorene backbone. Spiropyran functions as a molecular switch whose two states exhibit unique photochromic properties. The molecular switch can be activated by a variety of triggers including but not limited to mechanical-, pH-, light- and temperature-stimuli, and is thermally reversible in the small molecule state. Incorporated into the extended pi-conjugated system of a semiconducting polymer backbone, activation of these molecular switches results in spectroscopic shifts of the complete semi-conducting system and a loss of the thermal reversibility. We explore the influence of different chain architectures of spiropyran-co-fluorene polymers and the consequences of expanding the conjugation length of the spiropyran monomer on its switching properties.

In *Chapter 5* we continue along this concept, by introducing a different type of molecular switch into polyfluorene backbones. Here we focus our

attention to anthracene monomers, which remain susceptible to modification via a Diels-Alder reaction also post-polymerisation. The Diels-Alder adduct occurs anti-parallel on the central benzene ring of the anthracene causing splitting of conjugation into two isolated systems, thereby interrupting the flow of electrons along the semiconducting polymer backbone and straining the macromolecular conformation. Retro-Diels-Alder reactions, which restore the extended pi-conjugation is shown to be achievable both thermally and mechanically. The Diels-Alder adduct of these poly(fluorene-co-anthracene) polymers results in polymers with switchable conjugation. Moreover, we show how tuning of the composition of the polymers enables the tuning of the pre-strain existing on the Diels-Alder adduct and thereby tailoring of the easy of activation and the rate at which this occurs.

In *Chapter 3* we investigate a different route to create mechano-responsive semiconducting polymers, by the introduction of a molecular rotor into the backbone of a semiconducting chain. These small molecule molecular rotors have been widely applied as rigidochromic probes, e.g. as free volume probes in a variety of complex experimental systems. We incorporate the rotating phenyl group of a BODIPY rotor into the π-extended system of a polyfluorene polymer. We show that the energetic separation of the rotating moiety and the BODIPY core remains proficient to retain its rigidochromic properties. Furthermore the spectral separation between the non-responsive blue backbone emission and the responsive green bodipy emission creates an internal fluorescence emission standard. The energy transfer from the donor backbone to the acceptor rotor ensures this can be achieved using a single channel blue excitation source. This allows for the polymer to be used as a ratiometric free volume sensor in fluorescence imaging while maintaining high spectral and temporal resolution.

Previous work from our group showed how acceptor-doped conjugated polymers are very well suited for use as molecular mechanosensors.

Yet various effects remained poorly explored. In *Chapter 4*, we investigate chain-length effects on the energy transfer within acceptor-doped conjugated polymer sensors. We perform an exhaustive fractionation of a polymer batch into different fractions of higher monodispersity and different chain lengths. Using a combination of extensive spectroscopic study and Monte Carlo simulations, we show that the interplay between both chain-length and acceptor doping degree play a fundamental role in the usability of an acceptor based conjugated polymer as a strain sensor. We attribute this to a probabilistic process which occurs during the growth of the polymer chain in its synthesis. Although the law of large numbers averages these effects out for a homogeneous batch of sufficiently long polymers this is often ignored for shorter polymers. These results provide fundamental insights into the function of macromolecular strain sensors and guidelines how their use can be improved.

In addition to main theme of this thesis, as summarized above, a side-project on the assembly and phase behavior of soft colloids resulted in two published chapters. Both chapters aimed to understand how the details of the softness of small colloidal particles changes their properties in large ensembles in dense suspensions. In *Chapter 6* we use experiments and theory to explain how the softness of particles changes the apparent way in which the liquid suspension turns solid and how these apparent changes vanish when correcting for the size changes inherent to soft particles. This resolves a open issue in the field of colloidal glasses. In *Chapter 7* we continue this exploration by studying how softness, and in particular details on the shape of the soft potential, alters the formation of ordered phases. We show how small changes in the interaction potential can sort large changes in the crystal structures formed. These in-silico results provide guides to the preparation of non-close-packed and non-hexagonal crystal symmetries using colloidal particles as the building blocks.

List of Publications

THIS DISSERTATION:

- P. van der Scheer, Quintin van Zuijlen and J. Sprakel: **Rigidochromic conjugated polymers carrying main-chain molecular rotors** *Chemical Communications* 55, 11559-11562 (2019) (Chapter 2)
- P. van der Scheer, T. van de Laar and J. Sprakel: **Chain length-dependent luminescence in acceptor-doped conjugated polymers** *Scientific Reports* 9:11217 (2019) (Chapter 3)
- P. van der Scheer, T. van de Laar, J. van der Gucht, D. Vlassopoulos and J. Sprakel: **Fragility and Strength in Nanoparticle Glasses** *ACS Nano* 11(7), 6755-6763 (2017) (Chapter 4)
- Inge Bos, P. van der Scheer, Wouter G. Ellenbroek and J. Sprakel: **Two-dimensional crystals of star polymers: a tale of tails** *Soft Matter* 15, 615-622 (2019) (Chapter 5)

OTHER WORK:

- T. van de Laar, H. Schuurman, P. van der Scheer, J.M. van Doorn, J. van der Gucht and J. Sprakel: **Light from Within; Sensing Weak Strains and femtoNewton Forces in Single Molecules** *Chem*, 4(2), 269-284 (2018)
- Ties van de Laar, Ellard Hooiveld, Ruben Higler, Pieter van der Scheer, and Joris Sprakel: **Gel Trapping Enables Optical Spectroscopy of Single Solvated Conjugated Polymers in Equilibrium** *ACS Nano*, 13, 13185-13195 (2019)

Acknowledgments

Ik wil graag beginnen met het bijzonder bedanken van prof. dr. Joris Sprakel zonder wie dit boekje er uberhaupt niet zou zijn. Ik ben je erg dankbaar voor alle tijd en moeite die je in mijn persoonlijke ontwikkeling en onderzoek hebt gestoken. Ik vond het een ontzettend fijne samenwerking die ik erg ga missen. Gedurende mijn master thesis ben ik erg enthousiast geworden over het doen van onderzoek wat volkomen veroorzaakt is door jouw aanstekelijke, creatieve en toegewijde manier van onderzoek doen. Verder ben je iemand die ook altijd persoonlijk voor zijn mensen klaar staat en had ik me geen betere begeleider kunnen wensen. Heel erg bedankt voor alles!

Vervolgens mijn oud begeleider, kantoor buddy en mede AliExpress - Diamond-Member, Ties van de Laar. Jij ook heel erg bedankt voor alle hulp en bijdragen aan een memorabele 4 jaar. Altijd bereid om mensen te helpen waar je kan zolang het niet overlapt met een vakantie en zelfs dan is er hulp op afstand.

Ik wil Mara Winkels-Vink heel erg bedanken voor alle last-minute bestellingen en hulp met dingen die ik ongetwijfeld zelf zou moeten weten. Het soms starre universitaire protocol wordt een stuk aangenamer als je wordt bijgestaan door een vriendelijke dame die altijd tijd voor je heeft.

Ook spreek ik mijn dank uit aan Professor Jasper van der Gucht en mensen van PCC die ik niet bij naam en toenaam heb genoemd.

Mijn sport-collega dr. Jan Bart ten Hove (zonder baard), bedankt voor alle mental support, gezelligheid en de bereidheid tot het drinken van een incidentele versnapering. Wat twee arme PhD studenten wel niet kunnen aanrichten met een oude Saab in de Ardennen.

De mensen van kantoor 60.56 erg bedankt, toch een plek waar termen als normen en waarden nog een zekere betekenis hebben.

Al mijn studenten heel erg bedankt voor de fijne samenwerking, jullie inzet en bijdragen aan mijn onderzoek. Inge Bos, Hans Dekker, Lucile Michels, Evelien Heusinkveld & Quintin van Zuijlen. Ik heb veel van jullie geleerd en ik wens jullie het allerbeste in jullie eigen ondernemingen.

Diego mijn trouwe zwarte kat. Ik ben ernorm allergisch voor je maar je bent het helemaal waard.

Lieve Elaine, heel erg bedankt voor al je steun en geduld. Ik hoop dat we nog veel meer dingen samen kunnen vieren in de toekomst!

Ik wil de gehele familie van der Scheer heel erg bedanken voor alle steun en gezelligheid. Mijn tante Jeanine en nichtje Annabelle, ik kom altijd met veel plezier op bezoek en we hebben zelden een saai gesprek. Mijn lieve zus Caroline en haar dochter Nessa, we zien elkaar niet enorm veel maar het is altijd gezellig.

En als laatste mijn vader Charles. Iemand die ik niet genoeg waardering kan geven voor de vele rollen die hij over de jaren heeft vervult. Van paashaas tot mede-fietser en vader; hartstikke bedankt voor alles.

Pieter

Overview of completed training activities

Discipline specific activities

Dutch Soft Matter Meeting, The Netherlands (2016)

Jülich Soft Matter Meeting, Germany (Jülich, 2016)*

CHAINS, The Netherlands (NWO, 2017)*

Soft Comp annual meeting (2017-2018)*

MRS spring meeting and exhibit Phoenix (2019)*

RPK-B Polymer Physics course (2018)

NWO Superficial Superstructures consortium meetings (2015-2018)*

*poster or oral presentation

General courses

VLAG PhD week, The Netherlands (VLAG, 2016)

Project and Time Management (WGS, 2019)

Career Orientation, The Netherlands (WGS, 2019)

Journal Club, The Netherlands (2016-2020)

Optionals

Group meetings & colloquia (2015-2020)

Voets-Sprakel meeting (2016-2017)*

The research described in this thesis was supported financially by the Netherlands Organisation for Scientific Research (NWO) TOP-PUNT programme ’Superficial Superstructures’ (project number: 718.015.002)
Printed by Proefschriftmaken.nl in 100 copies